The Dynamical Ocean Component of the Madden-Julian Oscillation

A thesis submitted to the School of Environmental Sciences of the University of East Anglia in partial fulfilment of the requirements for the degree of Doctor of Philosophy

By Benjamin G. M. Webber

June 2012

Abstract

At time scales between synoptic weather and the seasonal cycle, the Madden-Julian Oscillation (MJO) is the dominant cause of atmospheric variability in the tropics, modifying seasonal rainfall totals and influencing atmospheric circulation worldwide. It induces a large response in the tropical oceans through surface fluxes of heat and momentum. While the thermodynamic ocean-atmosphere interaction has been well studied, understanding is lacking on the dynamical ocean response to MJO-induced surface momentum fluxes. A comprehensive observational study of the nature of this response is undertaken. This indicates large amplitude and coherent dynamic variability consisting of equatorial ocean Kelvin and Rossby waves, along with coastally-trapped waves and extra-tropical responses. These processes have important implications for ocean circulation, chemistry and biology. Furthermore, it is shown that this response in the ocean dynamics can influence the behaviour of the MJO itself. The propagation of equatorial ocean Rossby waves into the western Indian Ocean causes deepening of the thermocline, positive temperature advection and thus positive sea surface temperature anomalies that trigger atmospheric convection. This constitutes a feedback that will modify the behaviour of the MJO, strengthening its low frequency component and enhancing its intermittent nature. The ocean dynamics can also trigger individual Madden-Julian (MJ) events through the same oceanic processes. This triggering mechanism is strongest for 'primary' MJ events that are not immediately preceded by other MJO activity, nor by any other triggers.

A linearised ocean model is used to understand the fundamental principles behind the observed dynamical ocean component of the MJO. It is shown that the equatorial Rossby waveguide is more effective at transferring dynamic anomalies to the western Indian Ocean than the coastal Kelvin waveguide. Sensitivity studies demonstrate that westerly wind bursts with a broader latitudinal scale will be considerably more effective in generating a dynamical ocean response that can feed back onto the MJO. Crucially, it is shown that these dynamical ocean processes are predictable over periods of up to five months, far longer than the time scale over which the MJO can be predicted. It may therefore be possible to use observations of the ocean dynamics to improve forecasts of the MJO during periods of inactivity, when it has previously been most difficult to predict.

Acknowledgements

I would like to sincerely thank Dr Adrian Matthews, Prof. Karen Heywood and Prof. David Stevens for providing the opportunity of this Ph.D., and for their insight, guidance and inspiration throughout. Thanks to my examiners, Prof. Tim Osborn and Dr Steve Woolnough for an interesting and stimulating viva!

I have particularly enjoyed attending conferences, meetings and summer schools during my Ph.D., and am grateful to NERC and the school of ENV for providing the funding to make this possible. I am especially grateful to the organisers and participants in the NERC Climate Modelling Summer School, the IUGG conference in Melbourne, the Challenger Society conference in Southampton and the various Royal Met Soc conferences and student conferences, as well as my companions on the memorable nights out that ensued. I have also been fortunate enough to participate on two research cruises during my PhD; thanks to Brian King and Karen Heywood for organising those, and to the scientists and crew who made them so memorable.

I have been fortunate to be located within an office full of awesome fellow Ph.D. students. Big thanks go to all the inhabitants of the Beach over the past three and a half years, for the stimulating science and for the after-hours entertainment. Thanks in particular to Nick Earl, Bastien Queste, Jenny Graham, Chris Walker-Brown, Rob Graham and Chris O'Donnell. And thank you to all the other friends I've made during the PhD, far too many of you to name!

I am also fortunate to have friends outside the world of academia to divert me from the stress of a Ph.D. Big thanks to Tom and Vicki Sparkes, Rosa Britton and Dave Townsend, Andy Pattinson, Tom Heath, Tom Marr, Tom Powell, Chris Atkinson and Rachel Murphy for all the awesome trips to the hills. Thanks to Nem for continuous hilarity, entertainment and banter, and for the unquestioning love and support.

And finally, thanks to my family, Clare, John and Zoe for their support, motivation and love throughout, and for providing epic holidays when I've needed them the most.

Contents

List of tables

List of figures

Chapter 1

Introduction

This thesis concerns the interaction between two distinct climatic systems: the intraseasonal atmospheric variability of the Madden-Julian Oscillation (MJO), and the ocean dynamics triggered by resultant surface wind stress anomalies. The dynamical ocean response has largely been ignored in the context of the MJO, and it is this lack of knowledge that the current work seeks to rectify. The two components of this project will be outlined in turn below, starting with an introduction to the MJO, its importance for climate and impacts on human activity. In addition, the various mechanisms that explain its existence, behaviour and interactions with the ocean will be explained. An overview of the theory and fundamental equations underlying equatorial ocean dynamics will then be provided, with particular focus on the equatorial Kelvin and Rossby wave solutions to the shallow water equations on the equatorial β-plane. The vertical and horizontal structure of these waves, along with their propagation and reflection at meridional boundaries will then be described. Finally, the motivation for this present work will be outlined.

1.1 The Madden-Julian Oscillation

The MJO is an important source of global climate variability. At intraseasonal time scales (periods between weekly weather variability and the seasonal cycle), the MJO is the dominant source of climatic disturbance in the tropical atmosphere. It can be responsible for destructive floods and droughts, and modifies the seasonal rainfall totals on which billions of people depend for food production. The phenomenon was discovered, somewhat serendipitously, by Roland Madden and Paul Julian, and the characteristics described in

two seminal papers (Madden and Julian, 1971, 1972).

The MJO is characterised by large scale (order 10,000 km) disturbances, or anomalies, in convection, rainfall and wind throughout the depth of the troposphere. These anomalies propagate eastwards along or near the equator, at an average speed of around 5 m s^{-1}, typically starting in the western Indian Ocean and decaying in the central Pacific (e.g., Madden and Julian, 1972; Wheeler and Hendon, 2004). However, there is a component of the atmospheric signal that circumnavigates the globe at the same time scale, primarily as an atmospheric equatorial Kelvin wave although the signal is complicated by the obstructing mountain ranges of South America, Africa and the Maritime Continent (Matthews, 2000; Hsu and Lee, 2005). The MJO is a primary driver of precipitation variability in the monsoon regions of Asia (e.g., Wang and Rui, 1990), Australia (e.g., Hendon and Liebmann, 1990; Wheeler *et al.*, 2009), India (e.g., Wang and Rui, 1990; Pai *et al.*, 2011), South America (e.g., Liebmann *et al.*, 2004) and Africa (Matthews, 2004a; Lavender and Matthews, 2009). In addition, it generates anomalies in circulation and rainfall worldwide (Matthews *et al.*, 2004; Donald *et al.*, 2006), with implications for medium-range (e.g., monthly) weather forecasting (Vitart and Molteni, 2010).

The structure of the anomalies associated with the MJO is described in Madden and Julian (1972). The MJO has been subsequently defined separately in many studies, but these typically base their definition on empirical orthogonal function (EOF, Wilks, 1995) analysis of outgoing longwave radiation (OLR) data. Recently, it has become common to use the Wheeler-Hendon index, based on the first two coupled EOFs of OLR and zonal wind at 850 and 200 hPa (Wheeler and Hendon, 2004) for studies of the MJO. Figure 1.1 shows the surface wind and convective anomalies for the eight phases defined by this index during the months of December–February; Figure 1.2 is for May–June.

It is typical to think of the MJO as 'starting' in the Indian Ocean, with the initiation of enhanced convective anomalies here that subsequently propagate eastwards and amplify, reaching peak magnitude near the Maritime Continent. Phases 1–3 correspond to developing convection over the Indian Ocean, phases 4–5 the peak of convection over the Maritime Continent and phases 6–8 the progression into the western Pacific and eventual decay. The regions of reduced convection exhibit similar behaviour but offset by half a cycle (4 phases) such that the convective minimum over the Maritime Continent occurs

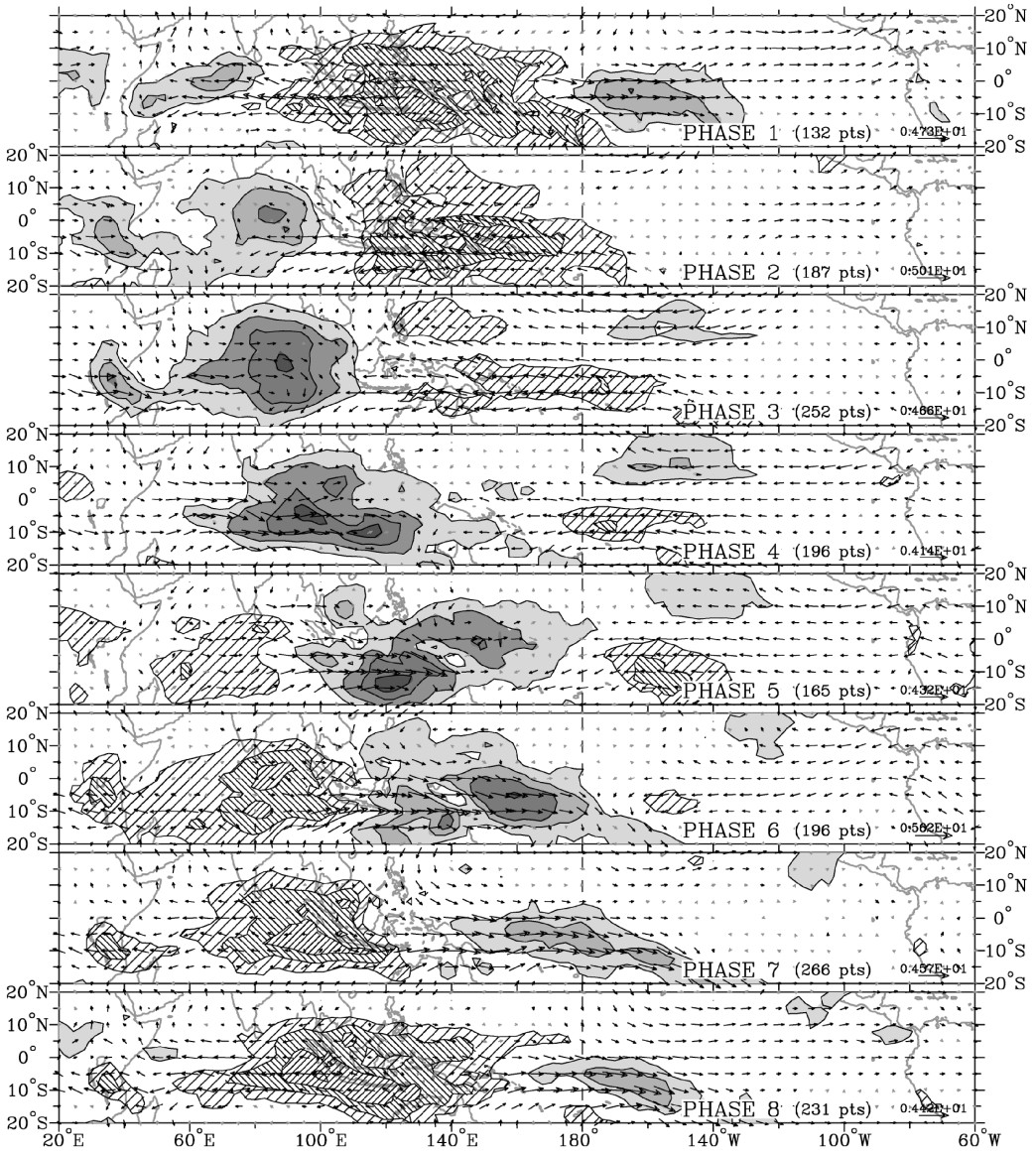

Figure 1.1: December-February (DJF) composite of OLR and 850 hPa zonal wind anomalies for the 8 phases of the Wheeler-Hendon index. Shading levels denote OLR anomalies less than -7.5, -15, -22.5, and $-$ 30 W m^{-2}, respectively, and hatching levels denote OLR anomalies greater than 7.5, 15 and 22.5 W m^{-2}, respectively. Black arrows indicate wind anomalies that are statistically significant at the 99% level. The magnitude of the largest vector is shown on the bottom right, and the number of days (pts) falling within each phase category is given. Reproduced from Wheeler and Hendon (2004)

between phases 8 and 1. In summer the MJO activity is similar to in winter but displaced north of the equator (Figure 1.2). In addition, the propagation of the convective anomalies from phase 2–4 clearly exhibits the northward propagation over the Indian subcontinent identified by Wang and Rui (1990). Wind anomalies associated with the enhanced convective signal are primarily a zonal circulation comprising of convergent flow near the surface and divergence aloft; the reverse is true for the suppressed phase of the MJO.

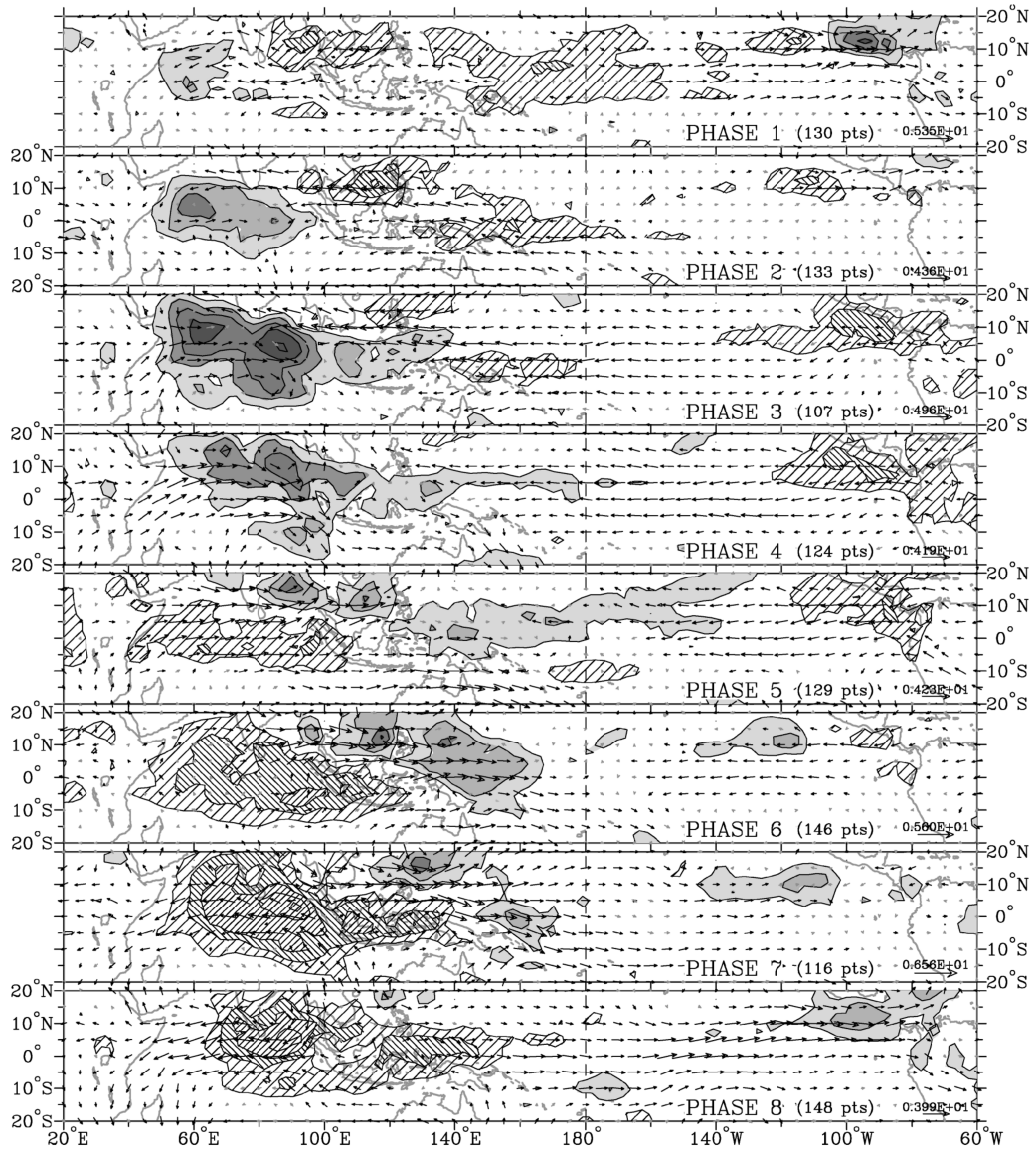

Figure 1.2: As Figure 1.1 but for May–June. Reproduced from Wheeler and Hendon (2004)

The MJO undergoes a substantial seasonal cycle (Madden, 1986; Wang and Rui, 1990; Salby and Hendon, 1994). During boreal winter and the spring and autumn, the MJO is strongly active and propagates zonally along or slightly to the south of the equator; the maximum activity occurs near the equinoxes when the intertropical convergence zone (ITCZ) migrates across the equator (Salby and Hendon, 1994). Conversely, during boreal summer, the MJO interacts strongly with the northern hemisphere monsoons and thus propagates northwards into the Indian subcontinent and Southeast Asia (Wang and Rui, 1990; Salby and Hendon, 1994; Pai *et al.*, 2011). This behaviour is summed up in Figure 1.3, which shows MJO activity and propagation paths averaged over the year; the zonally

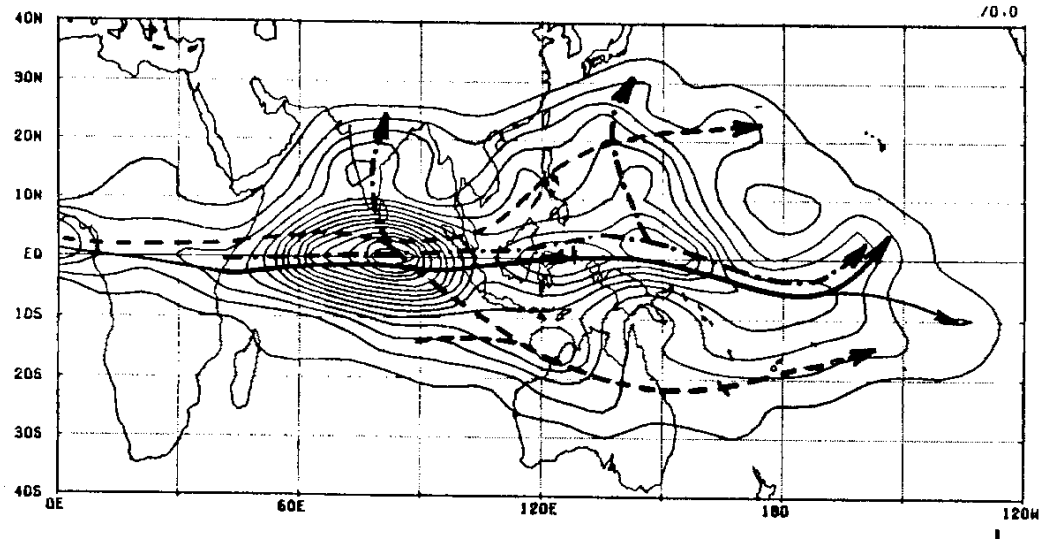

Figure 1.3: Contour plot of the total number of occurrences of strictly eastward-moving cloud complexes associated with MJ events. The solid line indicates the central path for zonally-propagating events, typical of the period around the equinoxes. The dashed lines indicate the central paths for other behaviour of the MJO during boreal summer, when it propagates northwards over India and Asia, and during boreal winter, when it can propagate over Australia (from Wang and Rui, 1990).

propagating behaviour is exhibited throughout the period of October–April, while the northward propagating branches are active in May–September. The convective signal does also interact with the Australian monsoon during austral summer, but this has a relatively minor impact on the overall behaviour of the MJO.

The MJO undergoes a large amount of interannual variability, which raises the question of whether the overall activity is predictable. However, Slingo *et al.* (1999) found that the mean global MJO strength is only very weakly correlated with sea-surface temperatures (SSTs) and not apparently caused by ENSO. However, the eastwards extension of the warm pool in response to an El Niño event leads to a similar expansion of the region of MJO activity (e.g., Hendon *et al.*, 1999; Bergman *et al.*, 2001). The timescale and propagation speed of the MJO is known to vary on interannual timescales; Pohl and Matthews (2007) showed that the MJO propagates significantly faster (slower) in El Niño (La-Niña) years. In addition, decadal trends in MJO activity have been shown to be significantly correlated with SSTs in the Indian Ocean and may therefore be altered by climate change (Slingo *et al.*, 1999).

The time scale of the MJO is not well defined. It was initially discovered as a broad spectral peak in the zonal wind field between 40 and 50 days (Madden and Julian, 1971).

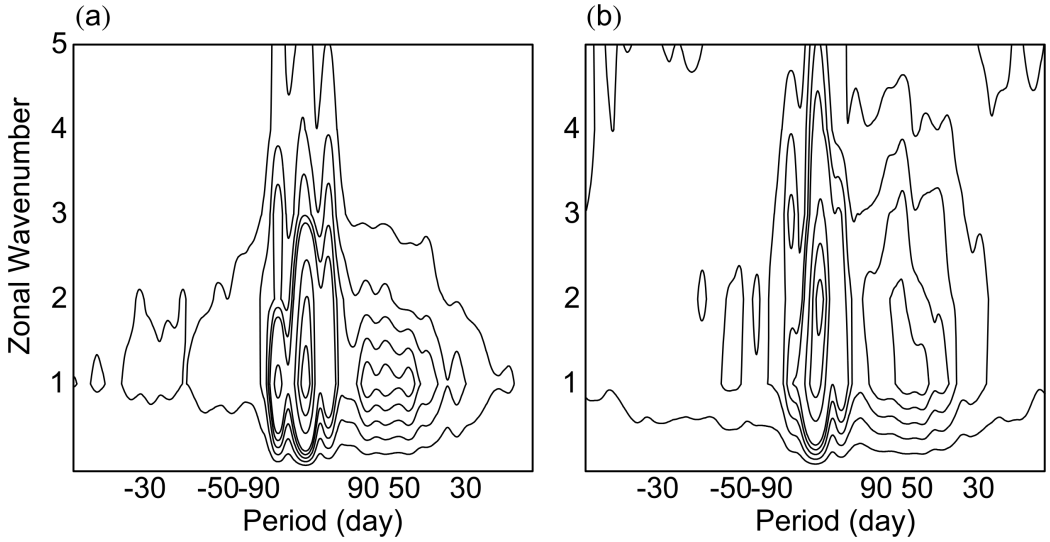

Figure 1.4: Time-space power spectra of (a) 850 hPa zonal wind (NCEP/NCAR reanalysis) and (b) precipitation (Xie and Arkin, 1997) for the period of 1979–1998, averaged over 20°N–20°S and 60°–180°E. Positive periods correspond to eastward propagating power, and negative periods to westward propagating power (from Zhang, 2005).

Since then definitions have varied, with 30–60 days being a common definition (e.g., Knutson and Weickmann, 1987; Ferranti *et al.*, 1990), but the convective signal has a substantial amount of spectral power extending to 95 days or more (Salby and Hendon, 1994). There are disagreements over the cause of this low-frequency tail, with some authors viewing it as a separate mode, for example with regard to the atmosphere-ocean resonance at periods around 90 days in the Indian Ocean (Han *et al.*, 2001; Han, 2005). Alternatively, the spectral power could be viewed as the manifestation of nonlinear interactions between various dynamical components of the MJO (Salby and Hendon, 1994). The temporal and spatial scales of the MJO are summed up in Figure 1.4, which shows the spectral power of precipitation and zonal wind at 850 hPa. In both spectra there is a broad peak around periods of 40–90 days that is strongest around wavenumber 1, but there is substantial power out to wavenumbers 3 and 4 in the precipitation spectrum. This implies that the zonal wind is strongly influenced by the large scale Kelvin and Rossby wave structures of the MJO, while the precipitation more closely follows the convective signal which tends to have somewhat smaller spatial scales.

The MJO involves a substantial amount of interaction between widely disparate spatial scales, from the scale of individual cumulonimbus clouds to zonal wavenumber 1 atmospheric Kelvin waves that span the Pacific ocean (Nakazawa, 1988; Slingo *et al.*, 2003; Majda and Biello, 2004). The convective signal of the MJO can be broken into

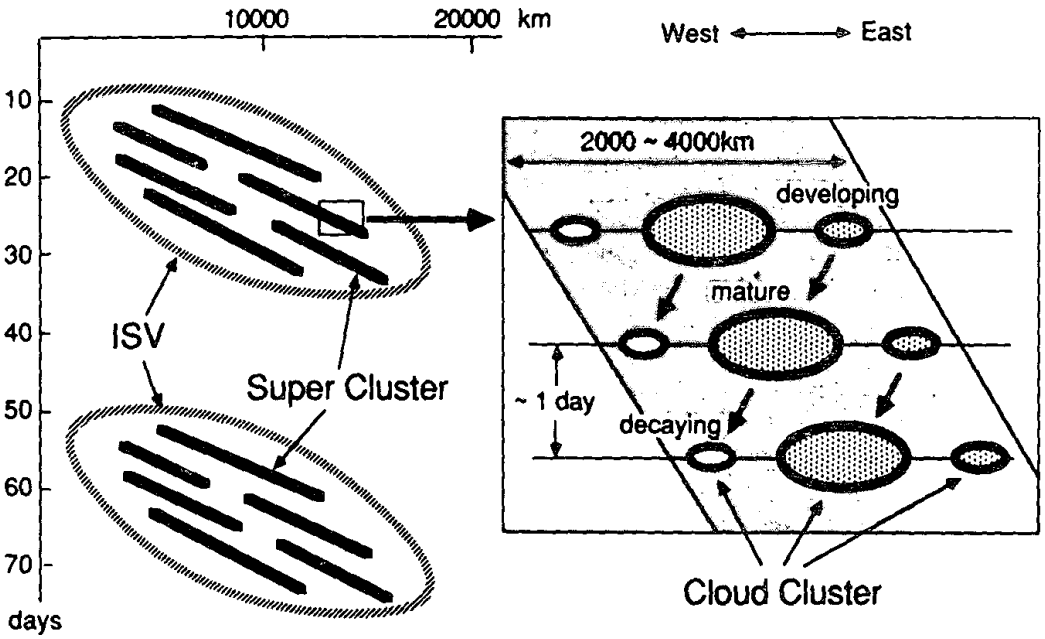

Figure 1.5: Schematic describing the details of the cloud complexes that comprise the MJO at various scales. Slanting heavy lines represent super cloud clusters (SCC) within the larger complexes of the intraseasonal variability (ISV). The right-hand side illustrates the fine structure of the SCC with smaller westward-moving cloud clusters that have a life cycle of a few days (from Nakazawa, 1988)

discrete scales, as illustrated by Figure 1.5, with the broadest envelope of convection containing super clusters of clouds that in turn contain *westward*-propagating cloud clusters (Nakazawa, 1988). There is also interaction between convection occurring with different vertical scales and the resulting diabatic heating profile; the precise vertical structure of this can have a large impact on the phase speed of the resulting MJO (e.g., Chang and Lim, 1988; Sui and Lau, 1989; Wu, 2003). In addition, there are interactions over different time scales, such as the interaction with the diurnal cycle in the ocean mixed layer mentioned above. These scale interactions are one of the major obstacles in accurately simulating the MJO in numerical models (Slingo *et al.*, 2003).

There have been various mechanisms proposed to explain the propagation of the MJO. Mechanisms involving atmospheric wave dynamics tend to produce solutions that propagate faster than observations (e.g., Chang and Lim, 1988), but improvements arise once coupling with the ocean is included (e.g., Waliser *et al.*, 1999; Inness and Slingo, 2003). Thus the MJO can be though of as a coupling between atmospheric equatorial dynamics and convection that is in turn thermodynamically coupled to the ocean. The atmospheric

dynamics are described by Salby and Hendon (1994) and Matthews (2000); these processes comprise the atmospheric equatorial wave response to convective heating following the Matsuno-Gill model (Matsuno, 1966; Gill, 1980), which in turn leads to frictional moisture convergence in the boundary layer of the equatorial Kelvin wave. This surface moisture convergence acts to enhance the convection to the east of positive convective anomalies and vice-versa. The Rossby wave response to enhanced convection leads to divergent anomalies that in turn reduces the convective anomalies to the west. The combination of these mechanisms can be shown to produce a self-sustaining mode in the warm pool region that propagates eastwards, consistent with observations (Matthews, 2000). In addition, there is a radiating atmospheric wave component of the response to this convective heating that propagates away from the convective anomaly at around 10 m s^{-1} (Salby and Hendon, 1994) and can in turn circumnavigate the globe and trigger a subsequent cycle of the MJO (Matthews, 2000).

The thermodynamic interaction between the atmospheric variability of the MJO and the sea surface temperatures (SSTs) has been a subject of lively debate (see Zhang, 2005, for a review), but the evidence suggests that it has a role to play in the existence and propagation of the MJO. The primary feedback mechanism was laid out by Flatau *et al.* (1997), based on observational evidence from ocean buoys in the equatorial Pacific, and further refined in several papers (e.g., Shinoda *et al.*, 1998; Woolnough *et al.*, 2000). Within the warm pool where the MJO is most active, mean surface westerly winds are enhanced by westerly wind anomalies associated with the MJO; easterly wind anomalies lead to a reduction in the total wind speed. Therefore, since latent heat fluxes depend upon the magnitude of the total wind speed (rather than the anomalies), the westerly wind bursts that follow the enhanced convective anomalies cause a marked increase in total wind speed and latent heat flux out of the ocean. Associated with this is the reduction in insolation caused by the active convection itself. Thus, negative SST anomalies follow enhanced convection and lead reduced convection; the inverse applies for positive SST anomalies, giving a quadrature relationship between convection and SSTs that suggests the potential for feedbacks. This behaviour is summarised in Figure 1.6, which illustrates the buildup of deep convection to the west of moisture convergence, high SSTs and a shallow mixed layer, followed by suppressed convection due to cold SSTs and moisture

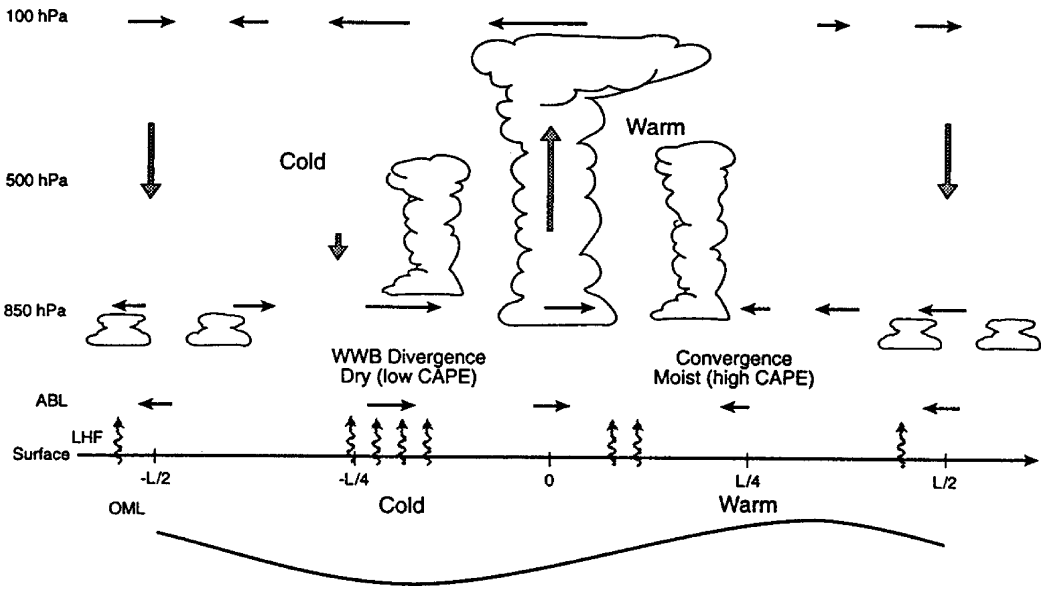

Figure 1.6: Schematic diagram illustrating the vertical structure of the MJO and its interaction with the MJO, as observed during the TOGA COARE experiments (Webster and Lukas, 1992). The squiggly lines denote surface latent heat flux. The symbols ABL, OML, LHF, WWB, CAPE and L represent, respectively, atmospheric boundary layer, ocean mixed layer, latent heat flux, westerly wind burst, convective available potential energy, and wavelength. Adapted from Wang and Xie (1998)

divergence.

Further evidence for the importance of coupling with the ocean comes from numerical model experiments. Simulations of the MJO tend to perform better when such thermodynamic coupling is simulated (Inness and Slingo, 2003), and realistic MJO behaviour arises in atmosphere-only models as a forced response to observed intraseasonal SST variability (Woolnough *et al.*, 2001; Fu and Wang, 2004; Matthews, 2004b). Model performance is further enhanced when the diurnal cycle of SST is simulated, since this can have a large impact on daily mean SSTs during clear-sky (break) phases of the MJO (Bernie *et al.*, 2005; Klingaman *et al.*, 2011).

There are many processes that lead to the initiation of new MJO events. As mentioned above, it is common for one event to trigger another, through atmospheric dynamics and ocean-atmosphere interaction. In addition, forcing from the extratropics may be important (Lau and Peng, 1987; Hsu *et al.*, 1990; Matthews and Kiladis, 1999), as may stochastic forcing within the tropics (Salby and Garcia, 1987; Majda and Biello, 2004). However, it can be difficult to separate out the signals to determine what are the signatures of a previous MJO cycle and what are triggers for a subsequent event. Furthermore, the MJO is sporadic, with periods of cyclical activity interspersed with periods of relative

quiescence. It can therefore be useful to define the MJO as a series of Madden-Julian (MJ) events, which can be split into successive events, that follow previous MJO activity, and primary events that arise after a period of inactivity. Matthews (2008) uses this distinction to investigate triggering mechanisms for the two types of event, thus allowing a more robust distinction between processes that might generate MJO activity and those that are generated by the MJO. Successive events are associated with a multitude of triggering mechanisms, including warm SST anomalies, cold upper-atmospheric anomalies that destabilise the atmosphere, mid-latitude disturbances propagating into the tropics and boundary layer convergence and humidity anomalies (Matthews, 2008, and references therein). However, no consistent or statistically significant triggers for primary events were found, which leaves an unfortunate gap in our understanding of the MJO, which this thesis attempts in part to address.

1.2 Equatorial Ocean Dynamics

Studies of the dynamics of the equatorial ocean and atmosphere have been motivated by the desire to understand large scale interannual climate variability such as the El Niño-Southern Oscillation (ENSO). The fundamental mechanisms behind ENSO variability depend upon the propagation of equatorial Kelvin and Rossby waves in the ocean, coupled to the atmosphere by the Bjerknes feedback mechanism (Bjerknes, 1969). Similar processes lead to the existence of the Indian Ocean Dipole (IOD; also known as the Indian Ocean Zonal Dipole Mode (IOZDM); Saji *et al.*, 1999). The propagation of such equatorial waves is crucial for transporting signals from one side of the ocean to the other in a relatively short period of time. Equatorial ocean Kelvin and Rossby waves were the main components of the theoretical model of Zebiak and Cane (1987) that described a 'delayed oscillator' response to surface wind forcing to explain ENSO. In this model, the positive feedback cycle triggered by the initial Kelvin wave is mediated by reflection of equatorial Rossby waves of the opposite sign at the western boundary of the Pacific (Suarez and Schopf, 1988; Battisti, 1988; Boulanger and Fu, 1996). However, more recent analysis suggests that such mechanisms do not account for all ENSO variability; for example it does not account for the role of the MJO in triggering El Niño events (Kessler and McPhaden, 1995; McPhaden, 1999). See Neelin *et al.* (1998) for a review of ENSO

theory and mechanisms.

Figure 1.7 shows a schematic of the equatorial Kelvin and Rossby waves. It is a curious fact that the vertical structure of the majority of ocean dynamics can be attributed to a single form, namely the first baroclinic mode (Wunsch, 1997); we will examine possible reasons for this below. The vertical structure for these waves is one where the horizontal velocity anomalies are of the opposite sign in the mixed layer relative to the deep ocean. The anomalies in the mixed layer are also orders of magnitude larger than in the deep ocean; this difference in magnitude is balanced by the difference in the depth of the two layers. The sign of the sea surface height anomalies is opposite to the anomalies in thermocline depth so that waves with positive SSH anomalies are also associated with deeper mixed layers. It is therefore customary to term such phenomena "downwelling" waves, and we use this terminology throughout despite the fact that such waves are associated with both downwelling (at the leading edge of the wave) and upwelling (at the trailing edge). The horizontal structure of Kelvin waves is to have a single maximum in SSH and zonal velocity at the equator; equatorial Rossby waves have more complex horizontal structures with multiple 'meridional mode' solutions possible (see section 1.2.2); Figure 1.7 shows the meridional structure for the first (and most common) of these modes.

There is a rich body of literature describing the properties of the various equatorial waves, all of which are solutions to the primitive equations on an equatorial Beta plane, whereby the latitudinal variation of the Coriolis parameter f is approximated by assuming its gradient β is constant, giving $f = \beta y$. An overview of the key points from this literature is provided here; for further information and derivations see, e.g., Lighthill (1969), Moore and Philander (1977), Philander (1979) and Gill (1980).

The primitive equations of motion are derived from the Navier-Stokes equations for fluid flow, using the Boussinesq approximation that ignores density variations except in

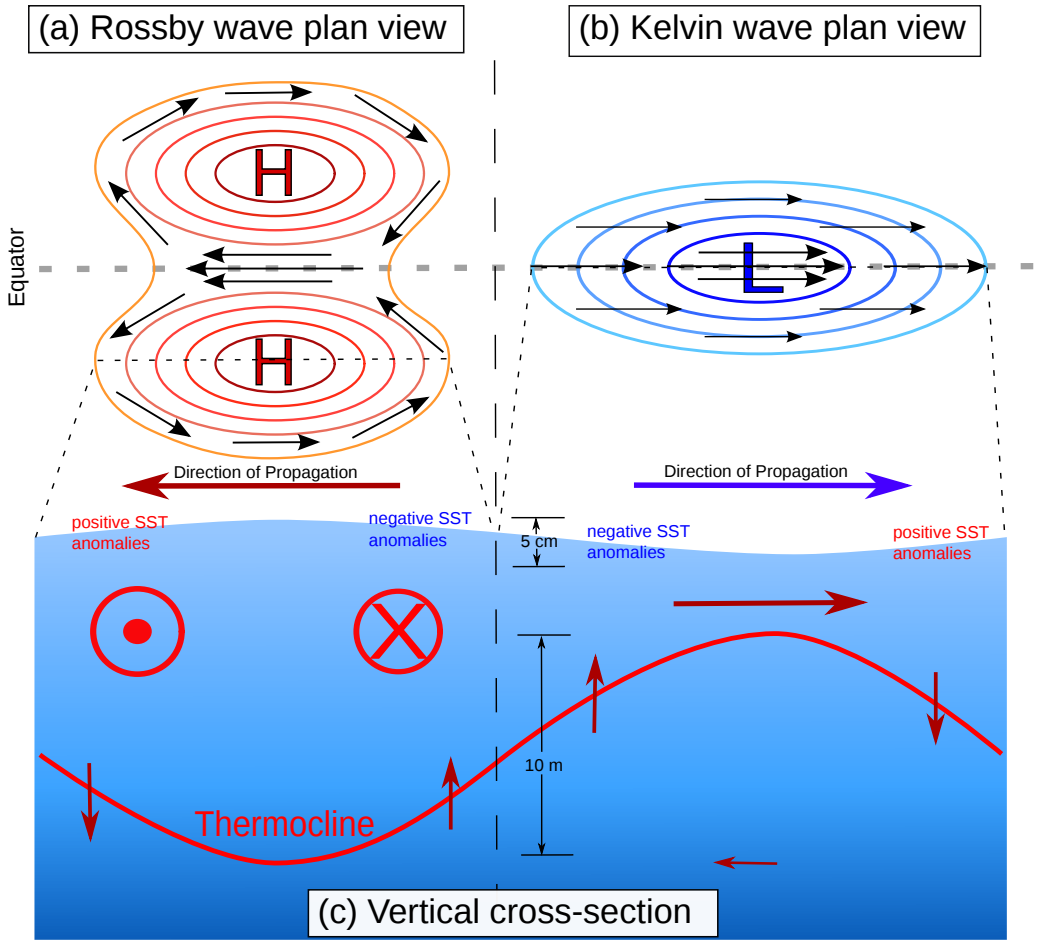

Figure 1.7: Schematic diagram illustrating the horizontal and vertical structure of equatorial Kelvin and Rossby waves. (a) and (b) show plan views of the sea surface height (contours) and surface velocity vectors for (a) a first meridional mode 'downwelling' Rossby wave (positive SSH anomaly) and (b) an 'upwelling' Kelvin wave. (c) shows the corresponding thermocline depth (solid red line) and circulation anomalies (not to scale); for the Rossby wave, this corresponds to a cross section through the southern hemisphere circulation, while for the Kelvin wave it corresponds to a cross section through the equator (see dashed lines).

the vertical, and are as follows for the ocean

$$\begin{aligned}
\frac{Du}{Dt} - fv &= \frac{1}{\rho_0}\frac{\partial p}{\partial x} + F^u, \\
\frac{Du}{Dt} - fv &= \frac{1}{\rho_0}\frac{\partial p}{\partial x} + F^v, \\
\frac{\partial p}{\partial z} &= -\rho g, \\
\nabla.\mathbf{v} &= 0,
\end{aligned}$$

where

$$\frac{D}{Dt} = \frac{\partial}{\partial t} + u\frac{\partial}{\partial x} + v\frac{\partial}{\partial y} + w\frac{\partial}{\partial z},$$

f is the coriolis parameter, ρ_0 is the mean density field following the Boussinesq approximation, and F^u, F^v are the forcing components in the x and y directions, respectively.

1.2.1 Vertical structure

To derive the equations describing equatorial waves, it is necessary to separate the vertical variation (i.e. dependence on z or p) from the remaining variations in space and time (i.e. dependence on x, y, t), by assuming that nonlinear terms in the equations of motion are small, except for the vertical advection of background stratification. Thus

$$\begin{aligned} u(x,y,z,t) &= \tilde{u}(x,y,t)h(z), \\ v(x,y,z,t) &= \tilde{v}(x,y,t)h(z), \\ \eta(x,y,t) &= \tilde{\eta}(x,y,t), \\ \omega(x,y,z,t) &= \tilde{\omega}(x,y,t)j(z), \end{aligned}$$

Note that the vertical structure for ω ($j(z)$) is different from the other vertical structure functions ($h(z)$), and that η, the sea surface height, does not have a vertical structure function as it is only defined at the surface. We will derive equations for h and j below. Substitution of the above terms for velocity into the continuity equation suggests that $h = \dfrac{\partial j}{\partial p}$. Solving the primitive equations using such approximations gives the following equation for the vertical variability:

$$\frac{\partial}{\partial z}\left(\frac{1}{N^2}\frac{\partial j}{\partial z}\right) + \frac{1}{c_e^2}j = 0$$

where $N = \sqrt{-\dfrac{g}{\rho}\dfrac{\partial \rho}{\partial z}}$ is the Brunt-Väisälä frequency, and $c_e^2 = \dfrac{NH}{n\pi}$ is the separation constant that yields c_e, the phase speed of the first baroclinic mode Kelvin wave.

The solution of the above differential equation (1.2.1) leads to the vertical structure

for uniform stratification,

$$j = A\sin\left(\frac{n\pi z}{H}\right),$$
$$h = A\frac{n\pi}{H}\cos\left(\frac{n\pi z}{H}\right).$$

Representing the vertical structure by a two-layer approximation is a common simplification used for idealised analytical and numerical models. For the two-layer structure comprising a well-mixed surface layer separated from the deep layer by a sharp thermocline, the solution permits only the first baroclinic mode, as shown in Figure 1.7. The surface flow is amplified relative to the deep flow by a factor of $1/H_e$ where $H_e = \dfrac{\rho_2 - \rho_1}{\rho_0} H_1$ is the equivalent depth (ρ_0, ρ_1, ρ_2 being the mean potential density and the potential density of the upper and lower layers respectively; see Lighthill, 1969). The effect of realistic ocean stratification, with a smooth thermocline near the surface is to modify the sine and cosine solutions of the uniform stratification case such that the variability is amplified near to the surface where the potential density gradient is large (Giese and Harrison, 1990). The phase speeds, equivalent depth and Rossby radius of deformation can be calculated locally for each mode by considering the stratification; see Chelton *et al.* (1998) for details.

To determine the dynamic ocean response to surface forcing, it is necessary to understand the projection of wind forcing onto the various baroclinic modes. As discussed by Lighthill (1969), it is useful to make the approximation of assuming that the wind stress will exert a constant body force, denoted Z_n for each mode, over a mixed layer of depth h_{mix}. This is a reasonable approximation in the tropical regions where the Ekman depth is large. Assuming this, it is possible to show that

$$1 + \sum_{n=1}^{\infty}\left(\frac{Z_n}{Z_0}\right) = \frac{H}{h_{mix}}$$

thus implying that the relative forcing of the baroclinic modes depends critically upon the mixed layer depth (Moore and Philander, 1977). Lighthill showed that for $h_{mix} = 200$ m and $H = 4000$ m, $\dfrac{Z_1}{Z_0} = 13.9$; for this reasonable example, the first baroclinic mode is forced almost 14 times as strongly as the barotropic mode. The equivalent term for the second baroclinic mode is approximately 5 (Moore and Philander, 1977), and the sum of

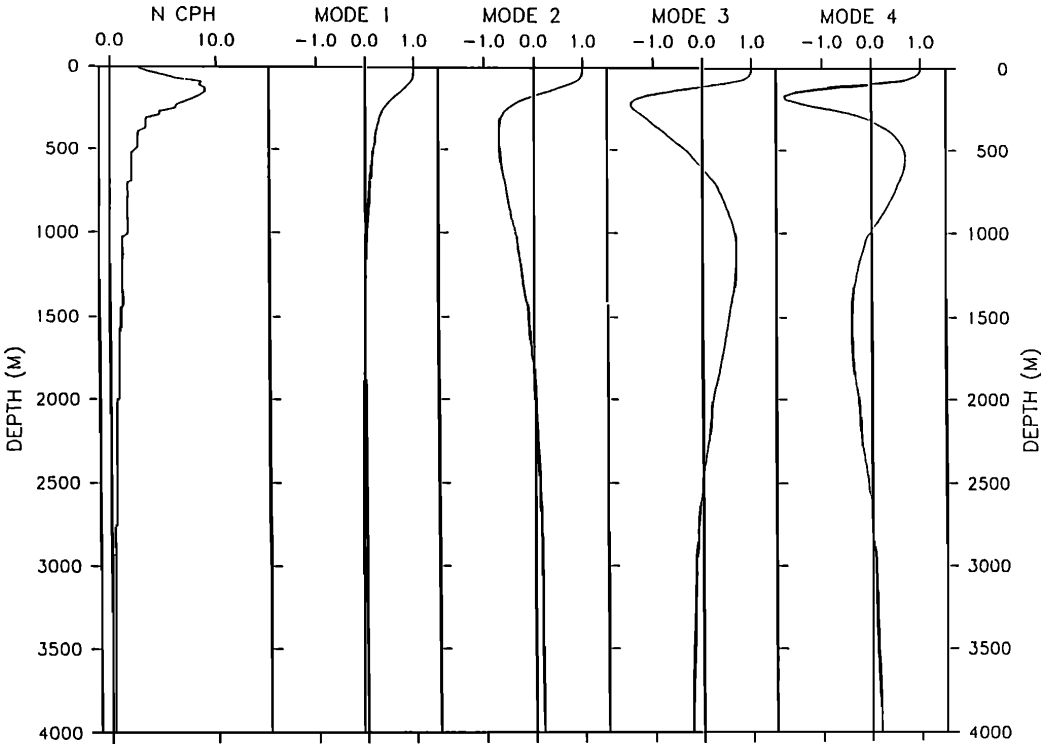

Figure 1.8: The buoyancy (N) profile for density stratification at 160°E in the equatorial Pacific. The zonal velocity structure functions of the first four baroclinic modes, normalized to unity at the surface, are also shown. Reproduced from Giese and Harrison (1990)

all modes (including the barotropic) is 20. Thus the first and second baroclinic modes and the barotropic mode account for approximately 70%, 25% and 5% of the forced response respectively, and higher modes are negligible. For stratification representative of the eastern Pacific, forcing projects more evenly across the first four baroclinic modes. However, dispersive effects are more important in the higher modes, as are nonlinear interactions between modes, even for nondispersive Kelvin waves (Giese and Harrison, 1990). The net effect of these considerations is that the response of the equatorial oceans is dominated by the first baroclinic mode, but that the next few modes can be important for understanding the full response, especially in regions where the mixed layer is shallow. The vertical structure of these modes is shown in Figure 1.8.

1.2.2 Horizontal structure and wave solutions

Following separation of the vertical variations in the momentum equations, we are left with the shallow water equations describing horizontal motion on the equatorial β plane

$$\begin{aligned} \frac{\partial u}{\partial t} - \beta y v &= -g\frac{\partial \eta}{\partial x}, \\ \frac{\partial u}{\partial t} - \beta y v &= -g\frac{\partial \eta}{\partial x}, \\ g\frac{\partial \eta}{\partial t} + c_e^2\left(\frac{\partial u}{\partial x} + \frac{\partial v}{\partial y}\right) &= 0, \end{aligned}$$

where η is the free surface height. These are analogous to the equations for surface gravity waves. For the equatorial Kelvin wave, we set $v = 0$ and look for wavelike solutions in x and t such that

$$\begin{aligned} u(x,y,t) &= \tilde{u}(y)e^{ik(x-ct)}, \\ \eta(x,y,t) &= \tilde{\eta}(y)e^{ik(x-ct)} \end{aligned}$$

where simple substitution shows that $c = \pm c_e$. By substituting back into the equation for u, and solving a first order differential equation, we obtain the solution $\tilde{u} = De^{-\frac{\beta y^2}{2c}}$ which is only bounded for the case where $c = +c_e$. Thus the phase speed is positive and the equatorial Kelvin wave travels eastwards. The trapping scale of the wave is given by $R_n = \sqrt{\frac{c}{2\beta}}$, where R_n is the equatorial Rossby radius of deformation. For values typical of an equatorial Kelvin wave in the ocean this gives a trapping scale of around 4° latitude. The solution for an equatorial Kelvin wave is as follows:

$$\begin{aligned} u &= u_0 e^{ik(x-c_e t)} e^{\frac{-\beta y^2}{2c_e}} \cos\left(\frac{n\pi z}{H}\right), \\ v &= 0, \\ \omega &= -\frac{u_0 H}{n\pi} e^{ik(x-c_e t+\pi/2)} e^{\frac{-\beta y^2}{2c_e}} \sin\left(\frac{n\pi z}{H}\right), \\ \rho &= \frac{c_e u_0 n\pi}{H} e^{ik(x-c_e t+\pi/2)} e^{\frac{-\beta y^2}{2c_e}} \sin\left(\frac{n\pi z}{H}\right), \\ \eta &= (c_e/g) u_0 e^{ik(x-c_e t)} e^{\frac{-\beta y^2}{2c_e}} \end{aligned}$$

where $u_0 = DAn\pi H$. The full solution for the equatorial Kelvin wave response to some forcing can be written as the sum over all baroclinic modes n. Note that the solution is a

combination of an eastward travelling wave, the vertical structure of the baroclinic mode and Gaussian trapping in latitude given by the Rossby radius of deformation.

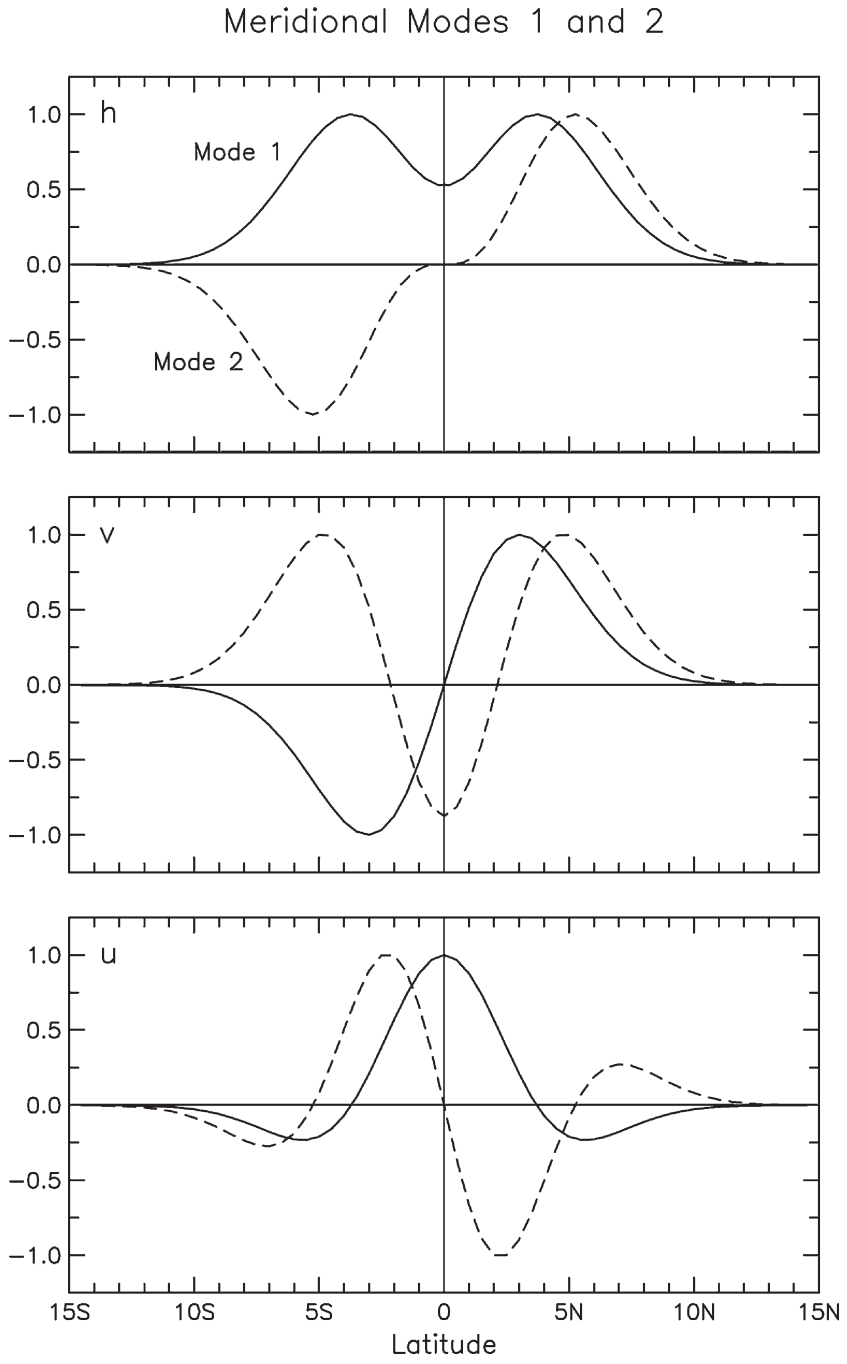

Figure 1.9: The latitudinal structures of sea surface height h, meridional velocity v, and zonal velocity u for the first (solid lines) and second (dashed lines) meridional modes of the classical equatorial Rossby wave theory. Reproduced from Chelton *et al.* (2003)

More general equatorial wave solutions can be found in a similar manner, but require a solution where v is nonzero. The solutions are well known and are given by

$$v = 2^{-m/2} H_m(y\sqrt{\beta/c}) e^{-\frac{\beta y^2}{2c}} cos(kx - \omega t)$$

where $\omega = ck$ is the frequency of the wave, m is the meridional mode and H_m is a Hermite polynomial of order m (Gill, 1982, and references therein). The meridional mode refers to the north-south structure of the solution, given by the Hermite polynomials; the first two solutions are shown in Figure 1.9, corresponding to the first two meridional mode Rossby waves. Note that the Kelvin wave solution is sometimes referred to as the $m = -1$ meridional mode. The general dispersion relation is given by

$$\left(\frac{\omega}{c}\right)^2 - k^2 - \frac{\beta k}{\omega} = \frac{(2m+1)\beta}{c_1}.$$

The dispersion relation gives, for each meridional mode m, the wavenumber k and frequency w of the various wave solutions; these are plotted in Figure 1.10. The solutions for $m \geq 1$ divide into two classes; the equatorial gravity waves and the equatorial Rossby waves. The dispersion relation for equatorial gravity waves is given by

$$\omega^2 = (2n+1)\beta c + k^2 c^2.$$

We will focus here on the Rossby wave case, for which $(\omega/c)^2$ is small and the dispersion relation approximates to

$$\omega = \frac{-\beta k}{k^2 + (2m+1)\beta/c}$$

with an error less than 2% for the first baroclinic mode (Gill, 1982). For long Rossby waves, k^2 is small and the solution approximates to

$$\omega = \frac{-c_1 k}{2m+1}$$

thus long equatorial Rossby waves of the first meridional mode travel westwards with phase speeds of approximately $1/3$ the Kelvin wave phase speed. For wind forcing with a broad meridional scale, the first meridional mode Rossby wave is most effectively forced, and therefore dominates in the response to the MJO, as we will see in the results. There is another class of waves for which $m = 0$ which behaves like a Rossby wave for large negative k and like a gravity wave for large positive k. It is therefore referred to as the mixed Rossby-gravity wave (or sometimes as the Yanai wave), whose phase velocity can

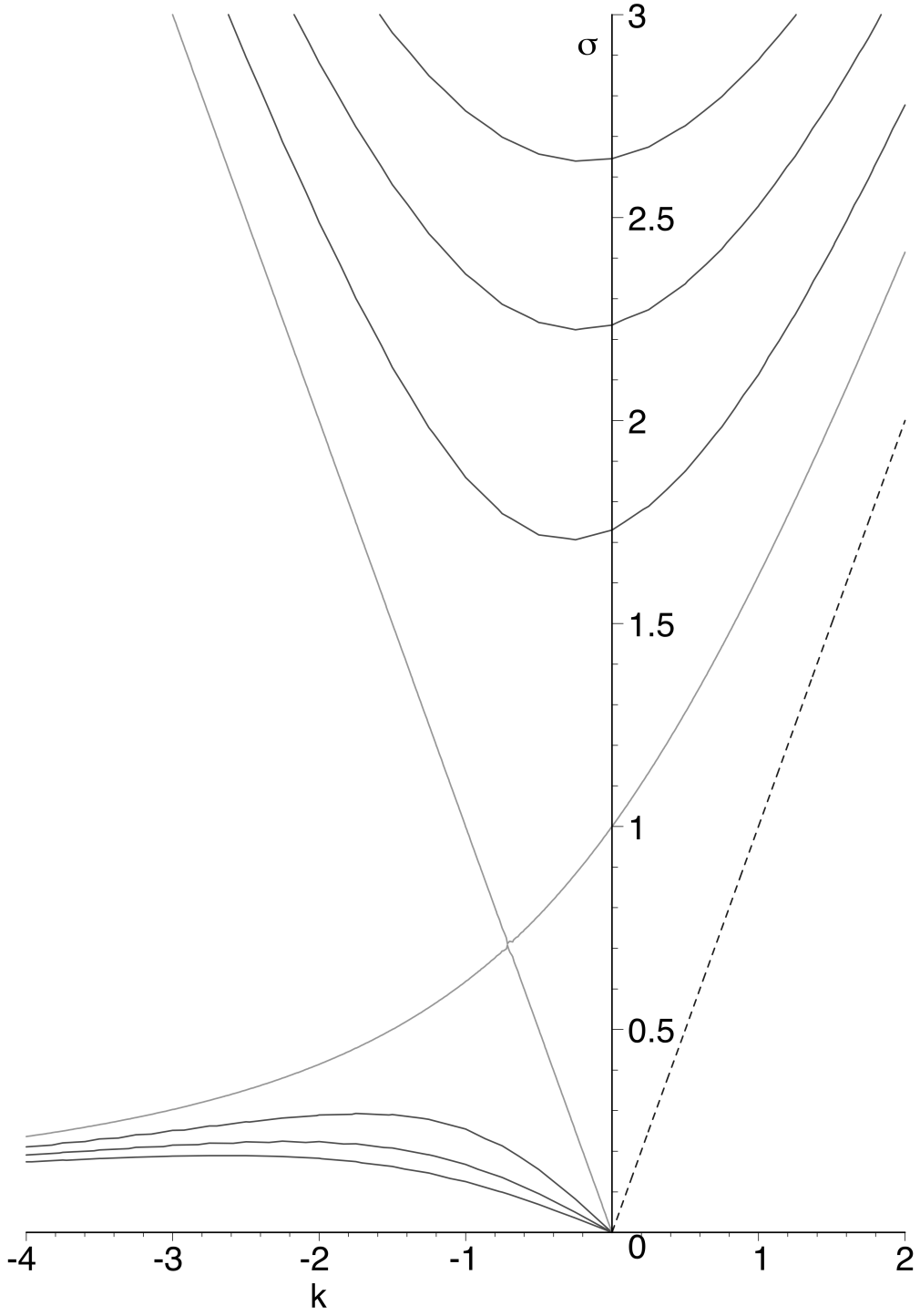

Figure 1.10: Dispersion curves for equatorially trapped waves. k has units of $\sqrt{\beta/c}$, and ω has units of $\sqrt{\beta c}$

be eastwards or westwards depending on wavelength. Its dispersion relation is given by

$$(\omega + ck)\left(\frac{\omega}{c} - k - \frac{\beta}{\omega}\right) = 0.$$

1.2.3 Reflection at meridional boundaries

Reflection of equatorial waves at meridional boundaries is fundamental for the generation of much of the oceanic variability of the tropical regions. The theory of wave reflection at meridional boundaries is covered in Moore (1968), Moore and Philander (1977), and Clarke (1983, 1991). We direct the reader to these for a full description and provide only an overview of the most important points here.

Moore and Philander (1977) show how the problem of reflection at a western boundary is possible to solve by a closed, finite series of reflected waves. This is possible because the incoming westward-propagating waves can be easily balanced by the reflected eastward-propagating Kelvin and mixed Rossby-gravity wave solutions. Note that it is the group velocity of these waves that are important since this is associated with the energy transmitted by the wave; thus it is possible to have eastwards propagating Rossby wave energy for sufficiently short wavelengths. The full solution includes such reflected Rossby waves, but only waves with an equal or lower meridional mode and the same meridional symmetry as the incoming Rossby wave. Therefore, if the incoming wave has an even meridional mode and is thus anti-symmetric, the reflected waves will all have even meridional modes lower than the mode of the incoming wave, and will also be anti-symmetric. The magnitude of all the reflected waves is dependent on the wavenumber and frequency of the incident wave; reflected Kelvin waves will have the same sign as the incoming Rossby waves, while the reflected Rossby waves will have the opposite sign. The latitude range over which the reflected waves are oscillatory in y is the same as that for the incoming waves. In this thesis we will mostly be concerned with the reflection of first meridional mode, long wavelength Rossby waves at the western boundary. Such a wave can only be balanced by reflection into an equatorial Kelvin wave of the same sign; e.g., a downwelling Rossby wave will generate a downwelling Kelvin wave.

For reflection at eastern boundaries, it is not possible to obtain a finite series solution; instead the solution includes an infinite series, but this was shown by Moore (1968) to represent meridionally-propagating coastal Kelvin waves. There is also a reflected component that consists of a finite number of meridional modes (Clarke, 1983). This reflected component consists of Rossby waves when the frequency of the incoming Kelvin wave is low ($\omega < (1-\sqrt{2})\sqrt{\beta c}$), and consists of inertia gravity waves when the frequency

of the incoming Kelvin wave is high ($\omega > (1+\sqrt{2})\sqrt{\beta c}$); there are no reflected wave solutions for incoming frequencies between these two values so all the incoming energy is absorbed into coastal Kelvin waves (Clarke, 1983). For the low-frequency case (which is of more relevance to this study), the reflected component increases quasi-linearly to 100% as ω tends to zero, with increasing numbers of meridional modes included in the solution. Note that, for a given wave frequency, there is a critical latitude below which the incoming Kelvin wave energy will be reflected, and above which it will be absorbed into coastally trapped waves (Clarke and Shi, 1991). For the wave periods associated with the MJO, this latitude is between 5°-10°N/S of the equator, being slightly greater to the north due to the more meridional boundary here (to the south, the buondary becomes progressively more zonal towards Java). Therefore we might expect a slightly greater proportion of the incoming wave energy to be reflected in the northern portion of the Rossby waveguide.

A further complication to the reflection problem arises when realistic boundaries are considered, either due to alignment in a direction other than direct north-south, or due to the presence of gaps in the boundaries. Both of these considerations need to be taken into account for reflection at the Maritime Continent, either as a western boundary to the Pacific, or as an eastern boundary to the Indian Ocean. Inclinations relative to the meridional increase the portion of the incoming wave energy that is absorbed into coastally-trapped waves and reduces the reflected portion (Clarke, 1992). In addition, reflectivity of equatorial Rossby waves at an eastern boundary perforated by gaps (representative of the Maritime Continent as a western boundary to the Pacific) is minimal; almost all the incoming energy is transmitted if any gaps exist within an equatorial Rossby radius of the boundary (Spall and Pedlosky, 2005). However, the Maritime Continent is fairly efficient at reflecting incoming Kelvin waves as an eastern boundary to the Indian Ocean (Clarke and Liu, 1993; Han, 2005; Fu, 2007; Oliver and Thompson, 2010), although this case has been given relatively little theoretical consideration.

Given that both boundaries of the Indian Ocean are relatively good reflectors, it raises the possibility of resonant modes of oscillations. The theory underlying such resonant modes was covered by Cane and Moore (1981), and involves only long Rossby waves and Kelvin waves; the short, eastward propagating Rossby waves propagate too slowly to be

important. This theory has subsequently been used to explain dynamical equatorial oscillations in the Indian Ocean, from the semi-annual cycle (Clarke and Liu, 1993; Han *et al.*, 1999; Fu, 2007), to spectral peaks in the intraseasonal frequency range (Han *et al.*, 2001; Han, 2005; Fu, 2007). Although these are resonant modes dependent on reflection at each boundary, their amplitude tends to be stronger in the eastern part of the Indian Ocean due to the stronger local surface forcing (Fu, 2007; Oliver and Thompson, 2010). The resonant periods (P) of these modes depends on the baroclinic modes, with $P = 107$ days, 54 days, 36 days, ... for the first baroclinic mode and $P = 176$ days, 88 days, 59 days, ... for the second baroclinic mode. The close agreements between the 176 and 88 day peaks for the second baroclinic mode and the observed semi-annual and 90 day spectral peaks respectively have been used to suggest that the second baroclinic mode could dominate over the first due to resonance effects. However, it seems quite plausible that resonance could occur for the first baroclinic mode, supported further by stronger projection of wind forcing onto that mode (as discussed in Section 1.2.1).

1.2.4 Coastally trapped waves

Coastal waves arise both through local wind forcing and as a remote response to equatorial Kelvin waves incident on an eastern boundary, as discussed above. Theoretical coastal Kelvin waves are non-dispersive and thus have the potential to propagate coherently far away from the initial forcing. However, more realistic treatment of the propagation of coastal waves suggests that this is not generally the case due to the combination of sloping topography with realistic stratification (Brink, 1982). Instead, true coastal waves do not behave like pure coastal Kelvin waves, but exhibit some of the properties of barotropic shelf waves and some of coastal Kelvin waves (Brink, 1982; Huthnance, 1985). Such waves retain the property of always propagating with the coastline on the right in the northern hemisphere, and on the left in the southern hemisphere. Their surface properties are also similar to the coastal Kelvin wave. However, these waves are dispersive, with the dispersion increasing with stratification until the dispersion curve rises above f; once this happens the waveguide becomes 'leaky' and coastal wave solutions no longer exist (Brink, 1991). The behaviour of such waves is dependent on the stratification parameter

S that takes into account the relative effects of stratification and bottom topography:

$$S = c_1^2 (f\Delta)^{-2},$$

where Δ is a measure of the shelf-slope width relative to ocean depth. At low latitudes, S is relatively large and for realistic shelf topographies the waves behave similarly to Kelvin waves, with cross-shelf flow near zero and a phase speed that is only slightly reduced from the pure Kelvin wave phase speed (Brink, 1982). However, at higher latitudes the waves become more like barotropic shelf waves; Allen and Romea (1980) show that such waves will behave similarly to barotropic shelf waves, albeit with slightly higher phase speeds. For each of these cases the precise nature of the shelf topography modifies the behaviour of the waves, so an accurate representation of bathymetry is required to simulate such processes well. In particular, the distance that such waves propagate coherently may be dependent on this bathymetry, with implications for the results shown in later chapters.

1.3 Motivation for present work

Although the MJO has been studied for four decades, there remains much about it we fail to understand. One element of this is its interaction with ocean dynamics. Although it has been shown that the MJO is effective at forcing equatorial ocean Kelvin waves (e.g., Hendon *et al.*, 1998) and that these can in turn trigger El Niño events (McPhaden, 1999), there remains a lack of understanding as to the role that ocean dynamics may play as a forcing mechanism for the MJO itself. Given that SST variability is known to be important for the MJO (e.g., Flatau *et al.*, 1997; Shinoda *et al.*, 1998; Woolnough *et al.*, 2000), and that equatorial dynamics can influence SSTs (Kessler *et al.*, 1995; Zhang, 2001), it seems reasonable to question whether the dynamics might influence the MJO. If so, this could be useful for prediction, since the typical timescales over which equatorial ocean waves are predictable are considerably longer than the time scale over which the MJO is predictable (three weeks at best, see Kang and Kim, 2010; Vitart and Molteni, 2010; Rashid *et al.*, 2011). Such forcing could also potentially be used to understand the sporadic and intermittent nature of the MJO. In addition, the dynamic ocean response to the MJO is worth studying, regardless of potential feedbacks, due to implications for

ocean circulation, chemistry and biology. The thesis consists of three chapters which examine the global dynamical ocean response to the MJO, indicate the role for the ocean dynamics to modulate MJO variability in turn, and examine the potential to use these relations to predict the initiation of 'primary' Madden-Julian events. The results of these three chapters have been published, in Webber *et al.* (2010), Webber *et al.* (2012a), and Webber *et al.* (2012b), respectively. The relative contribution of the various authors and the state of publication is indicated at the start of each chapter. The numerical model used is detailed in Chapter 4, and the overall conclusions from this work presented in Chapter 6.

Chapter 2

A dynamical ocean feedback mechanism for the Madden-Julian Oscillation

2.1 Preface

This chapter consists of a paper published in the Quarterly Journal of the Royal Meteorological Society, in April 2010, with the same title (Webber *et al.*, 2010). The manuscript is largely unchanged from the published paper apart from minor superficial changes to the figures and minor changes to the text, as well as the addition of the figure showing temperature advection. BGMW was responsible for the majority of the work, under supersvision by AJM and KJH, who provided scientific input and helped revise the text for publication. The comments of Paul Roundy and an anonymous reviewer also helped to improve the manuscript.

2.2 Abstract

Composite analysis is applied to study the dynamical ocean response to Madden-Julian (MJ) events, measured by anomalies in sea surface height from the merged TOPEX/Poseidon–European Remote Sensing satellite altimetry data set. In each of the tropical ocean basins, significant equatorial waves are forced, which are shown to modulate the sea surface temperature (SST) by 0.2–0.3°C in the absence of strong surface heat fluxes. In the Indian

Ocean there is a clear dynamical response which may play a significant role in generating later MJ events. Surface westerly winds, associated with the active phase of the Madden-Julian Oscillation (MJO), force an eastward-propagating oceanic downwelling equatorial Kelvin wave, which, on reaching the eastern boundary at Sumatra, forces reflected downwelling equatorial Rossby waves and coastal Kelvin waves. The coastal Kelvin waves propagate southwards towards northern Australia and northwards into the Bay of Bengal, and will be important for local physical, chemical and biological processes. The equatorial Rossby waves propagate westward across the Indian Ocean, arriving in the western Indian Ocean approximately 80–100 days after the initial Kelvin wave was generated. The arrival of these waves generates warm SST anomalies which leads to convection and may trigger the next but one MJ event, or amplify the low-frequency tail of the MJO. This constitutes a coupled feedback mechanism from the ocean dynamics onto the MJO, somewhat similar to the delayed oscillator mechanism for the El Niño-Southern Oscillation.

2.3 Introduction

At intraseasonal time scales the Madden-Julian Oscillation (MJO) is the primary source of tropical atmospheric variability. It consists of eastward-propagating regions of enhanced and suppressed convection and rainfall, associated with baroclinic wave structures evident in the wind and pressure fields (Madden and Julian, 1971, 1972). The MJO is a quasi-periodic occurrence with a broad spectral signal. It is typically defined by a period of $\sim$30–60 days but is associated with convective variability over a broader spectral range (Salby and Hendon, 1994), including scale interactions with high frequency convection (Majda and Biello, 2004; Batstone *et al.*, 2005). The MJO is most active in the warm pool of the Indian Ocean and the western Pacific, but it modulates atmospheric variability globally (Matthews *et al.*, 2004; Donald *et al.*, 2006), with significant impacts on rainfall, agriculture and business. For a full review of the MJO, see Chapter 1, Zhang (2005), and Lau and Waliser (2005).

The MJO forces a substantial thermodynamic response in the surface layers of the ocean (Jones *et al.*, 1998; Woolnough *et al.*, 2000; Waliser *et al.*, 2003). Within the warm pool, the anomalous surface winds of the MJO combine with climatological surface westerlies to produce an asymmetrical total wind speed signature that is enhanced (suppressed)

during westerly (easterly) anomalies. These winds lead to variations in the latent heat flux from the ocean, which is closely related to wind speed. The shortwave flux is also modulated by cloud cover during the MJO: the enhanced (suppressed) convective phase leads to a reduction (increase) in shortwave flux and thus cooling (warming).

Therefore, when there is active convection over the central Indian Ocean, the reduced latent heat flux warms the eastern Indian Ocean while the reduced shortwave and increased latent heat fluxes cool the western Indian Ocean, potentially leading to enhancement (reduction) of convection to the east (west) and thus eastward propagation. The reverse process may account for the eastward propagation of the subsequent suppressed convective anomalies. The surface fluxes combine to generate sea surface temperature (SST) variability of $\sim$0.15–0.35°C (Shinoda *et al.*, 1998), which precede the convective anomalies by a quarter of a cycle, consistent with a potential feedback between the two (Flatau *et al.*, 1997; Woolnough *et al.*, 2000).

There remains considerable debate over the relative importance of this oceanic thermodynamic coupling compared with other, atmospheric-only mechanisms which have also been suggested to explain the MJO. These mechanisms include atmospheric instability linked to frictional moisture convergence (Hendon and Salby, 1994), the interaction between convection and atmospheric Kelvin and Rossby waves (Matthews, 2000), external forcing from the mid-latitudes (Hsu *et al.*, 1990), and internal atmospheric multiscale interactions (Majda and Biello, 2004). However, coupled models generally perform better at simulating the MJO than atmosphere-only models, although the degree of improvement varies from minimal (Hendon, 2000) to more substantial (Inness and Slingo, 2003). Additionally, intraseasonal SST anomalies can force realistic atmospheric MJO behaviour in atmosphere-only models (Woolnough *et al.*, 2001; Fu and Wang, 2004; Matthews, 2004b). It is therefore clear that there is at least the potential for SST anomalies to be a key component of the MJO, but that many other processes will also influence the behaviour of the MJO, and that their relative importance may vary from event to event.

Near the equator, low-frequency planetary-scale Kelvin and Rossby waves are a key component of the oceanic dynamics and energy budget. Equatorial Kelvin waves have typical wavelengths of the order of 10–15 000 km (Kessler *et al.*, 1995), with typical sea

surface height (SSH) perturbations of $\sim$10 cm (Giese and Harrison, 1990). The propagation speed of both Kelvin and Rossby waves depends upon the vertical structure of the waves (their "baroclinic mode") and the stratification of the background state through which they propagate.

Equatorial Kelvin waves are non-dispersive. Depending on the mean stability profile, typical theoretical wave speeds are in the range $c_1 = 2.4$–3.0 m s^{-1}, for the first baroclinic mode (Chelton *et al.*, 1998). Equatorial Rossby waves follow the dispersion relation

$$c = \frac{-\beta}{k^2 + (2n+1)\beta/c_e},$$

where k is the zonal wavenumber, $\beta \approx 2.3 \times 10^{-11}$ m^{-1} s^{-1} is the meridional gradient of planetary vorticity, and n is the meridional mode. Long Rossby waves (with small k) are non-dispersive, with phase speed $c = -c_e/(2n+1)$. Rossby waves with wavelengths of the order of half the width of the Indian Ocean basin are weakly dispersive, with phase speeds reduced relative to the long wave value by 15%. The meridional scale of equatorial Kelvin and Rossby waves is determined by the equatorial Rossby radius of deformation, $R = (c/2\beta)^{1/2}$.

Kelvin and Rossby waves perturb the thermocline depth by three orders of magnitude more than they perturb the SSH. Waves with a positive SSH signal correspond to a deeper thermocline and are thus termed "downwelling" waves. Conversely, waves with a negative SSH signal correspond to upwelling. Kelvin waves have a meridional structure of SSH and zonal current with a single maximum (or minimum) at the equator. In contrast, there are multiple meridional structures for equatorial Rossby waves, the simplest being the symmetrical $n = 1$ meridional mode wave which has maxima (or minima) at 2–5°N and 2–5°S (Chelton *et al.*, 2003).

The surface zonal wind anomalies of the MJO are one mechanism by which Kelvin and Rossby waves are generated. Battisti (1988) showed that a symmetric equatorial westerly wind burst generates downwelling Kelvin waves and upwelling Rossby waves through the Ekman divergence field, although the response is dependent on the meridional structure of the wind field. Downwelling waves deepen the thermocline and warm the SST by reducing the entrainment of cold subsurface waters, while upwelling waves lead to enhanced entrainment and cooling (McCreary, 1983). The SST may also be modified

by zonal and meridional advection, which may be of first order importance in regions where a strong temperature gradient exists (Philander, 1981). Thus, the dynamical oceanic response to the MJO has the potential to generate SST anomalies which then feed back onto the atmosphere. Although the primary cause of intraseasonal SST variability within the region where the MJO is active comes from the surface fluxes, dynamical forcing still plays a substantial role and may locally contribute up to 50% of the total forcing (Waliser *et al.*, 2003).

In the eastern Pacific Ocean, the first baroclinic mode equatorial Kelvin wave period is observed to be around 70 days. Although this is longer than the dominant period of the MJO, the MJO is broadband with spectral power extending to $\sim$95 days (Salby and Hendon, 1994). In addition, closer examination of Kelvin waves forced by the MJO shows a transient decline in phase speed during periods of enhanced MJO activity, which would reduce the observed frequency of the waves in the eastern Pacific and may thus account for the frequency difference between the waves and the MJO (Roundy and Kiladis, 2006). The eastward propagation of the forcing allows resonance to occur, so that the MJO will more efficiently generate such waves than stationary wind bursts (Hendon *et al.*, 1998). The MJO-induced waves remotely force SST fluctuations of more than 0.5°C (Zhang, 2001), deepen the thermocline by as much as 50 m (Kessler *et al.*, 1995) and play a role in the generation and amplification of El Niño events (Kessler *et al.*, 1995; McPhaden, 1999; Edwards *et al.*, 2006).

Outside of the Pacific Ocean, the dynamical response to the MJO has been less well studied. Katz (1997) showed that Kelvin waves in the Atlantic have an intraseasonal periodicity of $\sim$40–60 days, consistent with the time scale of the MJO. However, the predominant forcing mechanism for these waves was found to be the seasonal cycle in the trade winds. Han *et al.* (2008) found that the primary cause of Atlantic intraseasonal variability in SSH and SST was Kelvin wave activity forced by local wind variability. They noted that this local variability may be remotely influenced by the MJO (Foltz and McPhaden, 2004), as well as by convective variability in the Amazon basin, but did not conclusively show evidence for an interaction with the MJO.

In the Indian Ocean, MJO-related Kelvin and Rossby wave variability has been observed at multiple time scales; intraseasonal spectral peaks have been found at 45 and 90

days (Han *et al.*, 2001), as well as lesser peaks at 70, 62.5 and 58.8 days (Fu, 2007). The 90-day peak appears to be the preferred time scale of the ocean dynamics and may enhance atmospheric variability on such time scales (Han *et al.*, 2001). The spectral peaks are strongest at around 4–5° north and south of the equator, consistent with equatorial Rossby wave structures (Chelton *et al.*, 2003). The MJO is known to interact with the Indian Ocean Dipole (IOD; e.g., Saji *et al.*, 1999) through the ocean dynamics; Rao and Yamagata (2004) showed that Kelvin waves forced by the MJO can terminate IOD events. In addition, Shinoda and Han (2005) found that sub-monthly variability in the central and eastern Indian Ocean, which is correlated with the IOD, can force an equatorial Kelvin wave response which may then feed back to the IOD by modulating the SST. Nevertheless, the interaction between the dynamics of the Indian Ocean and the MJO remains poorly understood.

The MJO undergoes a strong seasonal cycle; it is most coherent during boreal winter when it propagates zonally along the equator, while during boreal summer there is more northward propagation and interaction with the Asian monsoon (Wang and Rui, 1990). This seasonal cycle affects the dynamical response, which will be most efficiently generated by the zonally propagating, equatorial component of the MJO. In addition, the frequency of the MJO is influenced by seasonality (Pohl and Matthews, 2007), with implications for the resonant amplification of the ocean waves.

There evidently remains much scope for studying ocean dynamics over the MJO life cycle. This study elucidates the dynamic ocean response by using a compositing technique to study the time and phase evolution of SSH and SST in relation to the MJO. The use of satellite altimetry to study the MJO life cycle through composites is novel; previously the focus has generally been the connection between the MJO and the El Niño-Southern Oscillation (ENSO) in the Pacific (Edwards *et al.*, 2006), or on studying intraseasonal ocean dynamics in the Indian Ocean but without reference to the phase-by-phase evolution of the MJO (Han *et al.*, 2001; Han, 2005; Fu, 2007). Various atmospheric fields are studied to investigate atmosphere-ocean interaction and feedbacks, including the potential for the MJO-forced dynamical waves to modulate the SST and feed back onto the MJO convection. Section 2.4 describes the data sets used in this study and Section 2.5 outlines the methodologies used. The results are presented in Section 2.6, starting with the global

response and then focusing on the Pacific, Atlantic and Indian Oceans. The conclusions are discussed in Section 2.7.

2.4 Data

The merged TOPEX/Poseidon–Earth Remote Sensing (T/P–ERS) satellite altimetry data set is used for the SSH analysis (Fu *et al.*, 1994). This was chosen in preference over TOPEX/Poseidon data alone since the combination of multiple satellite data sets enhances spatial resolution and improves variance (Ducet *et al.*, 2000; Le Traon *et al.*, 2001), although there is a slight decrease in effective temporal resolution (Greenslade *et al.*, 1997). The "reference" data set, which is a homogeneous data set based on two satellites with the same ground-track, is used as opposed to the "updated" one, which uses up to four satellites at a given time. This sacrifices the potential for enhanced accuracy with improved satellite coverage in order to maintain consistent sampling in time. The data were obtained on a 0.25° grid as weekly maps (representing an instantaneous snap-shot derived from optimal interpolation) for the period from 14 October 1992 to 23 January 2008, and then interpolated using cubic splines to daily values. SST data were obtained from the Tropical Microwave Imaging (TMI) satellite (Kummerow *et al.*, 2000). The data used are daily maps of the 3-day average SST at 0.25° resolution for the period of 1 January 1998 to 17 December 2008.

Outgoing longwave radiation (OLR) data from the Liebmann and Smith (1996) data set are used as a proxy for convective activity and rainfall. The data set is optimally interpolated onto a 2.5° grid and in this study the daily mean data from 1 January 1990 to 31 October 2008 are used. Surface (10 m) wind data and surface fluxes of latent heat, sensible heat, shortwave radiation and longwave radiation were obtained from the European Centre for Medium-Range Weather Forecasts (ECMWF) interim analysis (Dee *et al.*, 2011) for the period from 1 January 1998 to 1 January 2009.

The linear trend and annual cycle are calculated point-wise for each variable, then the mean, trend and first three harmonics of the annual cycle are subtracted from the data to produce detrended anomaly fields. These are then bandpass-filtered using a 20–200 day Lanczos filter. This broadband filter has been shown to efficiently exclude both high frequency noise and low frequency climate signals while retaining the MJO signal

and preserving the distinction between individual Madden-Julian (MJ) events better than a narrower (e.g. 30–70 day) filter (Matthews, 2000). The filter uses 241 symmetric weights, meaning that 120 days of data are lost at each end of the data set. All data sets are further truncated so that an integer number of calendar years of data are retained, thus avoiding seasonal bias. Note that very similar results were obtained when the data were not filtered.

2.5 Methodology

The Wheeler-Hendon (WH) index (Wheeler and Hendon, 2004) is used to track MJO activity. This index is based on a multi-variate principal component analysis of high-pass filtered OLR and zonal winds at 850 and 200 hPa. The index is produced in real time, retains a high proportion of temporally coherent variance in the 30–80 day range and is independent of season. Every day is assigned to one of the eight phases defined by the two principal components (RMM1 and 2) of the index. Phase 1 corresponds to minimum convection over the Maritime Continent and the initiation of active convective anomalies in the western Indian Ocean. These anomalies move eastwards in each successive phase; by phase 4 the positive convective anomalies overly the Maritime Continent while the suppressed convection has propagated into the western Pacific. A new region of suppressed convection originates in the western Indian Ocean at phase 5; phases 5–8 are thus equivalent to phases 1–4 with anomalies of the opposite sign.

The WH index is becoming an accepted way to track MJO activity and has been used by many MJO studies since it was introduced (Donald *et al.*, 2006; Pohl and Matthews, 2007; Matthews, 2008). However, as with any index of the MJO, it will include variability with different modes of behaviour and timescales, such that the results will depend slightly on the definition of the MJO. Note that the WH index does contain variability not associated with the MJO, especially atmospheric Kelvin waves which can contribute substantially (Roundy *et al.*, 2009); however, the compositing technique used here should reduce the impact of such noise unless that noise systematically varies in response to the MJO in a way which projects onto the oceanic response.

To investigate this oceanic response, composites are created separately for each MJO phase, using all days within that phase when the amplitude of the WH index exceeds an arbitrary threshold value of 1.5. This value was chosen to select the stronger MJO

events (whose impact on the ocean should be stronger and more coherent), as opposed to the threshold value of 1 chosen by Wheeler and Hendon (2004). Composites for a given phase are generated by taking the mean of the composited field over all days that lie within that MJO phase and exceed the threshold. Since an average MJO cycle takes around 48 days, each phase lasts for $\sim$6 days. However, this can vary greatly depending on the MJ event (Salby and Hendon, 1994), as well as season and ENSO phase (Pohl and Matthews, 2007). This variation means that signals analysed with respect to phase can represent a combination of events with different individual life times. Therefore, although the eight MJO phase composites provide a robust picture of the evolution of the MJO in a particular variable, the exact time dependence of these signals is uncertain. Hence, time-lagged composites are also generated by adding or subtracting a set number of days from all these dates. These represent a more accurate and robust method for evaluating the time-evolution of the physical processes, and tend to produce more accurate estimates of phase speed than compositing on MJO phase (Matthews *et al.*, 2010).

The resulting composite anomaly fields are tested for local (grid-point) significance at the 95% level using a resampling technique (Wilks, 1995). The histogram of the null distribution for this test is generated at each grid point from 1000 Monte Carlo simulations. Each simulation consists of a composite which has the same number of MJ events, each with the same length as the original, but where these events are randomly selected. The dates of the events maintain seasonality through the constraint of lying within 15 days of the original composite calendar date, but are freely chosen from any year. Note that since the resampling technique is a non-parametric test, it is not necessary for the the number of degrees of freedom to be explicit in the formulation. However, this number is implicitly assumed to be the number of MJ events and remains constant throughout the simulations.

Each grid point value for each composite is then tested for local significance at the 95% level by comparison with the 2.5th and 97.5th percentile values of the null distribution. Field significance is also tested for each composite by generating a null distribution of the fractional area of the map that is locally significant at the 95% level from the Monte Carlo simulations. By definition, this distribution has a mean value of 5% but spatial correlations tend to increase the spread and skewness of the distribution such that the 95th percentile often exceeds 10%, especially when the test is done over a smaller area. For

a map of composite anomalies to pass the field significance test, the fraction of the map which is locally significant must exceed this value. This would be expected whenever there is a genuine physical process occurring, since the true response will be added to the 5% of anomalies expected to be present by chance.

2.6 The Dynamic Ocean Response

2.6.1 Global response

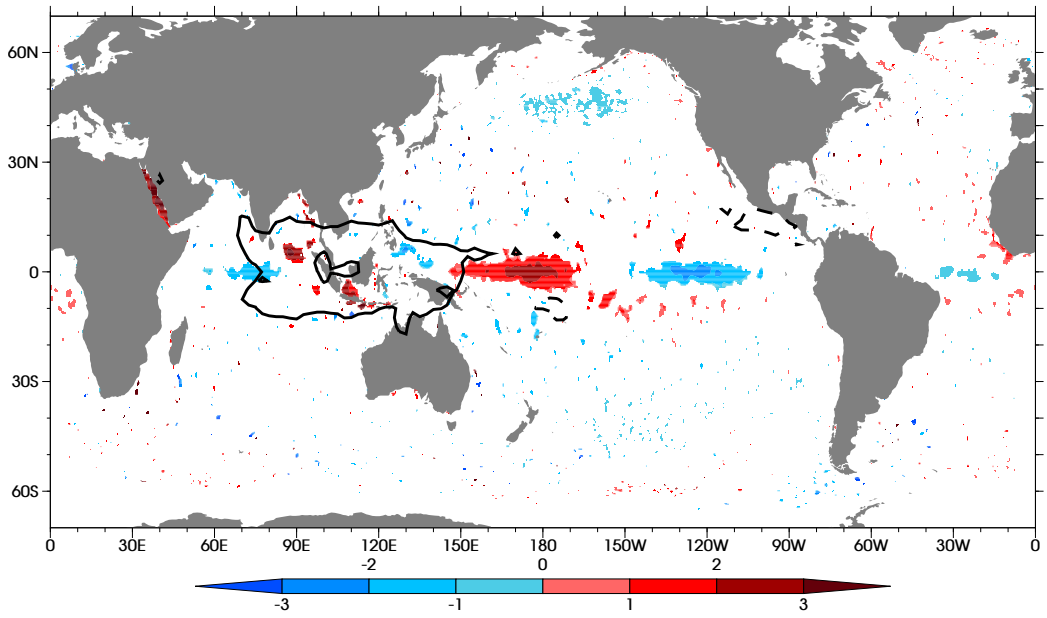

Figure 2.1: Composite anomalies of sea surface height for phase 8 lag 0. The shading interval is 1 cm. Regions where the anomalies are not significant at the 95% level are masked such that only significant anomalies are visible. OLR is plotted as thick contours at ± 10 W m^{-2}; the negative contour is dashed. This composite passes the field significance test at the 95% confidence level.

As an overview of the global dynamic ocean response to the MJO, the SSH anomalies in phase 8, at lag 0, are shown in Figure 2.1. At this phase of the MJO, suppressed convective anomalies are located over the Maritime Continent, leading to surface easterly wind anomalies over the Indian Ocean (not shown). The band of significant negative SSH anomalies along the equator in the Indian Ocean indicates the presence of an upwelling equatorial Kelvin wave being forced by these overlying easterlies. The off-equatorial SSH maxima near the coast of Sumatra indicate a downwelling Rossby wave generated by reflection of a downwelling Kelvin wave earlier in the MJO cycle (Section 2.6.4), although this will be further amplified by the concurrent wind forcing. The preceding Kelvin wave has also forced downwelling coastal Kelvin waves which can be seen propagating around

the Bay of Bengal and southwards along the coast of Java. These waves will advect temperature and energy polewards, away from the warm pool. There is also evidence of energy propagation into the Indonesian seas, notably through the Sunda channel between Java and Sumatra, which may affect the variability of the Indonesian Throughflow.

In the equatorial Pacific, a full Kelvin wave (both positive and negative anomalies) can clearly be seen, with maximum SSH perturbations of $\pm$2–3 cm. The timing of the positive SSH anomalies (indicating downwelling) is consistent with the local forcing by the MJO in the western Pacific, but the magnitude of the negative anomalies (indicating upwelling) in the central Pacific, where there is no local forcing, demonstrates the potential for the MJO to remotely influence the local dynamics.

In the Atlantic Ocean there is a weak ($<$1 cm) but significant upwelling (negative SSH anomalies) Kelvin wave apparent at the equator, in addition to positive SSH anomalies along the coast and along 5°S. These latter anomalies are possibly due to coastal Kelvin and reflected Rossby waves respectively, generated by the downwelling Kelvin wave forced by the preceding MJ event.

In general, the extra-tropical anomalies are weaker and less coherent than the equatorial anomalies. However, there are spatially (and temporally; not shown) coherent regions of significantly negative SSH anomalies in both the north and south Pacific, near 50°N and 50°S respectively. It may be that these anomalies are associated with the atmospheric extra-tropical response to the MJO, which drives significant surface wind variability on the MJO time scale (Matthews *et al.*, 2004; Matthews and Meredith, 2004; Donald *et al.*, 2006, and others). Another possible cause is the interaction between the MJO and high frequency transient waves in the subtropical jets (Matthews and Kiladis, 1999). However, a detailed analysis of the extra-tropical response to the MJO is beyond the scope of this thesis. Here, we will focus on the tropical oceanic response.

2.6.2 Pacific Ocean

Because the dynamic response of the Pacific Ocean to the MJO has been well studied in relation to the link with ENSO (Kessler *et al.*, 1995; McPhaden, 1999; Edwards *et al.*, 2006, and others), it is useful to compare our composites with previous studies to provide

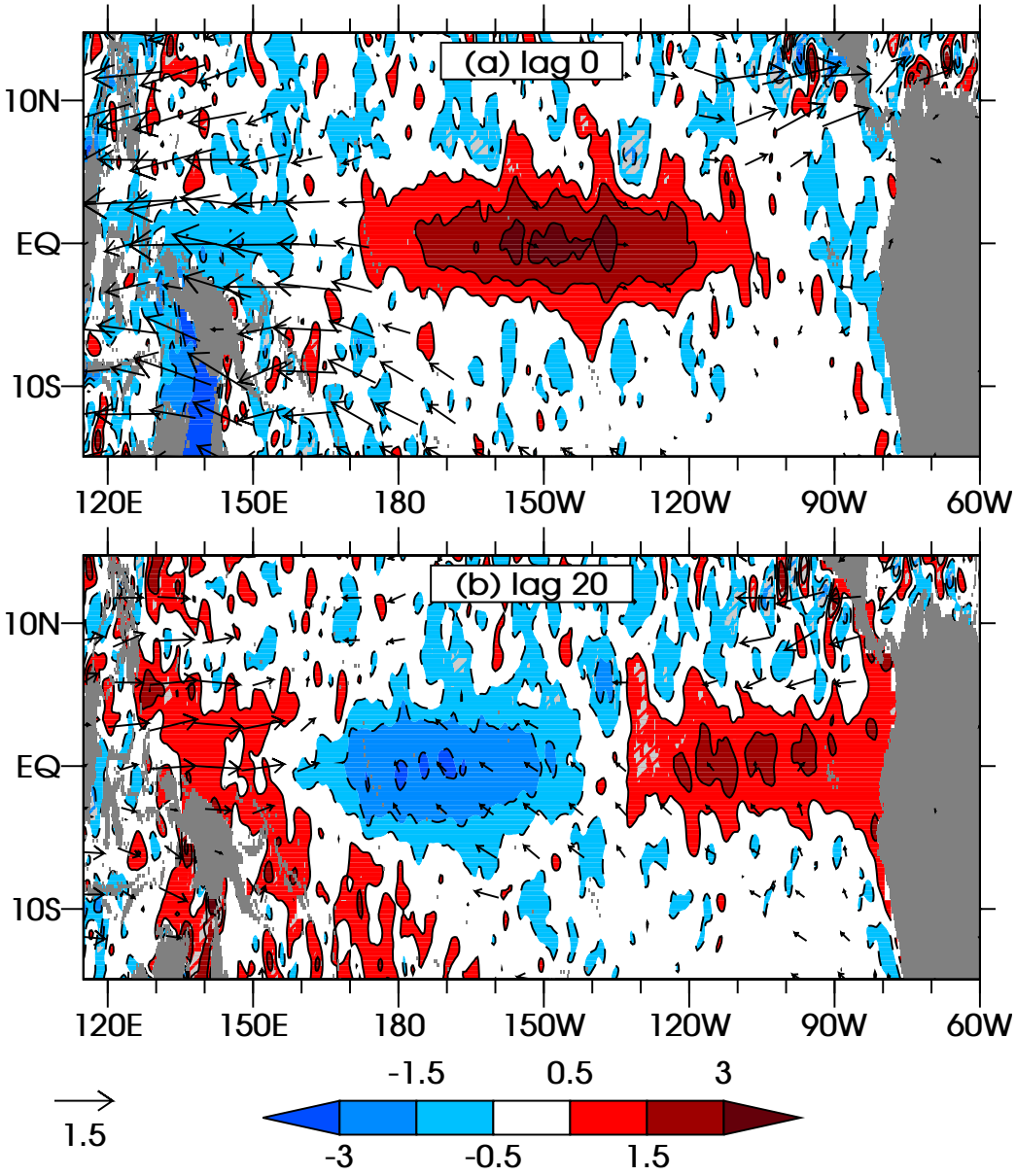

Figure 2.2: Composite anomalies of sea surface height for (a) phase 2 lag 0 and (b) phase 2 lag 20 days in the tropical Pacific. The shading and contour interval is shown (in cm) by the legend. Regions where the anomalies are not significant at the 95% level are hatched over such that only significant anomalies are clearly visible. Surface winds are plotted where either the u- or v-component is significant at the 95% confidence level; a scale vector of 1.5 m s^{-1} is shown. All composites pass the field significance test at the 95% confidence level.

a benchmark with which results presented later in this paper may be compared. Composites, time lagged with respect to phase 2 of the MJO, are shown in Figure 2.2. At lag 0, the downwelling (positive SSH anomalies) Kelvin wave present in the western Pacific in the phase 8 composite (Figure 2.1) has propagated eastward into the central Pacific, with maximum SSH anomalies of over 3 cm (Figure 2.2(a)). Phase 2 of the MJO represents a transition phase with suppressed convection propagating into the western Pacific accompanied by underlying easterly anomalies. The relationship between the atmospheric forcing and the oceanic response can be clearly seen as these easterly anomalies start to force a new, upwelling, Kelvin wave, which propagates to the central Pacific 20 days later (Figure 2.2(b)). At this time, the downwelling Kelvin wave has reached the coast of South America where it is subsequently transformed into coastal Kelvin waves. Downwelling Kelvin waves have been observed by the Tropical Atmosphere Ocean (TAO) buoy array to deepen the thermocline of the eastern Pacific and interrupt the thermal influence of climatological upwelling, potentially triggering El Niño events (Kessler *et al.*, 1995; McPhaden, 1999; Roundy and Kiladis, 2006).

The propagation speed of the Kelvin waves can be estimated from the composites; the downwelling wave is originally centered at around 140°W, reaching 100°W 20 days later. Thus its speed is approximately 2.6 m s^{-1}, consistent with the theoretical Kelvin wave speed for this region, of 2.4–2.6 m s^{-1} (see Chelton *et al.*, 1998, Figure 2). Previous theoretical and observational studies have suggested wave speeds nearer 2.3–2.4 m s^{-1} (Hendon *et al.*, 1998), but considering the uncertainty involved in estimating the Kelvin wave speed from only two composites, this is well within the reasonable range of values. In general, the results presented here are in good agreement with those from previous studies, suggesting that the methodology is valid.

2.6.3 Atlantic Ocean

Intraseasonal Kelvin waves in the Atlantic Ocean have been observed in response to the seasonal cycle (Foltz and McPhaden, 2004; Han *et al.*, 2008), but no conclusive link with the MJO has been found. Here, we examine the strength and coherence of the dynamic response to the MJO in our composites. In addition, the Atlantic Ocean represents an ocean basin without strong thermodynamic forcing by the MJO and is thus a good test of

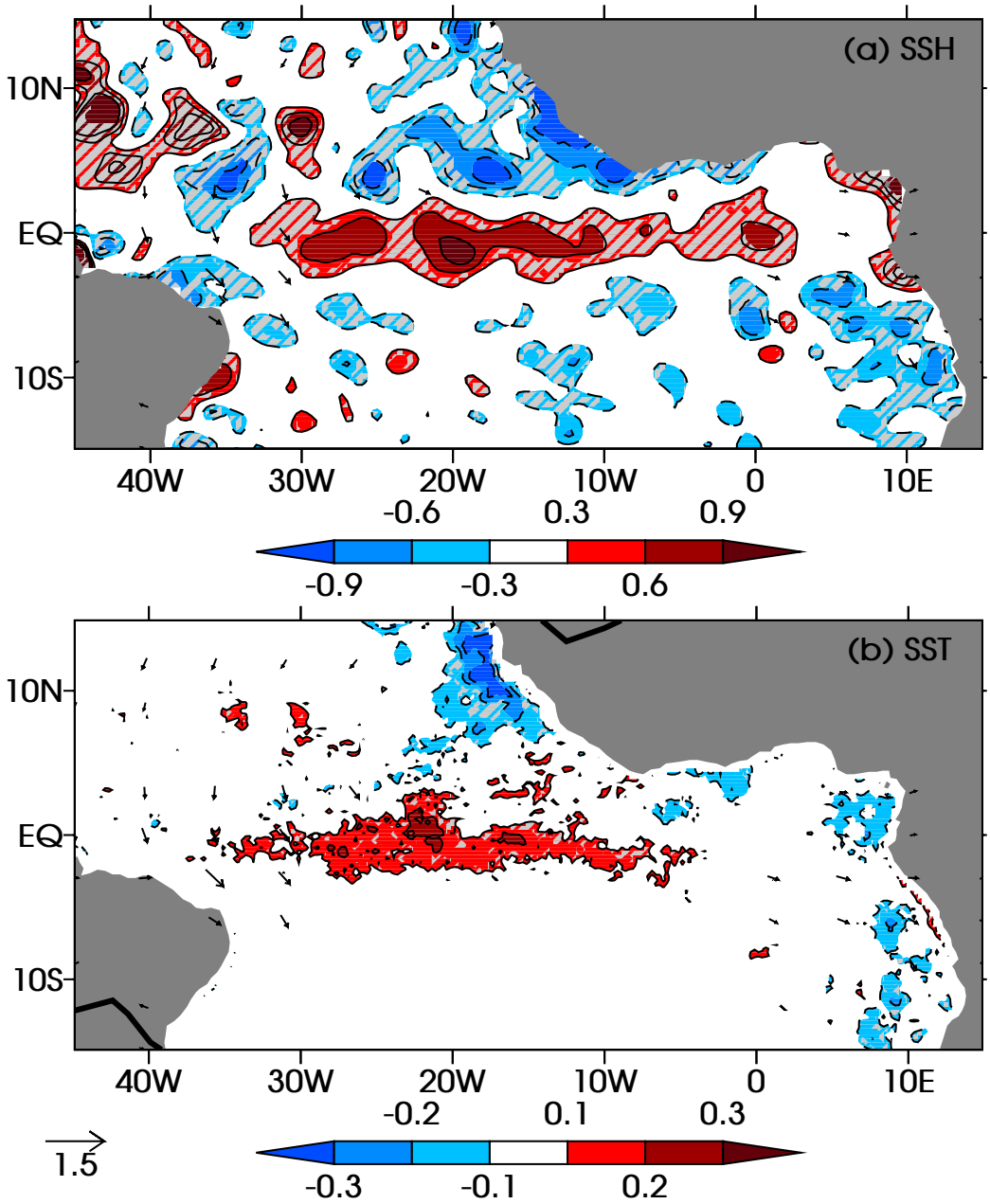

Figure 2.3: Composite anomalies of (a) sea surface height (b) sea surface temperature for phase 3 lag 0 of the MJO in the tropical Atlantic. The shading and contour interval is (a) 0.3 cm and (b) 0.1 °C. Surface winds are plotted where either the u- or v-component is significant at the 95% confidence level; a scale vector of 1.5 m s^{-1} is shown. Regions where the anomalies are not significant at the 95% level are hatched over in grey such that only significant anomalies are clearly visible. OLR is plotted as thick contours at ± 10 W m^{-2}; the negative contour is dashed. All composites pass the field significance test at the 95% confidence level.

the strength of the dynamically-induced SST anomalies.

In addition to the upwelling equatorial Kelvin wave in the Atlantic at phase 8 (Figure 2.1), there is a downwelling equatorial Kelvin wave which occurs at phase 3, lag 0 (Figure 2.3). Although the magnitude of the SSH anomalies is only a third of those seen in the Pacific, the wave is nevertheless significant and temporally coherent at other lags (not shown). The negative SSH anomalies along the African coast to the north and south are possibly due to the upwelling coastal Kelvin waves forced by the upwelling equatorial Kelvin wave shown in Figure 2.1. The significant wind anomalies are weak and do not coincide with the location of the Kelvin wave, implying weak wind stress. However, there is a broad region of westerly anomalies at phase 2 (not shown), which is likely to be the source of the downwelling Kelvin wave shown here.

The weakness of the wind and OLR anomalies also implies minimal surface flux anomalies of latent heat and shortwave radiation, allowing the relationship between the dynamical waves and the concurrent SST anomalies to be clearly seen (Figure 2.3(b)). Because downwelling waves deepen the thermocline and reduce entrainment, the downwelling equatorial wave leads to warm SST anomalies along the equator, while the upwelling coastal Kelvin wave is associated with cold anomalies. The SST anomalies correspond almost exactly with the location of the Kelvin waves, peak at over 0.2°C, and are significant at the 95% confidence level. Thus the remote response to the MJO in the Atlantic Ocean is substantial and drives SST fluctuations of the same order of magnitude as the flux-driven SST variability in the warm pool (Shinoda *et al.*, 1998).

2.6.4 Indian Ocean

2.6.4.1 Annual Average

We now focus on the Indian Ocean response, which is a key region of interest because it lies entirely within the core region of MJO activity. Therefore, any dynamically-induced SST anomalies will have a direct effect on the MJO. In addition, the Maritime Continent reflects a large proportion of incoming Kelvin wave energy as equatorial Rossby waves. The remainder of the incoming energy will be split between northward and southward propagating coastal Kelvin waves. The southward component will escape into the Pacific

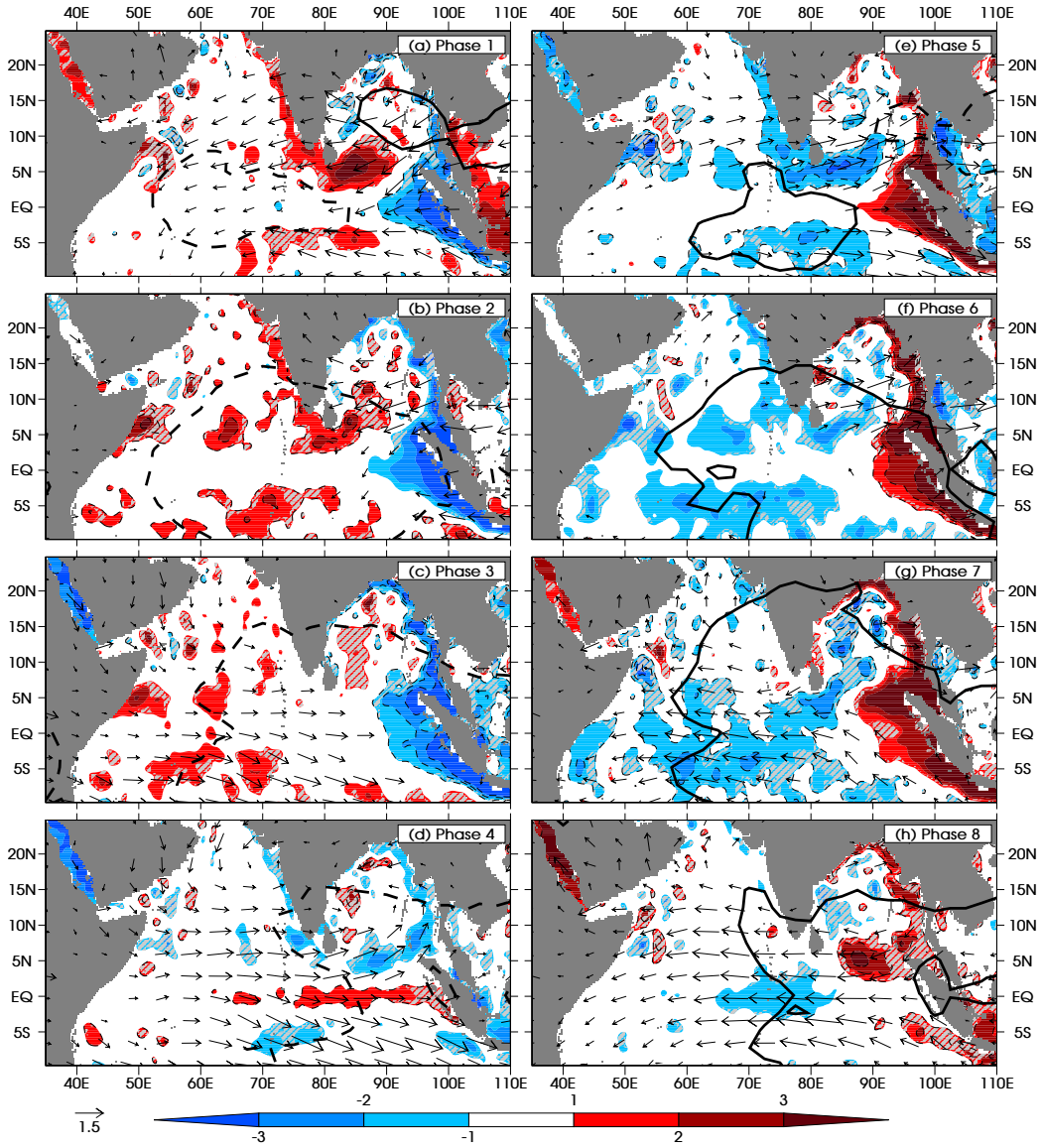

Figure 2.4: Composite anomalies of sea surface height for all 8 phases of the MJO. The contour and shading interval is 1 cm. Regions where the anomalies are not significant at the 95% level are hatched over such that only significant anomalies are clearly visible. Surface winds are plotted where either the u- or v-component is significant at the 95% confidence level; a scale vector of 1.5 m s^{-1} is shown. OLR is plotted as thick contours at ± 10 W m^{-2}; the negative contour is dashed. All composites pass the field significance test at the 95% confidence level.

but the northward component cannot propagate through the shallow Malucca straits between Sumatra and Malaysia and will thus propagate around the northern boundary of the basin. Therefore, in contrast to the Pacific, the majority of the wave energy will not radiate away from the forcing, but will instead remain trapped within the Indian Ocean, with the potential for resonant coupling between the MJO and the dynamical response.

Figure 2.4 shows the SSH response in the Indian Ocean for all eight phases of the MJO, with the concurrent OLR and surface wind anomalies overlaid. The upwelling

equatorial Kelvin wave generated by the easterly anomalies at phase 8 (Figure 2.1 and Figure 2.4(h)) reaches the coast of Sumatra by phase 1 (Figure 2.4(a)) where it triggers upwelling coastal Kelvin waves. These waves propagate polewards over the subsequent phases. The southward component propagates along the coasts of Sumatra and Java and then continues into the Indonesian seas, thus escaping the Indian Ocean. The northward-propagating coastal Kelvin wave circumnavigates the Bay of Bengal by phase 3, when a narrow region of negative SSH anomalies can be seen along the east coast of India. At phase 4, negative anomalies can be seen on the western coast of India, indicating that the coastal Kelvin wave has propagated around the tip of India and into the Arabian seas.

At phase 3, a first meridional mode (n=1) equatorial Rossby wave is generated by reflection of the incoming Kelvin wave at the eastern boundary, indicated by the dual SSH minima at 2–5°N and S. The westerly wind anomalies at phases 3 and 4 also generate positive wind stress curl which will lead to anomalous upwelling by Ekman divergence and then amplify and extend the reflected wave. This equatorial Rossby wave propagates westward, reaching the longitude of the tip of India at phase 5. The northern part of the Rossby wave interacts with the coastal Kelvin wave, amplifying the negative anomalies along the western coast of India. At phase 7, the easterly wind anomalies weaken the equatorial Rossby waves and generate a new upwelling equatorial Kelvin wave, at which point the cycle begins again.

In addition to this cycle in the upwelling waves, there is an equivalent cycle in the downwelling (positive SSH anomaly) waves. The downwelling equatorial Kelvin wave is forced at phase 4, transforms into coastal Kelvin waves at phase 5, which themselves circumnavigate the Bay of Bengal before coinciding with reflected Rossby waves at the tip of India at phase 1. The Rossby waves continue to propagate westwards, initially amplified by the easterly winds until the westerly winds which begin at phase 3 reduce their amplitude and force the new downwelling equatorial Kelvin wave at phase 4. Thus, the cyclical nature of the MJO can be clearly seen in the composites of the dynamical ocean response, which are roughly inverted half a cycle later (compare the left and right hand panels of Figure 2.4).

The coastal Kelvin waves propagating around the Bay of Bengal will affect the local

upwelling and the coastal currents; for example there is known to be intraseasonal variability in the East India Coastal Current (Durand *et al.*, 2009), which is likely to be partly due to such waves. The subsequent propagation along the west coast of India supports the findings of Vialard *et al.* (2009) that variability in current velocities near 15°N, 73°E is dominated by strong intraseasonal variability induced by coastal Kelvin waves similar to those found here and forced by the equatorial winds of the MJO.

This timing and interaction of the various waves forced by the surface winds is similar to that found by Valsala (2008) in an idealised modelling study of the oceanic response to seasonal variability using a patch of equatorial zonal wind stress. The similarity of the results shows that similar oceanic mechanisms are important for modulating the oceanic response to the seasonal cycle and the MJO. However, the shorter time scale of the MJO allows a different resonance to occur. As discussed above, the reflected upwelling equatorial Rossby wave generated at phase 3 is amplified by the reversal of the MJO-induced surface winds to westerlies during phases 4–5 and the resulting pattern of equatorial convergence and off-equatorial divergence. Similarly, the surface easterlies amplify the reflected downwelling waves at phases 7–1. In contrast, the longer lived seasonal forcing would continue to enhance the equatorial Kelvin waves and suppress the reflected equatorial Rossby waves.

The Kelvin waves appear to be generated in the central Indian Ocean rather than the western part. This is likely due both to the relative weakness of the wind anomalies in the western Indian Ocean and resonant amplification between the eastward propagating forcing and the oceanic Kelvin waves, similar to that found in the Pacific by Hendon *et al.* (1998). These waves continue to amplify upon arrival at the coast of Sumatra as easterly wind anomalies along the equator and south-easterly anomalies along the coast of Sumatra continue to generate upwelling. As the enhanced convective anomalies of the MJO propagate into the Maritime Continent from phase 2 to phase 4, the Indian Ocean wind anomalies weaken and then reverse, at which point a downwelling equatorial Kelvin wave begins to form. A similar mechanism amplifies this downwelling Kelvin wave at phase 5 before the winds reverse again at phase 6.

In addition to the waves clearly evident in the equatorial Indian Ocean, there is a significant and cyclical response in the Red Sea, with positive anomalies during phases

7 to 1, and negative anomalies during phases 3 to 5. The anomalies peak at over ± 3 cm and appear to be a response to the local wind forcing which reverses from north-westerly in phase 3 to south-easterly in phase 7. It is plausible that this represents net transport in response to the intraseasonal winds, but the quality of the altimetry data set may be questionable within a narrow and shallow region such as the Red Sea.

While the composites by MJO phase (Figure 2.4) give a robust overview of the main features of the dynamical ocean response to the MJO, the broadband nature of the MJO means that it is not possible to accurately calculate phase speeds for the waves, nor to study their time evolution in detail. To investigate this further, Figure 2.5 shows time lag composites of SSH and SST lagged with respect to phase 1. The positive SSH anomalies of the downwelling equatorial Rossby wave originate at lag -30 (Figure 2.5(a)) in the eastern Indian Ocean when the downwelling Kelvin wave generated during the previous MJO cycle reflects at the Sumatran coast. This corresponds approximately to the MJO phase 5 panel in Figure 2.4(e). The positive SSH anomalies can then be tracked as they propagate westwards through to lag 60, when they reach the coast of Africa. Hence there is a 90-day time scale from the oceanic Rossby wave propagation, which is twice the 45-day time scale of the canonical MJO.

Given the cyclical anomalies shown in Figure 2.4, it might be expected that the SSH anomalies at lag 0 (Figure 2.5(a)) would be repeated after a full cycle of the MJO, i.e., around lag 50 (Figure 2.5(h)). However, this is not the case, consistent with the ocean dynamics having a different time scale to the forcing. Indeed, the Rossby wave signal does not arrive in the western Indian Ocean until lag 60, implying that the positive SSH anomalies in this region in the MJO phase maps (Figure 2.4(c)) are the aliased signal from the arrival of Rossby waves a full MJO cycle after they were forced. The difference in time scales between the intraseasonal dynamics of the Indian Ocean and the MJO has been noted by Han *et al.* (2001), and Han (2005), who suggested that the shift is due to a resonant response of the equatorial Indian Ocean at the 90-day timescale.

In Figure 2.5, the relationship between the SSH and SST anomalies is generally weak, compared with the close correlation for the Atlantic composites shown in Figure 2.3. This is perhaps unsurprising given the strength of the surface flux anomalies associated with the MJO in the Indian Ocean. The total flux anomaly is primarily composed of

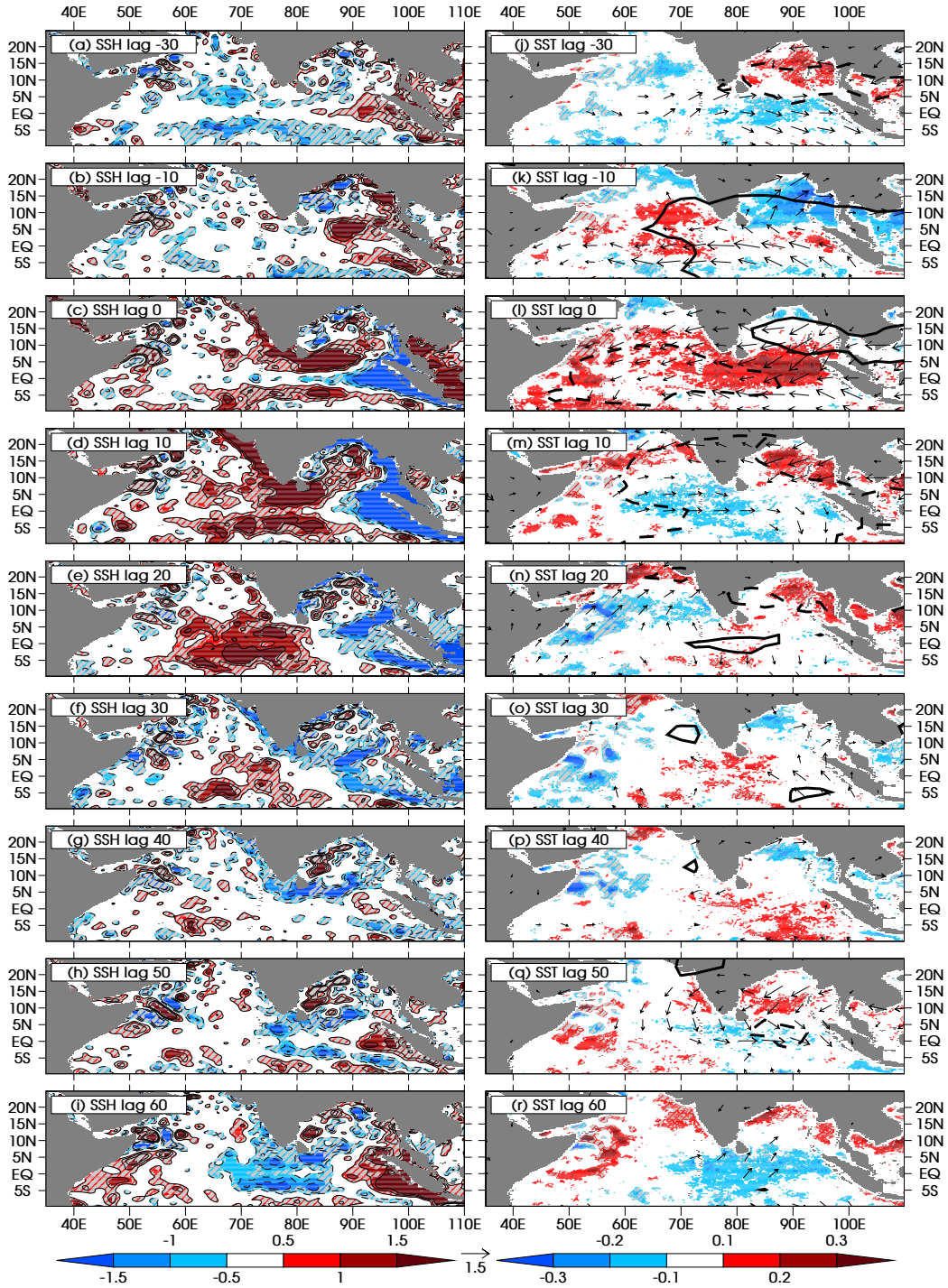

Figure 2.5: Composite anomalies of (a–i) sea surface height (cm) and (j–r) sea surface temperature (°C) at lags -30, -10, 0, 10, 20, 30, 40, 50 and 60 days relative to phase 1 of the MJO. Surface winds are plotted where either the u- or v-component is significant at the 95% confidence level; a scale vector of 1.5 m s^{-1} is shown. For panels (a–i), the contour and shading interval is 0.5 cm. For panels (j–r) the shading interval is 0.1 °C. OLR is plotted as thick contours at $\pm$7.5 W m^{-2} in panels (j–r); the negative contour is dashed. Regions where the anomalies are not significant at the 95% level are hatched over such that only significant anomalies are clearly visible. The SSH composites at lags 0, 10, 20, 30 and 60 and the SST composites at lags -30, -10, 0, 10, 20, 40 and 60 pass the field significance test at the 95% confidence level

the shortwave and latent heat fluxes (Woolnough *et al.*, 2000), so it is possible to make qualitative estimates of the strength of the total flux from the strength of the OLR and wind anomalies. The wind anomalies are generally stronger in the eastern Indian Ocean, and decrease in magnitude and significance with time, becoming largely insignificant by lag 60. The OLR anomalies are strong at lags 0 and 10 but rapidly decrease in magnitude later, with few anomalies exceeding the contour value of ± 7.5 W m^{-2}. By lag 60, the relationship between SST and SSH becomes stronger and more coherent, with positive anomalies around 50–60°E, and a broad region of negative anomalies between 70 and 100°E. The arrival of the Rossby waves and the associated warm SST anomalies near 60°E may help to trigger convection over the Indian Ocean 60 days after it was previously active in phase 1.

To investigate this hypothesised relationship, we construct lagged Hovmöller diagrams of SSH, SST and total accumulated surface heat flux for the Indian Ocean. The maximum amplitude SSH anomalies associated with first meridional mode equatorial Rossby waves occur off the equator between 2–5°N and S (Chelton *et al.*, 2003). Since this is consistent with the waves seen in the composites, we create the SSH Hovmöller diagrams by averaging over these latitude ranges to isolate the Rossby wave response. This method produces similar results to averaging over each latitude band separately, implying that the Rossby waves present in the lagged composites have a symmetric, meridional mode 1 structure with dual maxima, as opposed to higher meridional modes which are either anti-symmetric or have a more complex structure (Chelton *et al.*, 2003).

Because both the MJO activity and the mean circulation in the Indian Ocean undergo a strong seasonal cycle, the summer and winter monsoon seasons were analysed separately. This allows the effects of the equatorial currents on the Rossby wave phase speed to be investigated further and allows the impact of such variation on the atmosphere-ocean feedbacks to be examined.

2.6.4.2 Northern Winter

Figure 2.6 shows the Hovmöller diagrams of SSH and SST for all MJO events occurring between November and April (the northeast monsoon). Both the upwelling and downwelling Rossby waves can clearly be seen on the left hand panel. The downwelling

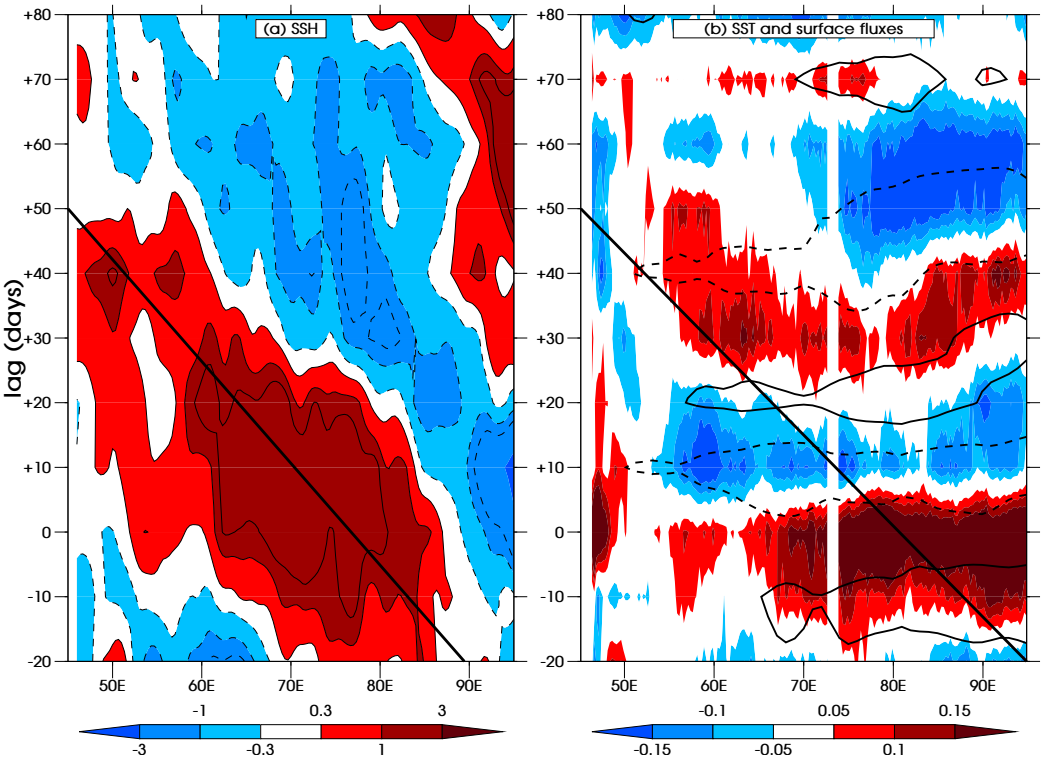

Figure 2.6: Hovmöller diagram of (a) composite SSH anomalies and (b) composite SST anomalies for lags -20 to 80 relative to phase 1 of the MJO, averaged between 2–4°N and 2–4°S for November–April. The shading interval is as shown in the legends in cm, and °C, respectively. In (b), the total surface heat flux is contoured at 12 Wm^{-2}, the negative contour is dashed, and the zero contour is omitted. The solid diagonal lines are fitted by eye to the SSH anomalies to represent the propagation of the downwelling Rossby wave in (a).

Rossby wave, forced by Kelvin waves generated in the previous MJ event, propagates from around 85°E at lag -20 to 50°E around lag 45, in time for the next MJ event. This implies a phase speed of roughly 0.8 m s^{-1}, shown by the solid line in Figure 2.6.

The right hand panel shows the SST Hovmöller diagram, which displays little in the way of propagation. The SST anomalies tend to follow the surface fluxes with the canonical quarter-cycle lag (Shinoda *et al.*, 1998, as discussed in Section 2.3). However, it is likely that the propagation of the downwelling Rossby wave (shown by the diagonal line in Figure 2.6) will also warm the SSTs slightly such that the warm (cool) anomalies are amplified (reduced), but that this is largely masked by the flux-induced SSTs. In addition, the thermocline is deeper in the central and eastern Indian Ocean (Figure 2.7) such that the effect of upwelling on SSTs will be reduced.

A key result of this study is that the arrival of the downwelling Rossby wave in the western Indian Ocean leads to a local warming of the SST with the potential to trigger a new MJ event. In Figure 2.6, there is an extended region of anomalously warm SSTs at

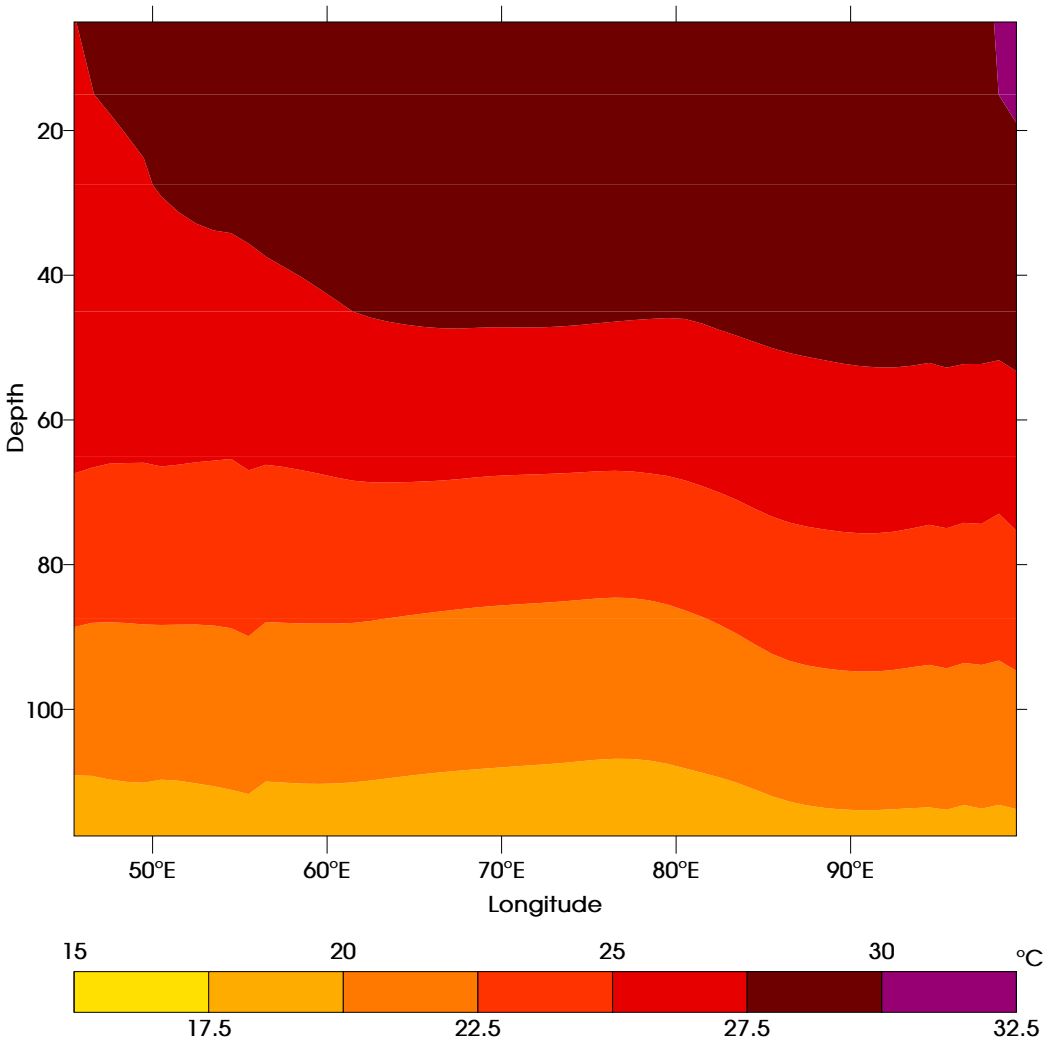

Figure 2.7: Mean subsurface temperature (shaded in °C; see legend) from the ECCO ocean state estimate over the period 1992-2007 and the latitude range 6°S–6°N, showing the shoaling thermocline in the western Indian Ocean.

55–60°E between lags 40 and 50, occurring shortly after the Rossby wave has propagated through this region. These warm SSTs cannot be attributed to surface fluxes since the total fluxes are negative for ∼12 days prior to the SST maximum, thus they are most likely generated by the Rossby wave. The western Indian Ocean is known to be a region in which there is a relatively high correspondence between thermocline depth and SST; Xie *et al.* (2002) show that the maximum correlation occurs in a region between 3–10°S and 50–80°E.

These SST anomalies near 60°E at lag 50 are at least as strong and more coherent than those in the same location at lag 0, and roughly equivalent to the thermodynamic response to the MJO (Shinoda *et al.*, 1998). Note that the relative modesty of these SST anomalies is partly due to the compositing methodology, which, by averaging over a large number of

events, will tend to reduce the magnitude of any individual anomalies. Intraseasonal SST anomalies of this magnitude have been shown to force MJO convection in atmosphere-only models (Fu and Wang, 2004; Matthews, 2004b), and, if SSTs in the western Indian Ocean are important for initiating the MJO convection then that the dynamically-induced SST anomalies at lag 50 could be sufficient to generate a new MJ event. However, the anomalies further east around lag 35 are more zonally coherent and will also contribute to the generation of the next MJ cycle. It should be stressed that the initiation of a new MJ event by the Rossby wave-induced SSTs is one of many possible generation mechanisms which may all influence the behaviour of the MJO. Nevertheless, this proposed mechanism will contribute to the broadband nature of the MJO by enhancing the longer time scale variability. To investigate the response of the MJO to these dynamically-forced

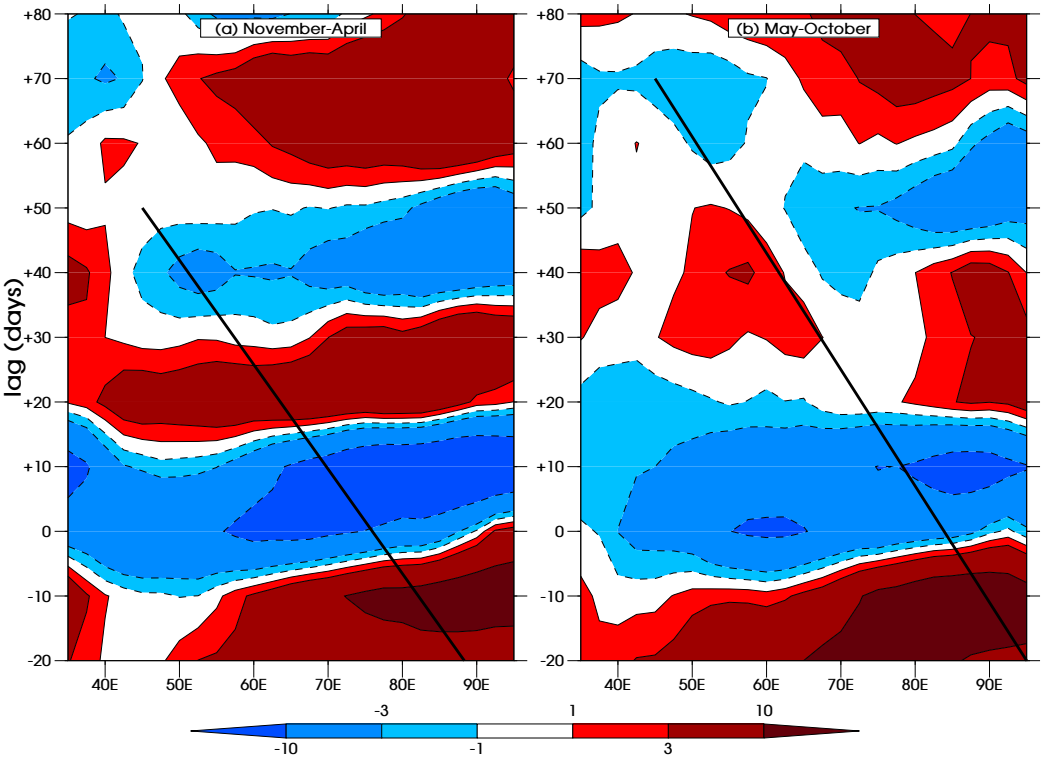

Figure 2.8: Hovmöller diagram of OLR anomalies for lags -20 to 80 relative to phase 1 of the MJO, for (a) November–April and (b) May–October. The contour and shading interval is shown in the legend (in W m^{-2}). The solid diagonal lines are fitted by eye to the SSH anomalies to represent the propagation of the downwelling Rossby waves in (a) November-April and (b) May–October.

SST anomalies, Hovmöller diagrams of OLR anomalies have been constructed for the same period. Because the MJO-induced OLR anomalies are meridionally extensive, the anomalies are averaged over a latitude range of 8°S–8°N such that the OLR anomalies accurately represent MJO activity. Constructing the Hovmöller diagrams over the same

latitude bands as for the SSTs does not alter the relationship between OLR and SST substantially for either summer or winter, but merely results in a stronger agreement between the two fields (not shown). Figure 2.8(a) shows the OLR composite for November–April. The MJO is strongly cyclical across the basin, with a period of around 40 days. The eastward-propagating anomalies of the MJO originate around 40–50°E at lag 0, but originate further east at lag 50, when the MJO is initiated at the same longitude as the dynamically induced SST anomalies.

From the data available it is hard to determine the relative importance of this dynamical mechanism compared with other mechanisms for generating subsequent MJO events, especially during the winter monsoon season when the various mechanisms coincide. The feedback from the dynamical waves onto the MJO is likely to be a source of resonant amplification in this season. The importance of the mechanism can be partly tested by comparison of the behaviour of the MJO in different seasons.

2.6.4.3 Northern Summer

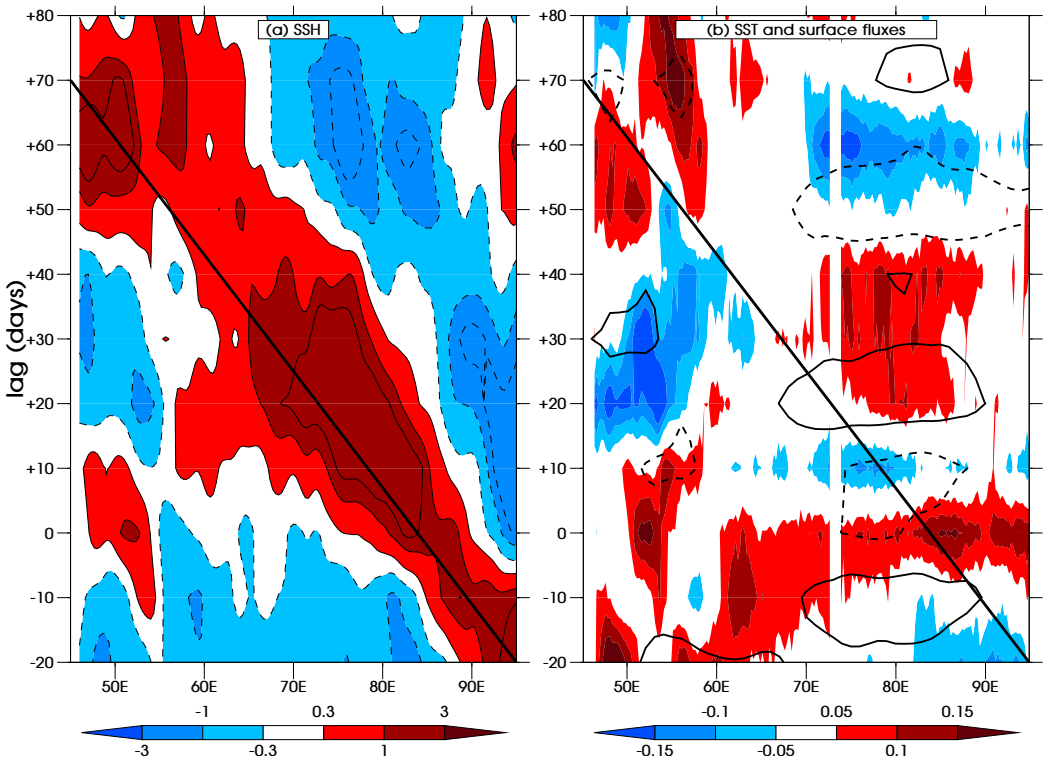

Figure 2.9: As Figure 2.6 but for May–October.

Figure 2.9 shows the Hovmöller diagram of SST and SSH for the southwest monsoon period between May and October. The propagation speed for the Rossby wave is

somewhat slower; the positive SSH anomalies do not reach the western Indian Ocean until lag 70 implying a phase speed of 0.7 m s^{-1}. In comparison, the theoretical first internal mode Rossby wave speed for non-dispersive Rossby waves in the Indian Ocean is 0.9 m s^{-1} (Chelton *et al.*, 2003; Fu, 2007). However, as noted in the introduction, for Rossby wavelengths of the order of 20–30° longitude there is an error of ∼15% relative to the non-dispersive approximation, reducing the phase speed to 0.68–0.77 m s^{-1}. Another possible reason for the discrepancy is the meridional potential vorticity (PV) gradient, which Chelton *et al.* (2003) showed reduced the phase speed of non-dispersive equatorial Rossby waves in the Pacific by ∼0.2 m s^{-1}.

In addition, the equatorial currents in the Indian Ocean exhibit a strong seasonal cycle which is likely to have an effect on the phase speed of the equatorial Rossby waves. In northern summer, there is a broad, eastward mean current with velocities of the order of 0.2–0.3 m s^{-1}, which will reduce the Rossby wave phase speed. In northern winter the current structure is more complex with a westward North Equatorial Current of 0.3 m s^{-1} in the eastern Indian Ocean and 0.5–0.8 m s^{-1} in the western region, and an eastwards Equatorial Countercurrent of 0.5–0.8 m s^{-1} (Tomczak and Godfrey, 1994). The total mean current between roughly 5°N and 5°S is therefore considerably less in northern winter, becoming negligible in January. Doppler shifting by the mean currents is thus consistent with the slower Rossby wave phase speed in summer. However, the relatively narrow meridional width of equatorial currents means that the change in the Rossby wave phase speed is often considerably less than the magnitude of the current velocities (McPhaden and Ripa, 1990). Quantifying this and the effect of changes to the stratification and the meridional PV gradients requires further research and is beyond the scope of this study.

Consistent with the hypothesis that the Rossby waves generate warm SSTs upon reaching the western Indian Ocean, the timing of the SST anomalies around 55°E is closely related to the SSH anomalies. There is a similar time lag between the Rossby wave propagation and the SST anomalies as seen for the winter monsoon. Further east, the SST variability appears more closely related to the surface fluxes, although modulation by the Rossby wave is also apparent.

During northern summer, warm SST anomalies of over 0.15 °C are present around

55°E between lags 50 and 80, comparable in magnitude to those present at zero lag, and equal to the overall magnitude of SST variation in response to the MJO in the Indian Ocean (Shinoda *et al.*, 1998). These SSTs do not have a coherent phase relationship with the local surface fluxes, in contrast to the SST anomalies in the central Indian Ocean which exhibit the canonical quarter-cycle lag described in Section 2.3. Thus, the dynamically forced SSTs of the western Indian Ocean would act to enhance MJO variability at periods of 60–70 days, or shift the initiation region further eastwards. We note that the eastward-propagating MJO is generally less coherent during boreal summer, and speculate that this delaying mechanism may be (at least partly) the cause.

The OLR composite for the summer monsoon (May–October, Figure 2.8(b)) is strikingly different from that for the winter monsoon. The period of the MJ events is longer, consistent with the longer transit times for the Rossby waves. Although the second composite MJ event occurs before the arrival of the Rossby waves in the western Indian Ocean, it originates further east, around 70°E, closely following the arrival of the Rossby wave at this longitude. In addition, there is evidence of westward-propagating OLR anomalies overlying the Rossby waves from lags 50–70, indicating an interaction between the two processes. There is also potential for the arrival of the Rossby waves in the western Indian Ocean to trigger MJ events around lag 70, which would enhance the low-frequency component of the MJO, although the Hovmöller diagram (Figure 2.8(b)) suggests that this is less common.

2.7 Conclusions

This study has shown the magnitude of the global dynamical response to the MJO, which includes significant anomalies in all tropical ocean basins and remote responses in the extratropics. That these remotely forced responses are significant is indicative of the sensitivity of the ocean to the MJO; in addition, the locally forced anomalies are long lived and temporally coherent, remaining significant out to lags of 60 days in the Indian Ocean.

In addition, this paper has highlighted the role of the ocean dynamics as a component of the coupled MJO system within the Indian Ocean, where a strong response is evident in the ocean dynamics which subsequently leads to SST anomalies with the potential to

feed back to the atmosphere. This relationship between the ocean dynamics and SST is similar to that found by Shinoda and Han (2005), who showed that sub-monthly variability enhanced by the IOD forces equatorial Kelvin waves which feedback onto the atmosphere through anomalous downwelling and thus warmer SSTs along the coast of Sumatra. The magnitude of the SST anomalies found here is equivalent to those forced by the surface fluxes of the MJO (Shinoda *et al.*, 1998), which have been shown to force atmospheric convection similar to the MJO in atmospheric models (Fu and Wang, 2004; Matthews, 2004b).

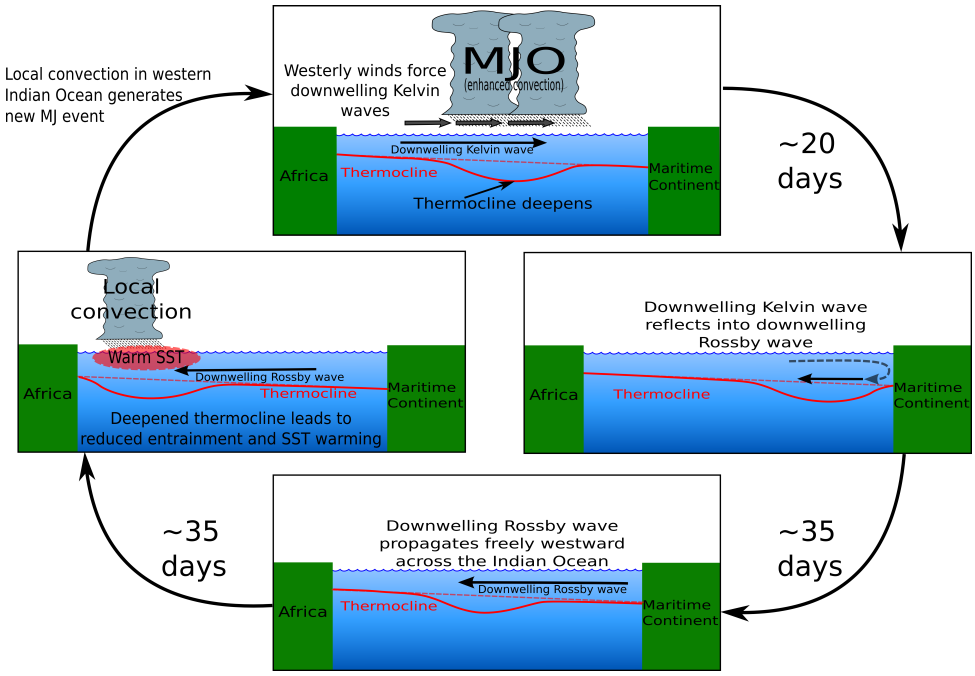

Figure 2.10: Schematic of MJO dynamical ocean feedback mechanism

The key components of this proposed feedback mechanism are summarised in Figure 2.10. The westerly surface wind anomalies associated with phases 3–4 of the MJO generate a downwelling equatorial Kelvin wave. This subsequently reflects into a downwelling equatorial Rossby wave which propagates westwards and arrives in the western Indian Ocean around 90 days after the initial Kelvin wave was forced, although this time scale will vary with season due to the different Rossby wave propagation speeds.

The timing of the Rossby wave arrival in the western Indian Ocean will, when the MJO is periodic with a time scale of 48 days, approximately coincide with the next-but-one MJ event. Alternatively, there may be no intervening event, in which case this

mechanism is a potential trigger for primary MJ events (Matthews, 2008). In either case, this mechanism will amplify the low-frequency component of the MJO, and may also modulate its seasonality. The mechanism is reminiscent of the delayed oscillator theory of ENSO (Battisti, 1988), although the time scale is very different, partly due to the much smaller ocean basin.

Despite the importance of the flux-driven SST anomalies in the central and eastern Indian Ocean, the SST anomalies in the western Indian Ocean are of equal magnitude but are clearly driven by the Rossby waves. This is highlighted by the difference in the SST fields between the summer and winter monsoons. This variation can be explained by the difference in the Rossby wave propagation speed which is consistent with the seasonal cycle in equatorial currents, suggesting that Doppler shifting is of first-order importance. The SST anomalies cannot be explained by local surface fluxes, since the two fields are almost exactly out of phase. Indeed, it appears that the surface flux variations in this region are primarily driven by shortwave flux variations (implied by the OLR anomalies) in *response* to the SSTs. Note that these convective anomalies in the western Indian Ocean will be important for the local and East African climate whether or not they generate a new MJ event.

The response of the MJO to the dynamic ocean forcing is complicated by the other mechanisms which sustain the MJO; for example, the composite Hovmöller diagrams (Figures 2.6, 2.8 and 2.9) indicate that the new MJ event is most likely to occur when both the dynamic (Rossby wave) and thermodynamic (surface heat flux) SST forcings are positive. In the winter monsoon (November–April), these two factors combine at around lag 40 to create a strongly cyclical MJO which is initiated in the western Indian Ocean. In contrast, for the summer monsoon composites, these two factors are in phase in the central Indian Ocean, from where the convective anomalies originate. The arrival of the Rossby waves in the western Indian Ocean does appear to generate convection in summer, but this is out of phase with the other forcing mechanisms such that this mechanism will reduce the coherence but increase the broadband nature of the summer MJO.

Our results imply that to accurately model the MJO, the ocean dynamics may need to be simulated adequately enough to resolve the Kelvin and Rossby waves as well as the SST anomalies forced by these waves. Achieving this may resolve some of the current

difficulties with modelling the MJO (Inness and Slingo, 2003). The significance of the dynamical response has implications for the circulation, chemistry and biology of the tropical oceans. Further work is necessary to investigate such matters, in addition to determining the strength of the feedback onto the MJO. It is hoped that this chapter has highlighted the importance of these questions, the answers to which may help improve our understanding of the coupled MJO system.

2.8 Acknowledgements

The merged TOPEX/Poseidon–ERS-1 satellite altimetry data were provided by AVISO and are available on their website at http://www.aviso.oceanobs.com/. The TMI SST data were obtained from the SSM/I website at http://www.ssmi.com/tmi/. The ECMWF winds and surface flux data were obtained through the British Atmospheric Data Centre (BADC) and from the ECMWF website at http://data-portal.ecmwf.int/data/d/interim_daily/. The interpolated OLR data were obtained from the NOAA/OAR/ESRL PSD web site at http://www.cdc.noaa.gov/. The Wheeler-Hendon index was obtained from http://www.bom.gov.au/.

Chapter 3

Ocean Rossby waves trigger primary Madden-Julian events

3.1 Preface

This chapter consists of a paper published in the Quarterly Journal of the Royal Meteorological Society, in March 2012, with the title "Ocean Rossby waves as a triggering mechanism for primary Madden-Julian events" (Webber *et al.*, 2012a). The manuscript is largely unchanged from the published paper apart from minor superficial changes to the figures and minor changes to the text, and all references to Webber *et al.* (2010) have been changed to "Chapter 2". BGMW was responsible for the majority of the work, under supervision by AJM, KJH and DPS who provided scientific input and helped revise the text for publication. The comments of Matthew Wheeler and an anonymous reviewer also helped to improve the manuscript.

3.2 Abstract

The Madden-Julian Oscillation (MJO) is sporadic, with episodes of cyclical activity interspersed with inactive periods. However, it remains unclear what may trigger a Madden-Julian (MJ) event which is not immediately preceded by any MJO activity: a "primary" MJ event. A combination of case studies and composite analysis is used to examine the extent to which the triggering of primary MJ events might occur in response to ocean dynamics. The case studies show that such events can be triggered by the arrival of a

downwelling oceanic equatorial Rossby wave, which is shown to be associated with a deepening of the mixed layer and positive sea surface temperature (SST) anomalies of the order of 0.5–1°C. These SST anomalies are not attributable to forcing by surface fluxes which are weak for the case studies analysed. Furthermore, composite analysis suggests that such forcing is consistently important for triggering primary events. The relationship is much weaker for successive events, due to the many other triggering mechanisms which operate more strongly during periods of cyclical MJO activity. This oceanic feedback mechanism is a viable explanation for the sporadic and broadband nature of the MJO. Additionally, it provides hope for forecasting MJ events during periods of inactivity, when MJO forecasts generally exhibit low skill.

3.3 Introduction

Equatorial Rossby and Kelvin waves form a large part of tropical ocean variability at timescales ranging from intraseasonal (Kessler *et al.*, 1995; Hendon *et al.*, 1998) to interannual (Battisti, 1988; McPhaden, 1999). Such waves affect sea surface height (SSH), zonal currents, pycnocline depth and vertical velocities. Anomalies in mixed layer depth, along with vertical, meridional and zonal advection, lead to variability in heat content and sea surface temperatures (SSTs; McCreary, 1983; Battisti, 1988). These effects on SSTs allow the ocean dynamics to trigger atmospheric convection, leading to feedbacks which have been shown to be important for the El Niño-Southern Oscillation (ENSO; Battisti, 1988; Kessler and McPhaden, 1995; McPhaden, 1999) as well as for the Madden-Julian Oscillation (MJO; Chapter 2, Han *et al.*, 2001).

Baroclinic waves perturb the depth of the mixed layer by several orders of magnitude more than they affect SSH. Thus, although typical SSH anomalies associated with equatorial Kelvin and Rossby waves are of order 10 cm (Giese and Harrison, 1990), thermocline depth can vary by as much as 40 m (Kessler *et al.*, 1995; McPhaden, 1999). This depth anomaly is of the opposite sign to the SSH perturbation, such that waves with a positive SSH signal correspond to a deeper mixed layer. It is common to describe baroclinic waves associated with positive SSH anomalies and a deeper mixed layer as "downwelling" waves. We adopt this terminology here, although it should be noted that such a wave is associated with both downwelling (at the leading edge) and upwelling (at the

trailing edge) anomalies. Similarly, baroclinic waves with negative SSH anomalies and a shallower mixed layer depth are termed "upwelling" waves.

Equatorial waves are forced by anomalies in surface wind stress. A symmetric westerly wind burst along the equator will generate Ekman convergence at the equator and thus force downwelling anomalies which then propagate eastward as a Kelvin wave (Battisti, 1988; Giese and Harrison, 1990). Typically, such wind bursts will also force a westward-propagating Rossby wave of the opposite sign, although this is dependent on the meridional structure of the wind field and its resultant curl (Chelton *et al.*, 2003). The meridional component of the wind field can also affect the magnitude of the resultant Rossby waves.

The MJO is the dominant mode of tropical atmospheric variability at intraseasonal timescales, and is thus an important source for intraseasonal oceanic Rossby and Kelvin wave activity. The MJO is characterised by propagating atmospheric wave structures affecting convection, surface and upper-tropospheric winds, and surface fluxes, and influencing rainfall throughout the tropics and worldwide (Madden and Julian, 1971, 1972; Matthews *et al.*, 2004; Donald *et al.*, 2006). The MJO has a broadband spectral signal, with the most energy in the 40–60 day range (Madden and Julian, 1971, 1972), but with a low frequency tail extending as far as 100 days (Salby and Hendon, 1994). For a full review of the MJO, see Chapter 1, Zhang (2005), and Lau and Waliser (2005).

The MJO has a substantial effect on SSTs through variations in surface fluxes, which has led to the suggestion that coupled ocean-atmosphere processes could be an important component of the MJO. The relative importance of ocean feedbacks as opposed to atmospheric-only mechanisms remains contentious (Zhang, 2005). However, models incorporating atmosphere-ocean coupling tend to outperform atmosphere-only models, although the degree of improvement varies from minimal (Hendon, 2000) to substantial (Inness and Slingo, 2003). Realistic MJO behaviour arises in atmosphere-only models forced by intraseasonal SST anomalies (Woolnough *et al.*, 2001; Fu and Wang, 2004; Matthews, 2004b), reinforcing the notion that there is at least the potential for SST anomalies to exert a strong influence on MJO activity. The standard hypothesis for this thermodynamic feedback is that the SST anomalies are in quadrature with the convective anomalies (Shinoda *et al.*, 1998) such that the positive SST anomalies exist to the east of the enhanced

convection and negative SST anomalies exist to the east of the reduced convection, thus leading to eastward propagation (Flatau *et al.*, 1997; Woolnough *et al.*, 2000). The magnitude of these flux-induced intraseasonal SST anomalies is $\sim$0.15–0.35°C in composites of the MJO (Shinoda *et al.*, 1998). In the Indian Ocean, this ocean-atmosphere interaction is strongest for the low-frequency component of the MJO which is strongest during boreal winter when the convection shifts southward over the Seychelles-Chagos thermocline ridge (Izumo *et al.*, 2010).

In addition to this thermodynamic coupling mechanism, there is also the potential for the ocean dynamics to force the MJO (Chapter 2, Han *et al.*, 2001; Fu, 2007). In the Indian Ocean, the dynamical ocean response to the MJO consists of equatorial Kelvin waves which reflect into equatorial Rossby waves on reaching the coast of Sumatra (Chapter 2, Oliver and Thompson, 2010). These reflected Rossby waves propagate westwards to arrive in the western Indian Ocean approximately 90 days later, where they lead to positive SST anomalies and thus trigger convection within the region where MJO events are initiated (Chapter 2). The magnitude of these composite warm anomalies is similar to the flux-induced anomalies, being around 0.2°C in the absence of strong surface heat fluxes. This dynamical ocean forcing mechanism is one of many triggers for MJO events, but is expected to modulate MJO activity and enhance the low frequency component of the MJO.

This paper seeks to examine whether forcing from ocean Rossby waves can also explain another feature of the MJO, namely the existence of "primary" Madden-Julian (MJ) events (Matthews, 2008). One of the reasons for the broad spectral signal of the MJO is that it is sporadic, with periods of continuous MJO activity punctuated by periods with minimal or incoherent variability. Matthews (2008) defined primary MJ events as having no preceding cycle of the MJO; they may or may not then trigger one or many "successive" MJ events. The key question is then to identify what causes primary events, but no conclusive triggering mechanism has been identified to date. In addition, forecasting the initiation of the MJO after periods of inactivity is notoriously difficult (Jones *et al.*, 2000), possibly due to the lack of understanding of the triggering mechanisms for primary events. However, the feedback from equatorial oceanic Rossby waves has not yet been examined in this light, which we will now address. Section 3.4 describes the data sets used

in this study and Section 3.5 defines the methodologies used. The results are outlined in Section 3.6, starting with the results from primary case studies, and then proceeding to composite studies of both primary and successive events. The conclusions are discussed in Section 3.7.

3.4 Data

The SSH data used in this study are from the merged TOPEX/Poseidon-Earth Remote Sensing (T/P-ERS) satellite altimetry product (Fu *et al.*, 1994; Ducet *et al.*, 2000; Le Traon *et al.*, 2001). Weekly maps on a 0.25° grid were obtained for the period from 14 October 1992 to 23 January 2008, and then interpolated to daily values using cubic splines. This was done to facilitate comparison with other, daily, data sets. SST data from the Tropical Microwave Imaging (TMI) satellite were extracted from 1 January 1998 to 17 December 2008 (Kummerow *et al.*, 2000). The data are available as daily maps of the 3-day average SST at 0.25° resolution. We have chosen the TMI data set over other SST data since it is not obstructed by clouds and thus is more accurate and contains more variance than SST data sets based on infra-red measurements (Harrison and Vecchi, 2001; Klingaman *et al.*, 2008). Comparison with the Reynolds SST data set (Reynolds *et al.*, 2007) suggests that the main conclusions of this work are not dependent on the choice of data set.

In order to analyse sub-surface ocean variability associated with Rossby waves, we use an ocean state estimate derived from the ECCO-GODAE project (Estimating the Circulation and Climate of the Ocean-Global Ocean Data Assimilation Experiment; Wunsch and Heimbach, 2007). This is based on the Massachusetts Institute of Technology (MIT) general circulation model (Marshall *et al.*, 1997a; Marshall *et al.*, 1997b) and its adjoint (Heimbach *et al.*, 2005). It assimilates all available observations to provide the best estimate of ocean state while retaining dynamical consistency both internally and with atmospheric forcing (Wunsch and Heimbach, 2007). The model covers the world ocean between 80°N and 80°S, excluding the Arctic, at 1° horizontal resolution with 23 vertical levels. The ECCO data used in this study are the vertical velocities and density anomalies, along with SST data for comparison with the TMI data set, all obtained at daily resolution for the period from 2 January 1992 to 30 December 2007.

Outgoing long-wave radiation (OLR) is used as a proxy for tropical deep convective precipitation. The OLR data for this study were obtained as 2.5° resolution gridded daily maps from the optimally-interpolated Liebmann and Smith (1996) data set from 1 January 1990 to 31 October 2008. For comparison with the OLR data, precipitation from the Tropical Rainfall Measuring Mission (TRMM) data set was obtained for the period from 1 January 1998 to 31 May 2010. The main results of this paper are not sensitive to whether OLR or TRMM data are used; the OLR data set is preferred for this study as it covers the entire period for which SSH data are available. Surface fluxes of latent and sensible heat, and short- and long-wave radiation were obtained from the European Centre for Medium-range Weather Forecasts (ECMWF) ERA-Interim data set (Dee *et al.*, 2011) for the period of 1 January 1990 to 31 December 2008; net surface heat fluxes were then calculated from these separate components.

The linear trend, mean and first three harmonics of the annual cycle were removed point-wise from each data set to produce detrended anomaly fields, which were then bandpass-filtered using a 20-200 day Lanczos filter. The use of such a broadband filter is motivated by its ability to exclude low-frequency climate signals as well as high-frequency noise while better retaining the MJO signal and the distinction between individual MJ events than a narrower filter window (Matthews, 2000). The filter uses 241 symmetric weights, meaning that 120 days of data are lost at each end of the data set. All data sets were further truncated so that an integer number of calendar years are retained, thus avoiding seasonal bias.

3.5 Methodology

Although it has become common to use the multivariate Wheeler-Hendon index (Wheeler and Hendon, 2004) to define the MJO, Matthews (2008) used a uni-variate definition of the MJO based solely on its convective signal. The motivation for this approach was to better isolate causes for the triggering of convection in primary MJ events and also to maximise the degree of independence in other atmospheric variables. We choose to use the same definition of the MJO and primary and successive MJ events as Matthews (2008), such that the results can be compared with that study. However, using the Wheeler-Hendon index produces broadly similar results.

Table 3.1: Start dates for primary and successive events for the period 1992–Present.

Year	Primary Events	Successive Events
1992	2 Dec	6 Feb, 28 Mar, 30 Apr
1993	30 Nov	15 Jan, 12 Feb, 28 May, 21 Jul
1994		15 Mar, 31 May, 29 Jun, 17 Nov
1995		8 Jan, 24 Feb, 27 Mar, 4 May, 6 Jun
1996		26 Mar, 26 Apr, 8 Jun, 5 Jul, 10 Oct, 7 Dec
1997	12 Feb	31 Mar, 10 May
1998	29 Oct	
1999	22 Aug	20 Jan, 17 Mar, 11 Oct, 2 Dec
2000	20 Feb	2 Aug, 18 Nov
2001	26 Apr	29 Jul
2002		1 May, 1 Aug, 1 Oct, 12 Nov, 22 Dec
2003	7 Dec	4 May, 2 Oct
2004	24 Sep	27 Dec
2005	30 Mar	29 Aug, 11 Oct
2006	21 Mar	10 Jan, 18 Apr, 9 Sep, 23 Dec
2007	29 Apr, 20 Jul	12 Dec
2008	26 Aug	18 Mar, 18 Apr
2009		27 Jan, 9 Apr, 9 Nov

The methodology of Matthews (2008) defines four phases of the MJO, with phase A representing the initiation of convection in the Indian Ocean coinciding with reduced convection in the western Pacific and phase B the propagation of enhanced convection over the Maritime Continent. Phases C and D are the inverse of phases A and B respectively. Periods of low MJO activity were classified as phase N, with a buffer zone to prevent a weak MJO from oscillating between active and inactive such that it is erroneously labelled a primary event (Matthews, 2008).

Primary events are thus defined using the above terminology by the phase sequence NABCD, and successive events by DABCD. Whether either type of event is followed by another MJO event is not considered in this study, although understanding MJO events which are not followed by another ("terminal events") is a worthwhile avenue of future study. A list of the start dates of primary and successive events is provided in table 3.1. Note that the dates for each event correspond to the maximum principal component (PC) amplitude in phase A, which refers to convection within the Indian Ocean. Matthews (2008) showed that this is the most common region for primary MJ events to occur, but it is possible for primary events to be triggered elsewhere. It is therefore not necessary for a successive event to be preceded by a primary event as defined here; furthermore, it is also possible for successive events to follow a period of disjointed MJO activity that is neither

"successive" nor "primary".

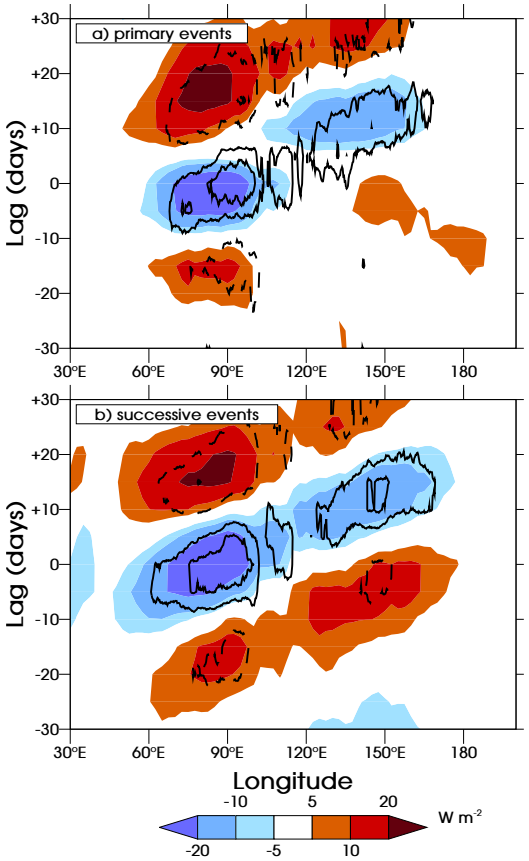

Figure 3.1: Hovmöller diagrams of anomalous OLR (shaded; W m^{-2}) and TRMM precipitation (contours) from lagged composites for a) primary and b) successive MJ events. The TRMM contour interval is 0.1 mm hr^{-1}, the zero contour is omitted and negative contours are dashed.

Figure 3.1 shows composite Hovmöller diagrams of OLR anomalies over the warm pool of the western Pacific and the Indian Ocean for the dates defined in table 3.1. Although there are some positive OLR anomalies in the Indian Ocean prior to the initiation of primary events, these do not propagate or form part of a coherent MJ event. By contrast, for successive events, the preceding positive OLR anomalies propagate coherently across the entire warm pool. These results are consistent with those of Matthews (2008).

Figure 3.2 shows the propagation of Rossby and Kelvin waves in a composite of SSH at lag -35 days relative to primary MJ events. The dashed arrow along the equator shows the equatorial Kelvin waveguide, the black boxes and arrows the equatorial Rossby waveguide. These boxes are defined on the basis of the Rossby radius of deformation; first meridional mode Rossby waves typically have SSH maxima centred around 4° latitude away from the equator (Chelton *et al.*, 2003). The positive SSH anomalies in the central Indian Ocean are associated with a downwelling Rossby wave, while the negative SSH

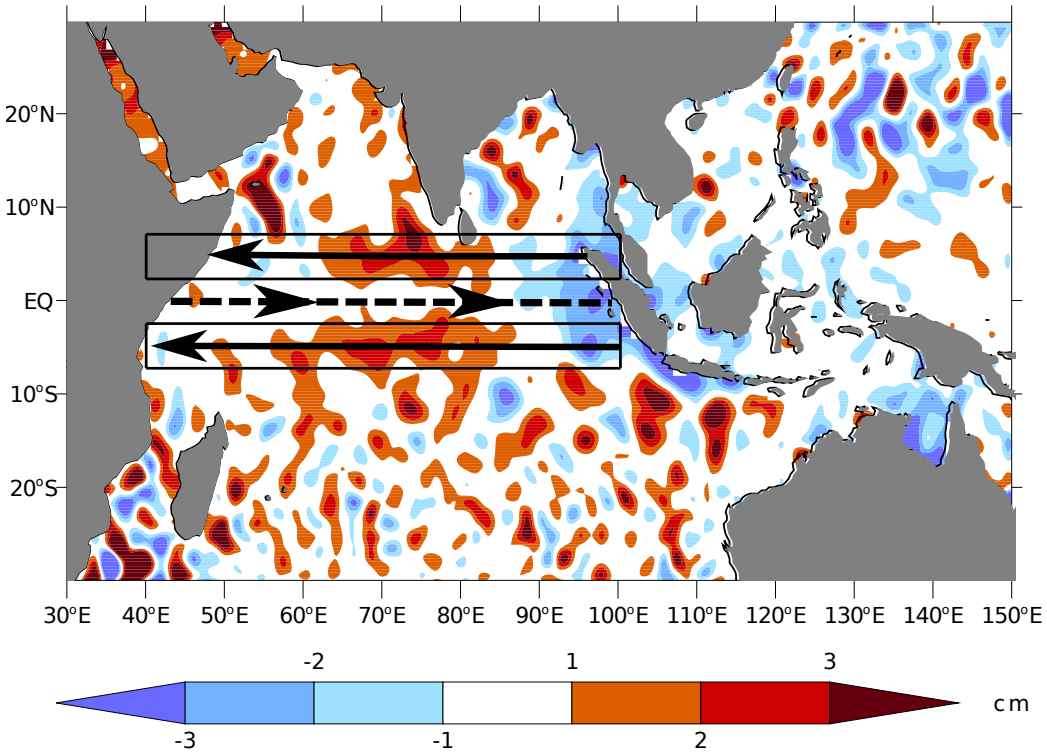

Figure 3.2: Composite SSH anomalies at lag −35 days relative to primary MJ events as defined in table 3.1, illustrating the propagation paths for equatorial Rossby waves (black boxes and solid arrows), and equatorial Kelvin waves (dashed arrow). The black boxes also represent the latitudes over which subsequent Hovmöller diagrams of Rossby wave propagation are calculated.

anomalies near the Maritime Continent indicate the reflection of an upwelling equatorial Kelvin wave into an upwelling equatorial Rossby wave. The triggering of upwelling coastal Kelvin waves can also be seen at the eastern boundary. For the subsequent analysis of the effects of Rossby wave propagation, Hovmöller diagrams for the Rossby waveguide are constructed over the latitudes and longitudes indicated by the black boxes in Figure 3.2. Data over land are masked and therefore not included in the results.

For the case study analysis, two representative primary events are selected, starting on 12 February 1997 and 24 September 2004. Relevant atmospheric and oceanic variables are extracted for the period extending from 100 days prior to the start date of these primary events to 100 days after. This allows the propagation of any Rossby waves to be followed across the Indian Ocean. The same time window is used for the compositing method, such that the composites represent the average of each variable over all the primary event case studies. Composites are also produced for the successive events.

3.6 Results

3.6.1 Case studies

Figure 3.3 shows two case studies of primary MJ events. The left hand panels relate to the event starting 24 September 2004, the right hand panels are for the event starting 12 February 1997. In both events, a downwelling equatorial Rossby wave (positive SSH anomalies) propagates westward between -100 and 0 days; this is indicated by the solid diagonal line in Figure 3.3(a,d), which is calculated using the methodology described in the appendix. This is then followed by the initiation of the MJO convection, around 0 days, shown by the eastward-propagating negative OLR anomaly in the same panels. Note that although the OLR anomaly appears to be zonally uniform due to the aspect ratio, it is in fact propagating east at around 5 m s^{-1}, consistent with previous observations of the MJO (Zhang, 2005).

A key result of this paper is that in both of these case studies, the initiation of the primary MJ events coincides with the arrival of the downwelling Rossby waves in both space and time. This is consistent with the mechanism proposed in Chapter 2. However, it is likely that such oceanic forcing will be most important, and most apparent in observations, when other triggering mechanisms are weak or non-existent, such as is the case for primary events (Matthews, 2008).

In order for the ocean dynamics to trigger an MJ event, the downwelling waves must create positive SST anomalies of relatively large magnitude; i.e., similar magnitude to those observed in response to surface fluxes. To study this we use a combination of TMI SST where available (for the 24 September 2004 case study) and ECCO SST elsewhere (for the 12 February 1997 case study), along with vertical velocity and density data from ECCO. In both case studies the positive SSH anomalies are led by downwelling anomalies and coincide with negative density anomalies at 75 m (Figure 3.3(c,f)), consistent with a deepening of the mixed layer. This will increase the heat content of the mixed layer and lead to a reduction in the entrainment of cold subsurface waters through wind mixing (McCreary, 1983; Battisti, 1988). These effects lead to an increase in SST, as observed in the positive SST anomalies along the Rossby wave propagation path (Figure 3.3(b,e)).

Given that the initial triggering of convection for MJ events tends to be in the western Indian Ocean (e.g., Zhang, 2005), it is the region to the west of 75°E that is primarily

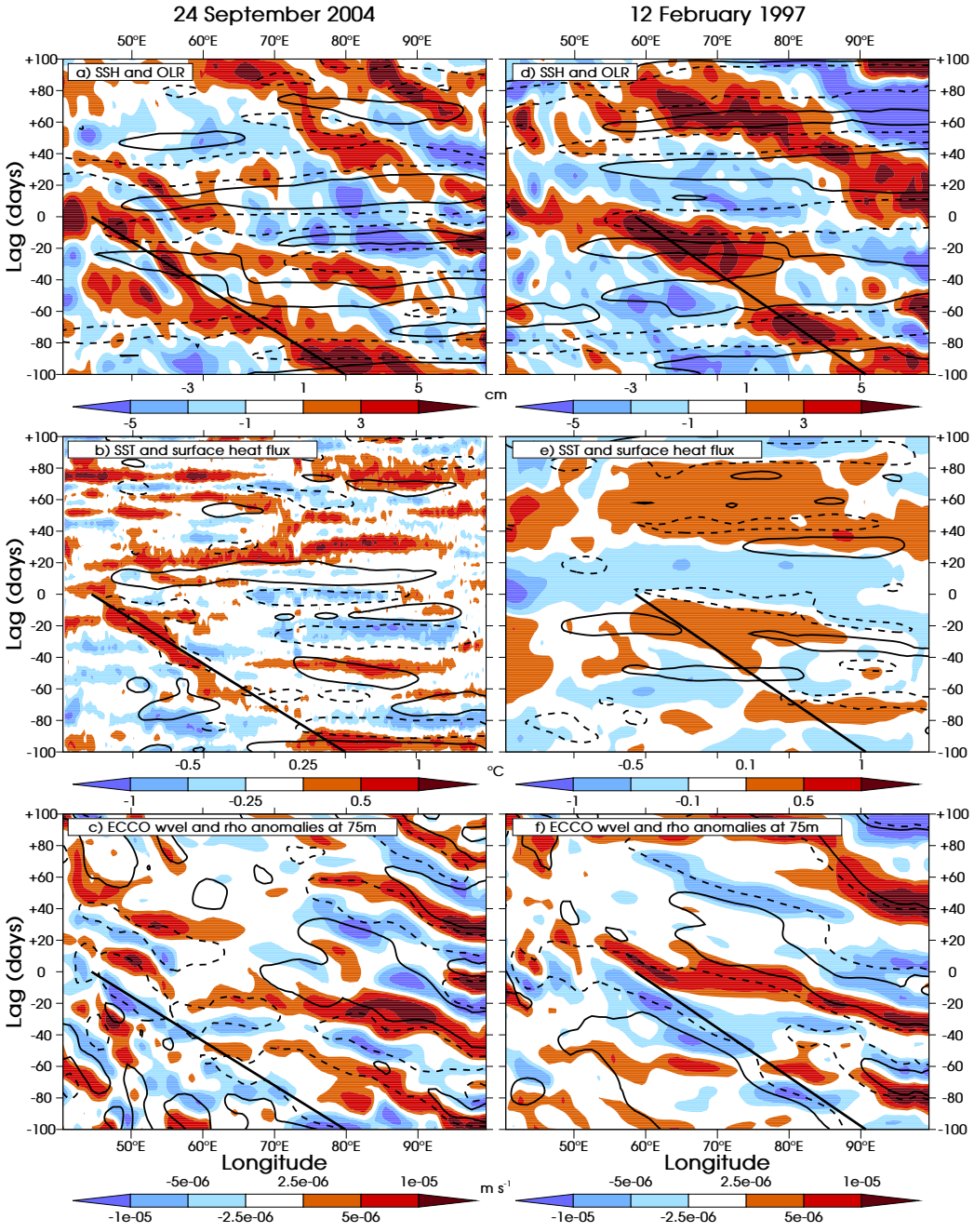

Figure 3.3: Hovmöller diagrams at lags −100 to +100 days relative to the primary event starting on 24 September 2004 of anomalous: (a) SSH (shaded; see legend) and OLR (contour interval is 15 W m^{-2}), (b) SST (shaded; see legend) and surface flux (contour interval is 30 W m^{-2}), (c) ECCO vertical velocity (shaded; see legend) and density (contour interval is 0.1 kg m^{-3}) at 75 m depth. (d) to (f): as (a) to (c) but for the primary event starting on 12 February 1997. Negative contours are dashed and the zero contour is omitted. The anomalies are averaged from 2–6°S and 2–6°N, over the equatorial Rossby wave boxes shown in Figure 3.2. The solid diagonal line in each panel represents the propagation of the downwelling Rossby wave (positive SSH anomalies) in panels (a) and (d).

of interest for oceanic triggering of primary events. Note that in the classical model of thermodynamical air-sea interaction within the MJO (Flatau *et al.*, 1997; Shinoda *et al.*, 1998), SST anomalies would be expected to be in quadrature with the heat flux anomalies. There is some evidence of this in the eastern Indian Ocean (east of 70°E in Figure 3.3(b,e)), where there are zonally extensive flux anomalies that generally precede SST anomalies of the same sign. However, there are some SST anomalies that are not well explained by the surface fluxes, especially in the western Indian Ocean. For the case study of 24 September 2004, the SST anomalies between lag -50 and lag 0, 40–60°E (Figure 3.3(b)) are consistent with the location and propagation of the downwelling anomalies (Figure 3.3(c)). In addition, these SSTs are not consistent with the surface flux anomalies, which are negative and appear to arise in *response* to the warm SSTs. The magnitude of the SST anomalies within this region of interest is around 0.5–1°C, which is substantial for intraseasonal SST anomalies, and certainly sufficient to generate MJO-like convection (Woolnough *et al.*, 2001; Fu and Wang, 2004; Matthews, 2004b). In addition, the coherent propagation of these SST anomalies from lead times as long as 50 days is impressive compared with other mechanisms for the MJO, with potential implications for forecasting such events.

Direct SST observations from the TMI data set were not available for the case study of 12 February 1997, so SST data from the ECCO reanalysis were used. These were compared with TMI SST data for other case studies and found to be consistent, although the magnitude of the ECCO anomalies was consistently about 50% smaller than the observed TMI anomalies. In addition, due to the lower resolution of the ECCO data, these SST anomalies have less small-scale noise than those derived from TMI data. For the case study starting 12 February 1997, the positive SST anomalies are preceded by some positive heat fluxes (Figure 3.3(e)). However, the shape and extent of the positive SST anomalies agree better with the density and vertical velocity anomalies in Figure 3.3(f) than with the surface fluxes, consistent with predominantly dynamic, as opposed to thermodynamic, forcing. The magnitude of these SST anomalies is between 0.2–0.5°C; given that these are likely to be an under-estimate of the true anomalies, they are certainly large enough to influence atmospheric convection.

Rossby waves have a variety of meridional modes; the first such mode is associated

with symmetric off-equatorial maxima (Chelton *et al.*, 2003) and appears to dominate the intraseasonal ocean dynamics over the higher modes which have more complicated structures (Chapter 2). The distance by which the SSH maxima of the first meridional mode Rossby waves are displaced from the equator is governed by the Rossby radius of deformation, but typically is of the order of 4–5° latitude (Chelton *et al.*, 2003). Analysis of the latitudinal structure of the Rossby waves observed here is consistent with first meridional mode waves.

The phase speed c of Rossby waves is governed by the baroclinic and meridional mode of the wave and by the stratification of the background state ocean through which it propagates. Equatorial Rossby waves (first baroclinic mode) follow the dispersion relation

$$c = \frac{-\beta}{k^2 + (2n+1)\beta/c_e}, \tag{3.1}$$

where $\beta \approx 2.3 \times 10^{-11}$ m^{-1} s^{-1} is the meridional gradient of planetary vorticity, k is the zonal wavenumber, n is the meridional mode number and c_e is the phase speed of the first baroclinic mode Kelvin wave. Kelvin waves are non-dispersive; typical values of c_e are around 2.4–3 m s^{-1}, depending on local stratification (Chelton *et al.*, 1998). Long Rossby waves with small k are approximately non-dispersive, with $n = 1$ Rossby waves propagating at 1/3 of the Kelvin wave phase speed, or approximately 0.9 m s^{-1}. However, in reality the Rossby wave phase speed is often weakly dependent on k such that for wavelengths of the order of 3000 km, c will be $\sim$15% slower than in the non-dispersive limit. Furthermore, Chelton *et al.* (2003) observed low frequency, first meridional mode Rossby waves to propagate roughly 30% slower than predicted in the Pacific, giving phase speeds of around 0.5–0.6 m s^{-1} even though these waves were approximately non-dispersive.

The phase speed of the Rossby waves we observe can be estimated from the slope of the lines in Figures 3.3(a,d). For both case studies, the wave travels approximately 35° longitude in 100 days, leading to a phase speed of 0.5 m s^{-1}. We visually estimate the uncertainty in this estimate to be roughly ± 0.1 m s^{-1}. This is slower than the non-dispersive first meridional, first baroclinic mode Rossby wave speed of around 0.9 m s^{-1} for this region (Chelton *et al.*, 1998). However, given that the wavelength of these waves is approximately 15-30° longitude, dispersive modifications to the phase speed will be non-negligible. Using a wavelength of 20° longitude, equation (1) gives a phase speed of

0.7 m s^{-1} for $c_e = 2.7$ m s^{-1}, which is not inconsistent with the phase speed observed. Zonal currents may influence the phase speed of these waves, although away from the Somali Current, the time-mean depth averaged zonal velocity preceding the two case studies is negligible. However, Chelton *et al.* (2003) showed that consideration of the shear generated by the asymmetric equatorial current system of the Pacific slowed the propagation of Rossby waves by around 0.2 m s^{-1}, which may partly explain the discrepancy seen here.

The SSH anomalies are symmetric about the equator (not shown), consistent with first meridional mode waves, but to confirm the baroclinic mode of the waves, it is necessary to examine their vertical structure. To analyse this, we show depth-longitude sections of density and vertical velocity, averaged over 2–6°S and 2–6°N (boxes in Figure 3.2), at lags -50 days to 0 (Figure 3.4). These show the propagation of a downwelling Rossby wave indicated by the westward propagation of negative density anomalies, and highlighted by the black diagonal arrow. The inverse relationship between the density and SSH anomalies can also be seen, consistent with baroclinic wave theory. As the sign of the vertical velocity anomalies is uniform with depth, and the density anomalies are unimodal with a single maximum around the depth of the pycnocline (roughly 100 m), these waves are most likely first baroclinic mode waves.

The vertical velocity anomalies are broadly in quadrature with the density and SSH anomalies, such that downwelling (negative vertical velocity anomalies) occurs at the leading (western) edge of the westward-propagating negative density anomalies. Given that the ocean is stably stratified, with background mean density increasing with depth, this suggests that the density anomalies arise predominantly through vertical displacements of isopycnals, as opposed to lateral advection or surface buoyancy fluxes. Furthermore, estimating the temperature advection from ECCO data (Figure 3.5) suggests that vertical temperature advection dominates, although horizontal advection is of the same sign and contributes around 25% of the total temperature advection in the top 100 m. The total mean temperature advection over this depth range corresponds to warming rates of up to 0.1°C per day. Assuming that this layer is fairly well mixed, and seeing that these anomalies persist for more than 10 days, the total cumulative temperature advection is sufficient to cause the observed SST anomalies. In addition, the deepening of the

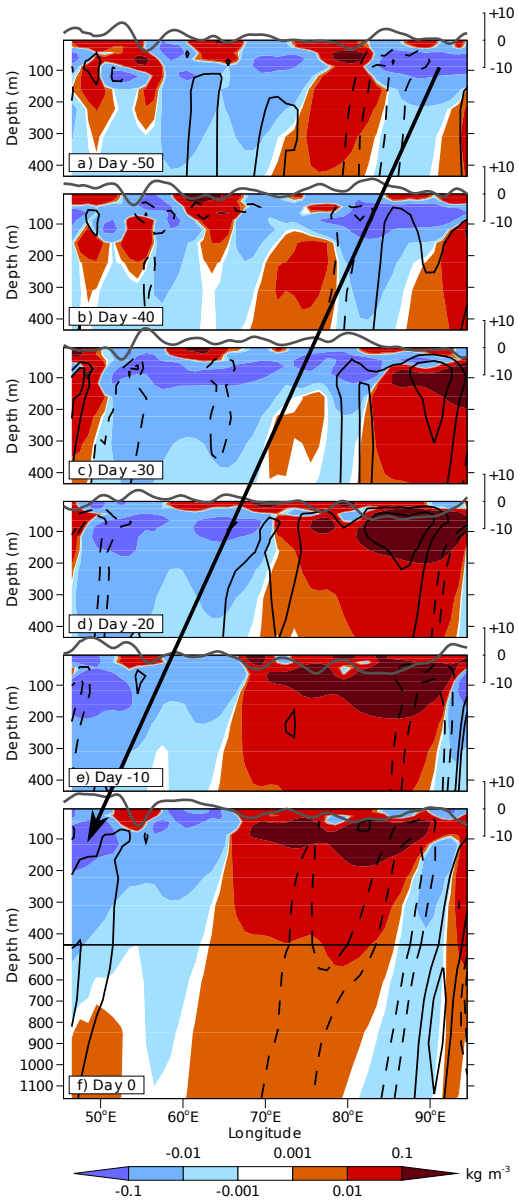

Figure 3.4: Density anomalies (shaded; see legend, in kg m^{-3}), vertical velocity anomalies (black contours) and SSH anomalies (grey contour along top of each panel; cm) at day (a) -50, (b) -40, (c) -30, (d) -20, (e) -10, (f) 0 relative to the primary event on 24 September 2004. The contour interval for the vertical velocity anomalies (positive upward) is 1×10^{-5} m s^{-1}; negative contours are dashed and the zero contour omitted. The bottom panel is extended down to 1160 m to show the magnitude of the anomalies in the deep ocean; note the discontinuity in the y-axis at 435 m. The diagonal arrow indicates the propagation of the downwelling Rossby wave that triggers the primary event, and is calculated using the algorithm described in the appendix.

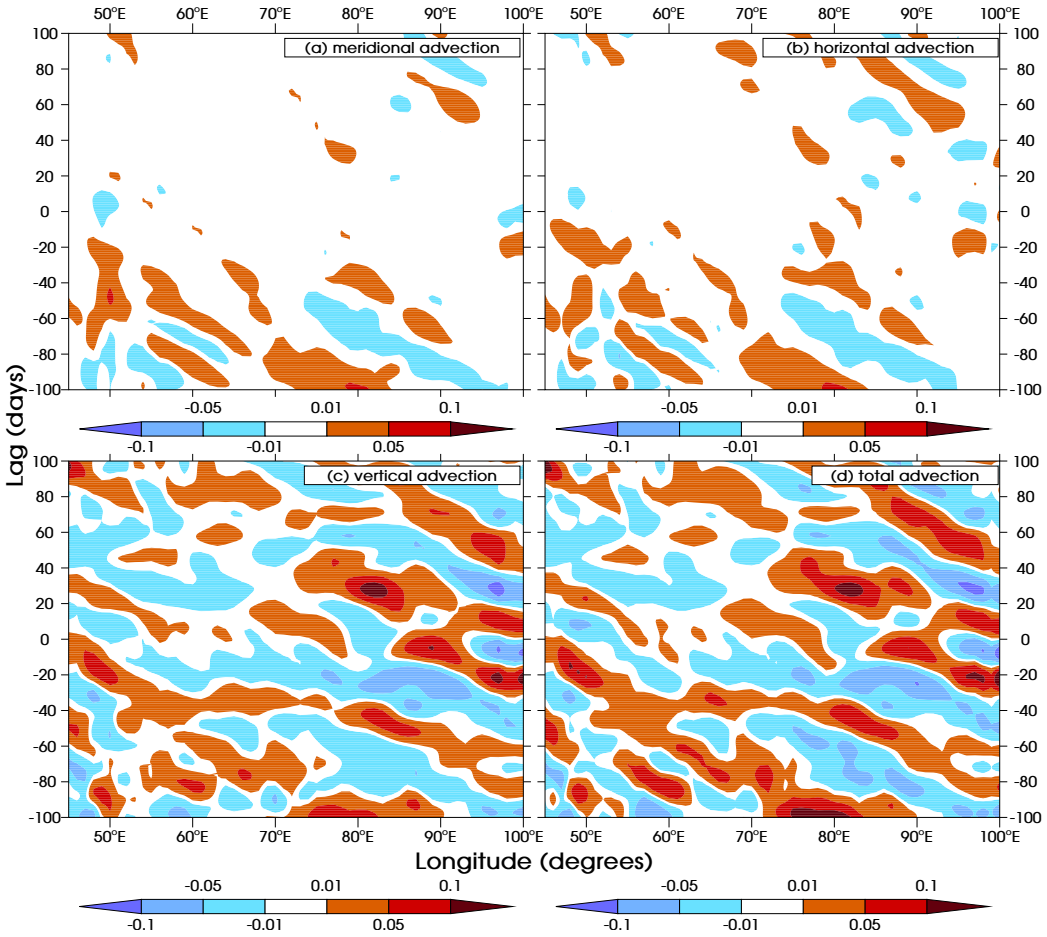

Figure 3.5: Profiles of (a) meridional, (b) horizontal, (c) vertical and (d) total temperature advection (shaded; see legend, in °C day^{-1}) averaged over depths of 10–100 m, calculated from mean temperature and velocity anomalies from the ECCO data set, for the case September 2004 case study.

mixed layer associated with this downwelling will inhibit the entrainment of cold, deep water, thus enhancing the positive SST anomalies (McCreary, 1983). From seasonally averaged density profiles the density anomalies can be converted to estimated perturbations to isopycnal depth: The anomalies of $\sim$0.1 kg m^{-3} seen in Figure 3.4 correspond to vertical perturbations of $\sim$5 m in the isopycnals at 75 m, consistent with vertical velocity anomalies equivalent to $\sim$1 m per day sustained over several days.

The anomalies in both vertical velocity and density extend down below 300 m (Figure 3.4(f)), associated with downward propagation of wave energy into the deep ocean, consistent with the results of Matthews *et al.* (2007, 2010). The westward tilt of the anomalies with depth is consistent with upward phase propagation and downward energy propagation. Because the vertical density gradients are less in the deep ocean, the magnitude of the density anomalies decreases with depth, but there are nevertheless anomalies

of around 0.005 kg m^{-3} at 1000 m, which is similar to the amplitude of the seasonal cycle at this depth (not shown).

3.6.2 Composites

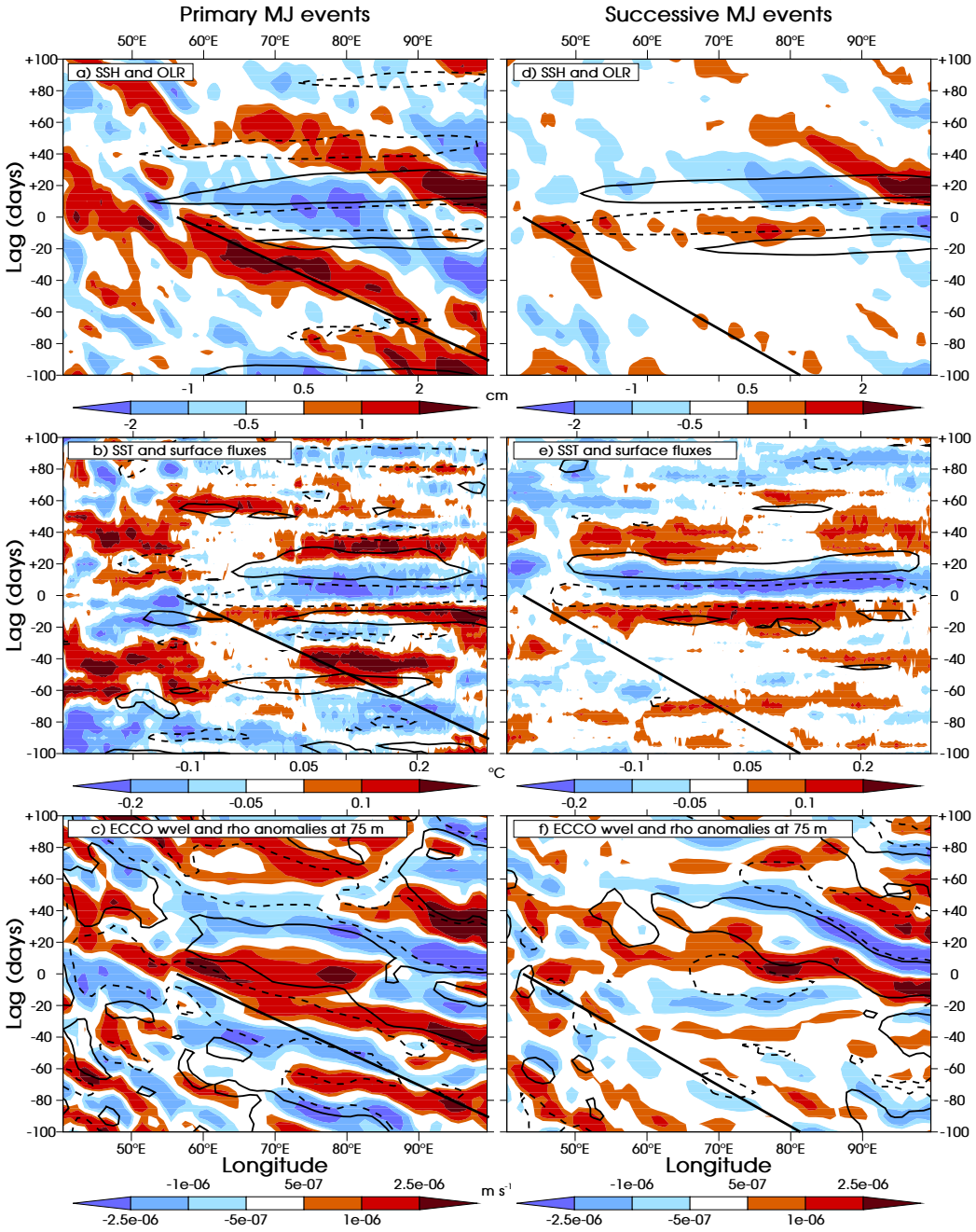

Figure 3.6: As Figure 3.3 but for (a-c) composite primary events and (d-f) composite successive events. The contour intervals are: a) and d) ±7.5 W m^{-2}, b) and e) ±10 W m^{-2}, c) and f) ±0.025 kg m^{-3}.

The case studies show the potential for primary MJ events to be triggered by the arrival of downwelling Rossby waves. Here, we examine how robust the relationship is in

general through composite analysis. Figure 3.6 shows composites of the same variables as in Figure 3.3; the left hand panels are composites over all primary MJ events, the right-hand panels are for successive MJ events. For the SST data, the TMI data were only available for primary events after 1998, but this contains 14 out of the 17 events used for the other composites.

Figure 3.6(a) shows that primary MJ events, as indicated by the negative (dashed) OLR contour at around lag 0, are consistently preceded by the arrival of a downwelling Rossby wave (westward-propagating positive SSH anomaly), supporting the hypothesis of such waves as a triggering mechanism. The wave signal is relatively coherent, although a little discontinuous, and is preceded by downwelling anomalies and colocated with negative density perturbations at 75 m (Figure 3.6(c)), consistent with deepening of the mixed layer. The propagation speed of the composite wave is approximately 0.6 m s^{-1}, slightly faster than in the case studies. Both the OLR anomalies, and the positive SSH anomalies associated with the triggering Rossby wave, are statistically significant at the 95% confidence level.

The immediate relationship between SSH and SST anomalies is less clear for the composites than for the case studies. There are positive SST anomalies in the region of interest (the western Indian Ocean) prior to the initiation of the primary MJ event, but they are relatively weak and do not propagate with the Rossby wave. Instead, the SST anomalies are zonally extensive and appear broadly consistent with surface fluxes, even if the dynamical forcing is also a factor. This is possibly an artefact of the methodology since the dynamically forced SST anomalies will be relatively localised compared with the zonally extensive flux-driven SST anomalies. Given that our definition of primary MJ events assigns day zero to peak OLR amplitude anywhere within the Indian Ocean, this may refer to MJ events triggered at a wide range of longitudes. This could lead to dynamically-induced SST anomalies being artificially "smeared out" in the composite analysis; we return to this question below. Note that the propagating SSH signal of the Rossby wave is still evident despite this smearing effect because this signal is more coherent than for SST and also stronger relative to the zonally-extensive wind stress forcing of SSH.

For successive MJ events, the composite analysis indicates a different story. There is

little evidence of propagating Rossby wave signals, although the SSH anomalies are positive immediately prior to the initiation of the successive events (Figure 3.6(d)). The SST anomalies are zonally extensive (Figure 3.6(e)) and broadly consistent with the theories of thermodynamic air-sea interaction within the MJO (Flatau *et al.*, 1997; Shinoda *et al.*, 1998), and also consistent with the results of Matthews (2008), who found that successive MJ events were consistently preceded by significant positive SST anomalies. Note that both the primary and successive MJ events do themselves trigger Rossby waves at the eastern boundary of the Indian Ocean (positive SSH anomalies propagating westward from lag 10 days, 100°E), in keeping with the findings of Chapter 2 and Oliver and Thompson (2010).

Figure 3.7 shows the depth-longitude sections of density and vertical velocity anomalies for the composite primary events. The vertical velocities are clearly in quadrature with the density anomalies, consistent with vertical motions being the primary cause of the density anomalies. These anomalies extend below 300 m, with composite density anomalies of up to 0.0025 kg m^{-3} at 1000 m; there is also a pronounced westward tilt with increasing depth below 500 m (Figure 3.7(f)), consistent with downward propagation of wave energy. Once again, the vertical structures of these waves support the hypothesis that they are first baroclinic mode waves whose phase speeds have been slowed by a combination of basic state currents and dispersive effects.

3.6.3 Relative Longitude

As discussed above, there is the potential for primary MJ events to be triggered at different longitudes; therefore the triggering Rossby wave signals will not be aligned in longitude, leading to a tendency for composite analysis to smear out the signal. This is especially true for variables such as SST anomalies where other, zonally extensive processes may mask the relatively localised influence of ocean dynamics. Indeed, analysis of the longitude of the arrival of the Rossby waves indicates a wide spread between 40 and 70°E. To account for this variability, the composites are aligned onto a new, relative longitude axis, such that the Rossby waves arrive at zero relative longitude. This methodology is described below.

The methodology used to create the relative-longitude composites was designed to

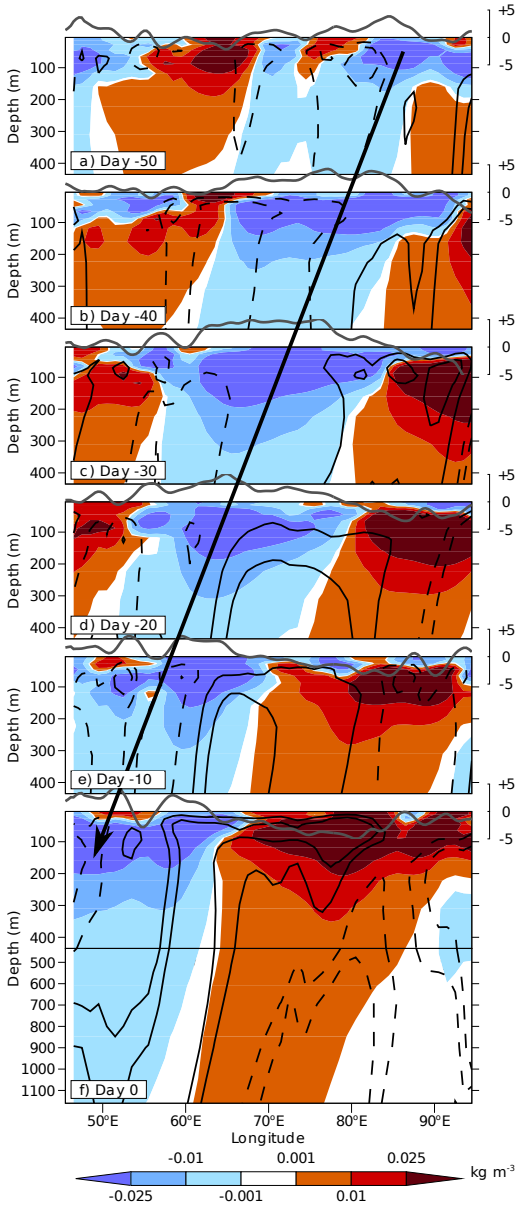

Figure 3.7: As Figure 3.4 but for composite primary events. The contour interval for the vertical velocity anomalies is 2.5×10^{-5} m s^{-1}.

objectively identify the arrival of a downwelling Rossby wave at the start (i.e., lag 0) of each MJ event. For each MJ event, we identify the "optimal" propagation line on the Hovmöller diagram of SSH anomalies over the Indian Ocean (40–100°E) between lag −100 days and lag 0 (e.g., Figure 3.8(a) for MJ event starting on 12 February 1997). We assume that for a Rossby wave to trigger a new MJ event, it must arrive in the *western* Indian Ocean, where the thermocline depth is shallower and large SST perturbations can be realised (see Figure 2.7 in Chapter 2). Hence, only "target" longitudes between 40 and 75°E are considered. We also assume that Rossby waves will only have "target" phase

speeds between -0.35 and -1.2 m s^{-1}, based on observations (Chelton *et al.*, 1998).

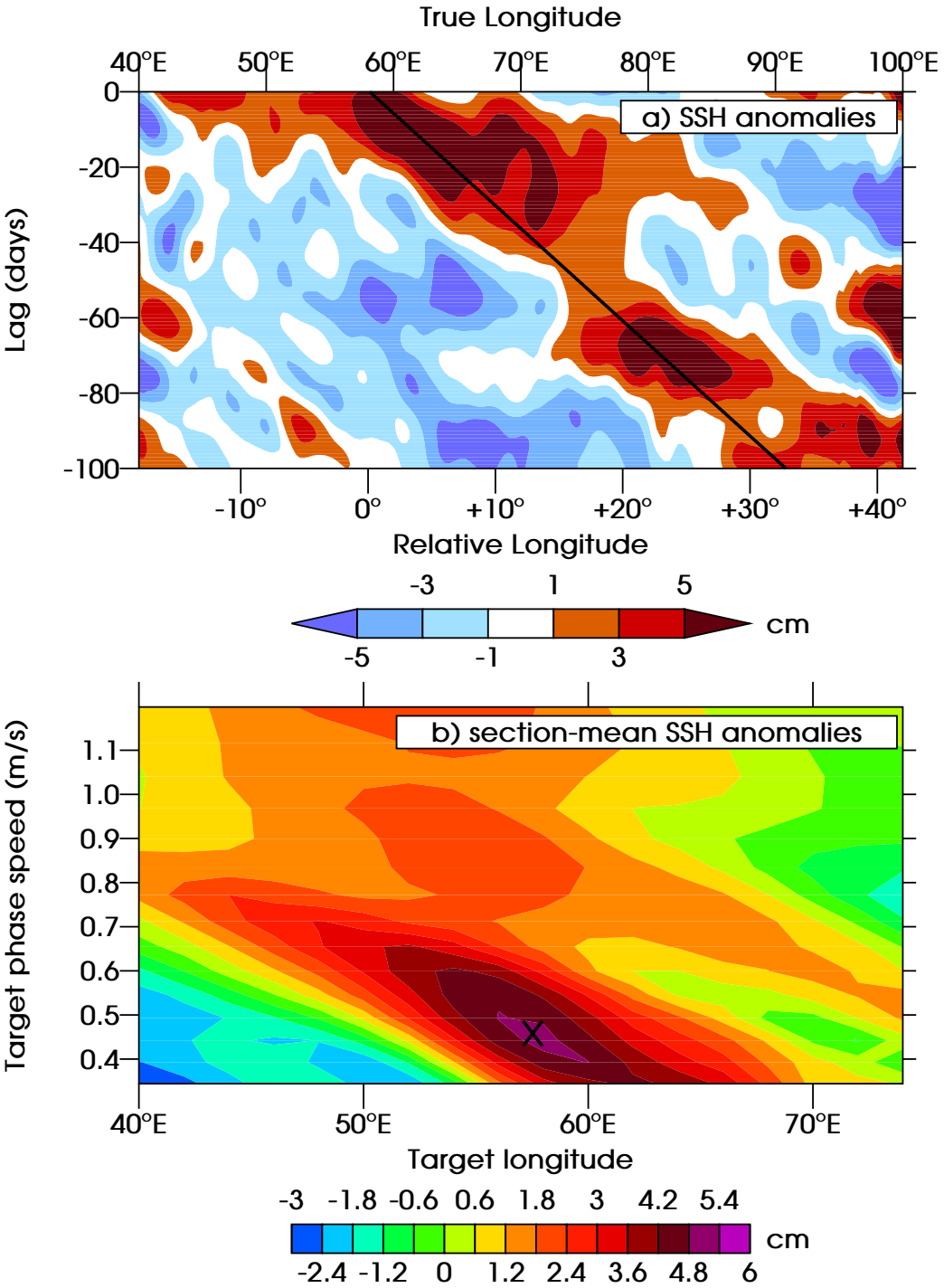

Figure 3.8: Example of the methodology used to calculate relative longitude: (a) SSH anomalies in cm for the primary event on 12 February 1997 with true longitude on the upper x-axis and the new, relative longitude on the lower x-axis. (b) mean along-path SSH anomalies for the range of target longitudes and phase speeds used in the method. The maximum mean SSH is indicated by the solid line in (a) and the cross in (b).

The best fitting target longitude λ, and phase speed c, is then determined for each case study. A propagation line is constructed for each λ-c pairing, i.e., a line whose slope

is determined by c, passing through longitude λ at lag 0. The SSH anomaly along this line is then calculated by interpolation from the data on the gridded Hovmöller diagram (Figure 3.8(a)). The mean of this SSH section is then calculated. Once this process has been repeated for each possible pair of target longitudes and phase speeds, the mean SSH can be plotted on axes of target longitude and phase speed (Figure 3.8(b)). The maximum value of mean SSH in this target longitude, phase speed parameter space is then found, and used to identify the optimal propagation line. For the example MJ event of 12 February 1997, this corresponds to a target longitude of 58°E, and a target phase speed of -0.44 m s^{-1} (cross in Figure 3.8(b)). When this optimal propagation line is plotted on the input Hovmöller diagram (diagonal line in Figure 3.8(a)), it can be clearly seen to capture the westward-propagating positive SSH anomaly.

The methodology is robust in that the example shown here has a clear unimodal maximum that can be identified from the parameter space diagram (Figure 3.8(b)). Results for other case studies were similar.

The target longitude for each MJ event was then used to remap variables onto a relative longitude axis. Hence, the target longitude corresponds to a relative longitude of zero, and points to the west (east) of the target longitude correspond to negative (positive) relative longitudes.

The results of the relative longitude composites are shown in Figure 3.9; the same variables are composited as in Figure 3.6. The composites only extend to relative longitude $-5°$, since any further extension to the west starts to impinge on Africa for many of the composite members. By construction, the SSH composite shows a westward-propagating positive SSH anomaly arriving on lag 0 days and zero relative longitude, for both primary (Figure 3.9(a)) and successive (Figure 3.9(d)) events. For primary MJ events, the propagating Rossby wave signal (positive SSH anomaly) is stronger and more coherent when expressed in relative longitude (Figure 3.9(a)) than in the "true longitude" composite (Figure 3.6(a)). The phase speed of the composite Rossby wave is roughly 0.5 m s^{-1}, as in the case studies. Note that the location of initiation for the primary MJ event, as defined by the negative OLR anomalies, is not constrained in any way by this compositing methodology. Therefore, the fact that the OLR anomalies in Figure 3.9(a) do begin very close to relative longitude 0 reinforces the hypothesis that such events are triggered by the

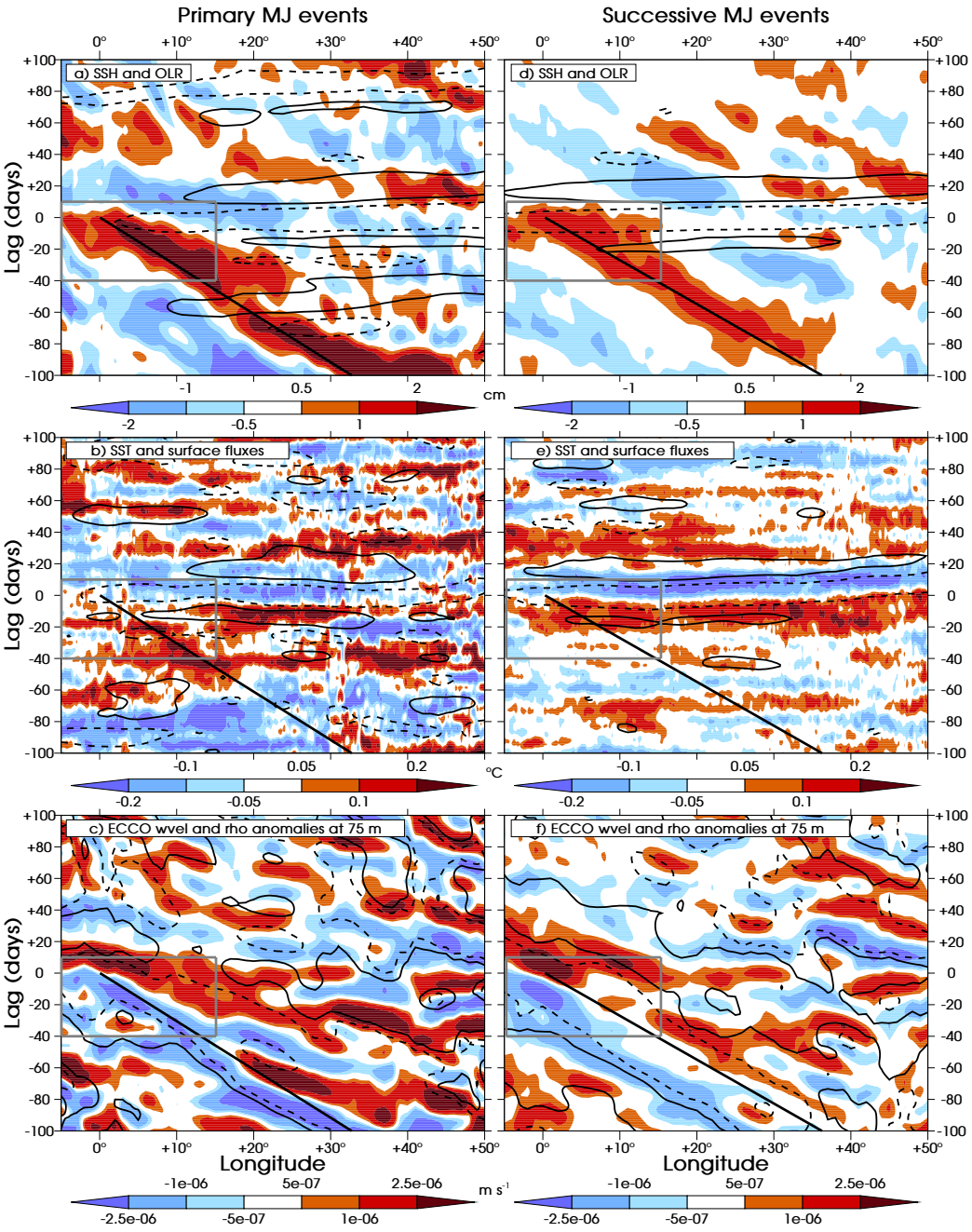

Figure 3.9: As Figure 3.6 but using relative longitude on the x-axis (see Appendix A for details). The grey box represents the area of particular interest in the western Indian Ocean where the downwelling Rossby wave has the greatest potential to trigger MJ events.

arrival of the Rossby wave.

Furthermore, once the downwelling Rossby wave arrives in the western Indian Ocean, where the thermocline is shallower, it is now colocated with coherently propagating SST anomalies (Figure 3.9(b), in the region indicated by the grey box). These SST anomalies have magnitudes around 0.15 °C, similar in magnitude to the composite flux-driven SST anomalies known to be important for thermodynamic air-sea coupling (Shinoda *et al.*, 1998, Figure 3.9(e)). These positive SST anomalies are generally not consistent with the surface flux anomalies, but are consistent with the vertical velocity and density anomalies at 75 m (Figure 3.9(c)), implying a dynamical forcing. The anomalies propagate coherently from 50 days prior to the triggering of the primary event, suggesting potential predictability. There is still some evidence for flux-driven SST anomalies in the eastern Indian Ocean prior to the primary event, but it is clear that the dynamically driven SSTs play a crucial role in the initiation of the primary events.

When successive MJ events are composited on relative longitude, there is also a coherent Rossby wave signal (Figure 3.9(d)). This is perhaps not surprising given that the methodology will locate any Rossby wave activity, whether or not such waves act as a trigger for convection. However, there is no coherent propagation of SST anomalies along the path of the Rossby wave signal; the SST anomalies are zonally homogeneous and consistent with surface flux forcing (Figure 3.9(e)). There are substantial vertical velocity and density anomalies at depth (Figure 3.9(f)), so it is somewhat surprising that a stronger SST signal is not seen. Consistent with this lack of a dynamically forced SST signal, the negative OLR anomalies begin substantially further west than the longitude of the Rossby wave signal at lag 0, out to -15° relative longitude (not shown). Hence, the arrival of the Rossby wave does not appear to be the primary trigger for successive MJ events. It is to be expected that the waves will still have an effect on the behaviour and frequency of successive events, but it is clear that other mechanisms are likely to be more important for successive events (Matthews, 2008).

3.7 Conclusions

The key conclusion of this paper is that primary MJ events can be triggered by the arrival of a downwelling ocean Rossby wave. This is supported by case study and composite

analysis. Given that no consistent trigger mechanism was found by Matthews (2008), this is substantial evidence for the importance of ocean dynamics for the MJO, as suggested in Chapter 2. Such feedbacks are likely to modulate MJO activity more generally, although observational evidence will be less clear when other triggering mechanisms are also important.

In contrast to primary events, successive MJ events do not appear to be consistently triggered by the arrival of a downwelling Rossby wave. This presents a slightly different perspective to that given in Chapter 2, where it was suggested that forcing from oceanic Rossby waves would affect all MJ events, thus providing a feedback mechanism that would enhance low-frequency MJO variability. The results presented here suggest that this oceanic forcing of the MJO is far stronger for primary events (a subset of the events used in Chapter 2) than for successive events. Nevertheless, this will have the effect of strengthening the low-frequency tail of the MJO since the frequency composition of primary events is, by definition, lower. It is interesting to note that air-sea interaction has been observed to occur more strongly within a lower-frequency component of the MJO in the Indian Ocean (Izumo *et al.*, 2010).

Figure 3.10 shows the proposed triggering mechanism for primary MJ events. The downwelling Rossby wave propagates in from the eastern Indian Ocean; these waves may have been triggered by reflection of equatorial Kelvin waves at the eastern boundary, or by direct forcing from equatorial wind stress curl. The wind stress which initially triggers these waves may be related to previous MJO activity, well separated from the subsequent primary MJ event by a period of quiescence, but other sources of intraseasonal wind variability are also likely to be important. The triggering Rossby wave is associated with positive (predominantly vertical) temperature advection, along with deepening of the mixed layer and thus reduction in the entrainment of cold water to the surface, leading to an increase in SST. This SST increase leads to moistening and warming of the atmospheric boundary layer over a large region, thus priming the atmosphere for convection and triggering a primary MJ event. Although the schematic shows the waves triggering a new event only upon reaching the western Indian Ocean, analysis of individual case studies suggests that events can be triggered anywhere between 40° and 70°E, where the MJO is typically triggered and the thermocline is relatively shallow.

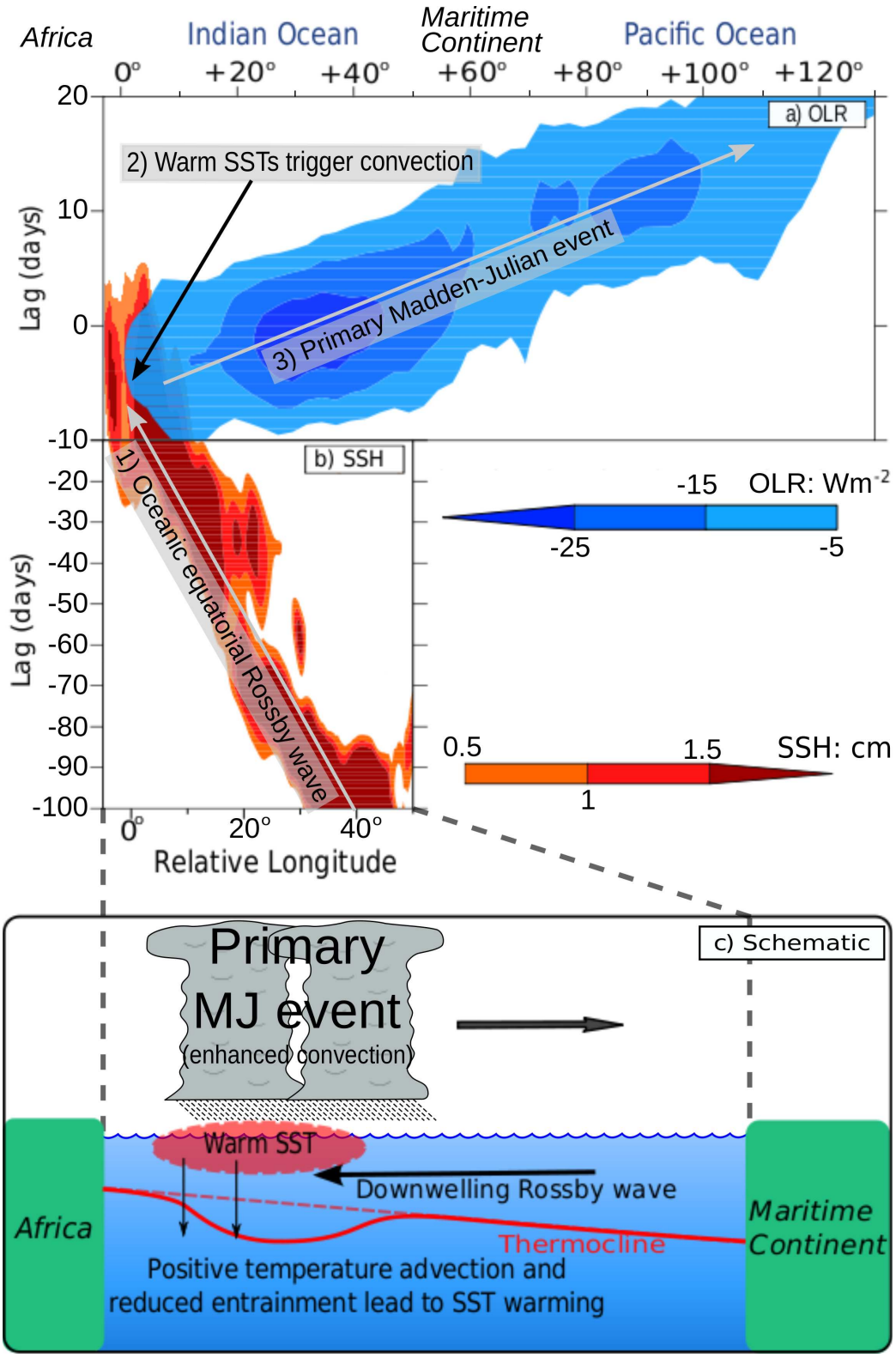

Figure 3.10: Triggering of primary Madden-Julian events by an oceanic equatorial Rossby wave. (a,b) Hovmöller diagrams of OLR and SSH anomalies (shaded; see legends) on relative longitude at lags −100 to +20 days relative to composite primary MJ events. Note the discontinuity in the y-axis at lag −10 days. (c) Schematic of triggering mechanism for primary MJ events, showing the relationships between the Rossby wave (positive SSH anomalies in (a) and (b)), downwelling, thermocline depth and SSTs which leads to the triggering of a primary MJ event, as shown by the negative OLR anomalies in (a).

It is interesting to examine these results in the light of previous studies of intraseasonal ocean dynamics in the Indian Ocean. It has been suggested that the propagation of Rossby and Kelvin waves will couple to the atmosphere, thereby enhancing atmospheric convection at time-scales of around 90 days (Han *et al.*, 2001; Han, 2005; Fu, 2007), consistent with the idea that such feedbacks will enhance the low-frequency tail of the MJO. Chapter 2 and Oliver and Thompson (2010) documented how the cyclical MJO can force equatorial Kelvin wave variability which subsequently generates both reflected Rossby waves and coastal Kelvin waves upon reaching the coast of Sumatra. In their composites based on the cyclical MJO, these Rossby waves do not coherently propagate as far as the western Indian Ocean. However, this is likely to be due to the fact that compositing on the cyclical MJO imposes a time scale that is shorter than the time taken for a Rossby wave to cross the Indian Ocean. Indeed, time-lag composites relative to a single MJO phase do show Rossby waves freely propagating as far as the western Indian Ocean (Figure 2.5 of Chapter 2). Therefore, these previous studies do not preclude the possibility that the Rossby waves observed to trigger primary MJ events could have been triggered by MJO activity some time beforehand, followed by a period of inactivity.

Forecasts of the MJO generally perform better when there is already an active MJ event in existence (Jones *et al.*, 2000). This is consistent with the observation by Matthews (2008) that successive events are associated with a multitude of triggering mechanisms that are relatively well understood, in contrast to primary events. The results presented here suggest that an accurate knowledge of the ocean state could offer predictability for primary events, especially as the propagation of oceanic Rossby waves is predictable at long lead times (potentially several months). Indeed, recent ensemble prediction of the MJO using a coupled model that was initialised with both atmospheric and oceanic analyses has shown significant improvement in skill for times when there is no initial MJO activity, i.e., primary events (Rashid *et al.*, 2011). It would be interesting to analyse whether the inclusion of SSH data in statistical forecasts of the MJO also improves skill scores. The potential for Rossby waves to trigger a primary event will likely depend upon atmospheric conditions also being suitable for the generation of an MJ event. Nevertheless, the results presented here suggest that monitoring Rossby waves in the Indian Ocean, through a combination of data from moorings, ARGO floats and satellite altimetry, is a

worthwhile undertaking that might help predict primary MJ events.

Another consideration that will affect the strength of this proposed forcing mechanism is the degree to which SSTs depend upon mixed-layer depth. For example, McPhaden (1999) noted that the shoaling of the thermocline following the 1997-98 El Niño event only led to a reduction of SSTs once the wind-induced mixing increased sufficiently to entrain the cold deep waters to the surface. Therefore, it should be expected that the effect of downwelling (or indeed upwelling) waves on SSTs will be dependent on the degree of wind-induced mixing and the depth of the basic-state thermocline. However, given that the thermocline is relatively shallow in the western Indian Ocean, it follows that wind-mixing will be relatively efficient at modifying SSTs here. Indeed, the western Indian Ocean is known to be a region where SSH and SST are well correlated (Xie *et al.*, 2002), thus making it a prime region for coupling between ocean dynamics and convection.

A limitation of this study is the small sample size available for primary MJ events, which increases the potential for sampling error in the results. This is unavoidable given the relatively short period over which satellite data have been available. Modelling studies of this dynamical forcing mechanism would be worthwhile, albeit contingent on the identification of a coupled model which adequately simulates all the relevant processes. Further work would also be useful to identify whether forcing by the ocean dynamics could also be responsible for "terminal" events, where the MJO goes from active to inactive. Some of the processes are investigated further using idealised modelling in Chapter 5.

3.8 Acknowledgments

The altimeter products were produced by Ssalto/Duacs and distributed by Aviso with support from Cnes and are available at `www.aviso.oceanobs.com/`. The TMI SST data were obtained from the SSM/I website at `www.ssmi.com/tmi/`. The ECMWF surface flux data were obtained through the British Atmospheric Data Centre (BADC) and from the ECMWF website at `data-portal.ecmwf.int/data/d/interim_{}daily`. The interpolated OLR data were obtained from the NOAA/OAR/ESRL PSD web site at `www.cdc.noaa.gov/`. TRMM rainfall data were obtained from `trmm.gsfc.nasa.gov/`. Data from the ECCO-GODAE project were obtained through the

ftp site `www.ecco-group.org/`. The research presented in this paper was carried out on the High Performance Computing Cluster supported by the Research Computing Service at the University of East Anglia.

Chapter 4

A linearised ocean general circulation model

4.1 Description

Here we provide an overview of the numerical model used for simulating the equatorial ocean dynamics in Chapter 5. This is a linearised general circulation model based on the one developed by Stevens (1988) and the one described by Webb (1996). It is similar in form to the GFDL Modular Ocean Model (MOM), that in turn is based on the code of Bryan (1969), Semtner (1974), and Cox (1984). MOM has been used extensively for modelling problems from across oceanography, and a similarly linearised model to the one used here was applied to study the spin-up of the North-Atlantic (Anderson *et al.*, 1979). An overview of the model code is presented here, along with a discussion of its performance and some simple test simulations.

The model is well suited to idealised studies of equatorial ocean dynamics as it does not have nonlinear processes within it, nor does it contain atmosphere-ocean coupling. This simplicity does limit the generality of the conclusions, but it also provides a clean framework in which to assess the processes of interest. The relation between forcing and response can be readily identified and sensitivity studies can be conducted without being complicated by unwanted effects.

The model is a level-coordinate ocean model, whose design is shown schematically in Figure 4.1. The model is configured quasi-globally (the Arctic and the Nordic Seas north

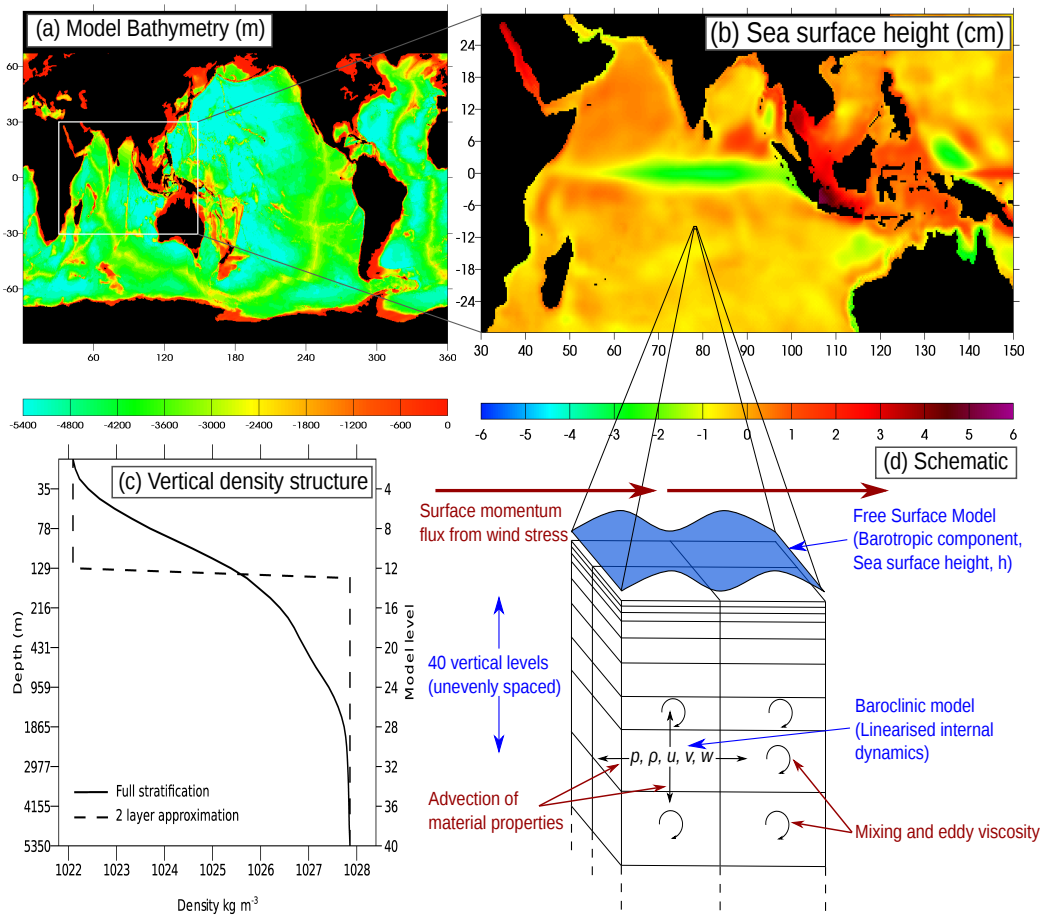

Figure 4.1: Schematic of the model. a) Map of the bathymetry used in the model, b) representative map of sea surface height (shaded, cm; see legend) in the Indian Ocean region from an idealised model run, c) mean vertical density profile that the model is initialised with, d) schematic of model grid, numerical schemes and their interactions.

of 67° N are omitted), with a horizontal resolution of $1/3° \times 1/3°$ and 40 uneven levels in the vertical that vary smoothly from 10 m thickness at the sea surface to 300 m thickness at depth.

Variables are arranged in the horizontal according to the Arakawa B grid (Figure 4.2(a), Arakawa and Lamb, 1977). This grid structure has been shown to do well at simulating flow that is dominated by the Coriolis term (since the Coriolis term can be represented without averaging), but can lead to dispersion errors and 'checkerboarding' in simulating gravity waves. The vertical structure of the model is shown in Figure 4.2(b), with all variables other than vertical velocity in the centre of the grid. This is the most suitable structure for variables in the vertical since the calculation of vertical advection and continuity are possible without averaging.

The model does not contain any time-mean currents. It is initialised with a single mean

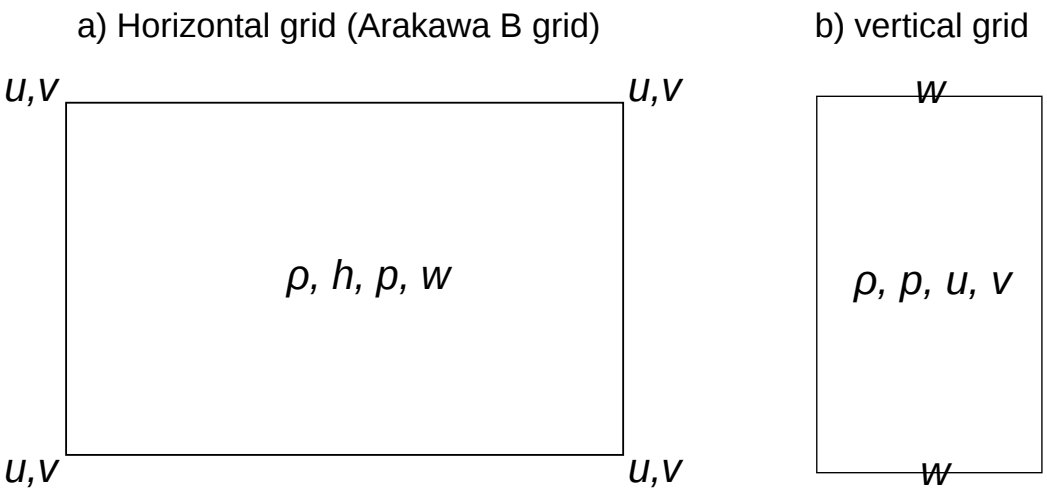

Figure 4.2: Schematic showing the layout of variables in the model; a) horizontal 'B grid', b) vertical grid

vertical potential density stratification, $\bar{\rho}(z)$ that is independent of horizontal position. This is derived from the mean stratification over the tropical Indian Ocean, since that is the area of most interest for this thesis. The data for this initial stratification come from the WOCE ocean atlas (Conkright *et al.*, 2002); see section 4.3 for discussion of the robustness of this choice.

The lack of currents is a major simplification in the model, and may have important implications for the conclusions that can be derived from the model simulations. For example, (Chelton *et al.*, 2003) showed that the equatorial current systems in the Pacific have a detectable influence on both the propagation speed and the meridional structure of the equatorial first mode baroclinic Rossby waves there. This influence occurs through the modification of the meridional potential vorticity gradients as opposed to through simple Doppler shifting by the mean current strength. McPhaden and Ripa (1990) show that this latter effect would only modify the phase speed of a Rossby wave by around 10% of the current speed for the narrow equatorial current systems. It is not trivial to incorporate the effects of these currents into the model, since minor innaccuracies in the location and structure of the currents could generate large discrepancies in the subsequent impact on wave propagation. Therefore it is outside the scope of the simple linear modelling study undertaken in Chapter 5 to attempt to include currents into the model. Given the scale of the modification found by (Chelton *et al.*, 2003), it is expected that the results will nevertheless be first-order accurate.

The model equations are formulated in spherical coordinates, with ϕ and λ representing latitude and longitude respectively, while z is the vertical coordinate. The equations of motion are thus

$$\frac{\partial u}{\partial t} - fv = -\frac{1}{\rho_0 a \cos\phi}\frac{\partial p}{\partial \lambda} + A_h \nabla^2 u + K_m \frac{\partial^2 u}{\partial z^2}, \tag{4.1}$$

$$\frac{\partial v}{\partial t} + fu = -\frac{1}{\rho_0 a}\frac{\partial p}{\partial \phi} + A_h \nabla^2 v + K_m \frac{\partial^2 v}{\partial z^2}, \tag{4.2}$$

$$\frac{\partial p}{\partial z} = -\rho g, \tag{4.3}$$

$$\frac{1}{a\cos\phi}\frac{\partial u}{\partial \lambda} + \frac{1}{a\cos\phi}\frac{\partial}{\partial \phi}(v\cos\phi) + \frac{\partial w}{\partial z} = 0, \tag{4.4}$$

$$\frac{\partial \rho}{\partial t} + w\frac{\partial \bar{\rho}}{\partial z} = K_h \frac{\partial^2 \rho}{\partial z^2}, \tag{4.5}$$

where

$$\nabla^2(\mu) = \frac{1}{a^2\cos^2\phi}\frac{\partial^2 \mu}{\partial \lambda^2} + \frac{1}{a^2\cos\phi}\frac{\partial}{\partial \phi}\left(\frac{\partial \mu}{\partial \phi}\cos\phi\right).$$

The variables $t,\ u,\ v,\ w,\ p,\ \rho,$ represent time, zonal velocity, meridional velocity, vertical velocity, pressure, and density anomaly, respectively. The radius of the Earth is $a,\ g$ is the acceleration due to gravity, and ρ_0 is a reference potential density. The Coriolis parameter $f = 2\Omega\sin\phi$, where Ω is the speed of angular rotation of the Earth. The horizontal eddy viscosity is $A_h = 10^3$ m^2 s^{-1} and the vertical eddy viscosity, K_m and diffusivity, K_h, are both set to 10^{-4} m^2 s^{-1}. The vertical velocity, w, is calculated by integrating the continuity equation (4.4) from the ocean floor (where $w = 0$) upwards.

At the ocean surface a wind stress $\left(\tau_s^\lambda, \tau_s^\phi\right)$ is applied and related to the ocean velocities by

$$\rho_0 K_m \frac{\partial}{\partial z}(u, v) = (\tau_s^\lambda, \tau_s^\phi)$$

and no flux of density is prescribed.

The model is forced with surface wind stress, either idealised or realistic, the latter being derived from reanalysis winds interpolated onto the model grid. This surface momentum flux generates vertical motion through Ekman pumping or suction, that subsequently leads to anomalies in both sea surface height (SSH) and density. These anomalies

subsequently generate horizontal and vertical motion in accordance with thermal wind balance and the resulting anomalies propagate as baroclinic and barotropic waves. Eventually these processes will lead to the spin-up of a pseudo-realistic ocean circulation, but for the present study, only the propagation of waves is of interest. These waves are predominantly linear processes (especially for the first few baroclinic modes), so the use of a linear model is reasonable.

The lack of interaction with the atmosphere is an obvious limitation to the model, as is the lack of any surface heat fluxes. It must therefore be assumed that any real-world coupled feedbacks that influence the atmospheric variability will be incorporated in the atmospheric reanalysis data used to force the model. The lack of surface heat fluxes and of any explicit formulation of mixed-layer thermodynamic processes limit the degree to which the feedback from the waves onto the MJO can be assessed, and this must be inferred from observations or physically-based estimates. The latter can be achieved by analysing the ECCO ocean state estimate to calculate vertical heat fluxes and mixed layer depth anomalies from observed case studies or composites. Nevertheless, further modelling work to investigate the strength of feedbacks onto the atmosphere using a coupled model with a high resolution mixed layer model embedded would be worthwhile.

4.2 Numerical Formulation

The baroclinic and barotropic components of the velocity field are solved separately. The rationale behind this separation is that the barotropic circulation contains fast propagating gravity waves that require a much shorter time step to simulate accurately than any baroclinic process. The equations of motion for the baroclinic component of the model are discretised using Bryan's (1969) scheme and the barotropic component follows (Killworth *et al.*, 1991). The solution has the very important property of being energetically consistent and causing no erroneous sources of energy.

The numerical stability of all such numerical models depends on the choice of grid spacing, time step, eddy viscosity and eddy diffusivity. The most basic criterion is the Courant-Friedrichs-Lewy (CFL) condition that states that no information should propagate more than a single grid box in a given time step. For this reason it is necessary to a have a smaller time step in the barotropic component of the model, since the propagation

of the fastest barotropic gravity waves greatly exceeds the fastest propagating baroclinic waves.

The timestep limitation due to the horizontal viscosity terms can be expressed as

$$\Delta t^v < \frac{\Delta^2_{\text{min}}}{8A_h}.$$

where Δ_{min} is the minimum grid spacing and Δt^v is the momentum equation time step. In order for the viscous lateral boundary layer to be properly resolved, the following criterion must be satisfied:

$$A_h > \beta\Delta^3_{\text{max}} \quad \text{where} \quad \beta = \frac{\partial f}{\partial \phi}$$

where Δ_{max} is the maximum grid spacing. For this model, A_m is set to 10^3 m^2 s^{-1}, which is similar to the viscosity of peanut butter. This may have important implications for the simulated flow, but is an inescapable problem in ocean modelling. It is generally held that the large scale flow can be simulated fairly accurately despite this discrepancy. Note that this is not an explicit viscosity, but instead a parameterisation of sub-grid scale processes.

4.3 Tests of the Model

Here we perform some rudimentary tests to ensure that the model is accurately simulating the propagation of Kelvin and Rossby waves. These tests will be compared to observations from satellite altimetry for sea surface height, and to output from the ECCO GODAE ocean state estimate (Wunsch and Heimbach, 2007) for the sub-surface velocity structure. Note that there are other tests and comparisons performed in Chapter 5, which further underline the solid performance of the model.

The first test is of the baroclinic Kelvin and Rossby wave speeds. For this a pseudo-impulsive forcing representative of a westerly wind burst over the western Indian Ocean was used, which triggers a freely-propagating equatorial ocean Kelvin wave response that subsequently reflects into an equatorial ocean Rossby wave at the eastern boundary. Figure 4.3 shows the propagation of these waves; the black lines on these Hovmöller diagrams shows the phase speed in each case, calculated using the methodology in section 3.6.3. For the Kelvin wave, this phase speed is 2.4 m s^{-1}, and for the Rossby wave it is 0.9 m s^{-1}. Although there is a slight discrepancy between these figures (the Kelvin wave

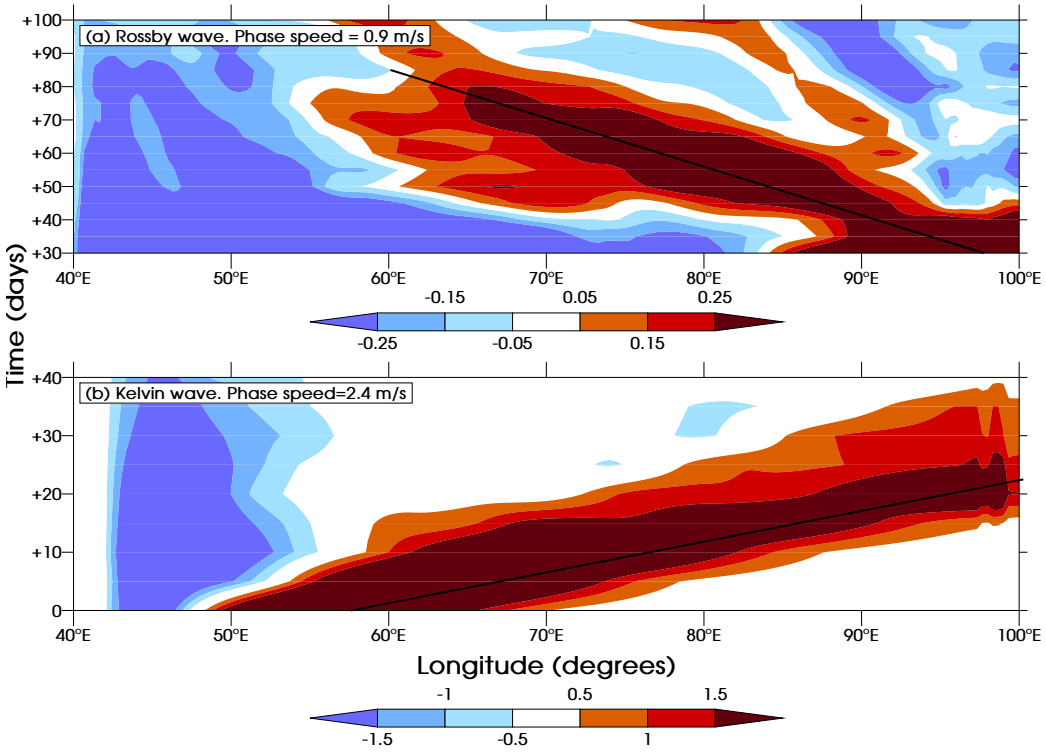

Figure 4.3: Hovmöller diagrams for a test run of the model, forced with a Gaussian wind patch centred on the equator at 50°E. a) SSH (shaded, cm; see legend) averaged over 2°S–2°N to highlight the Kelvin wave propagation, b) as in (a) but averaged over the Rossby wave guide, 2°–6°N/S.

speed should theoretically be exactly three times the Rossby wave speed), they are both consistent with the results of (Chelton *et al.*, 1998), who found first baroclinic mode Kelvin wave phase speeds in the range of 2.4–2.9 m s^{-1} in the equatorial Indian Ocean. These would correspond to Rossby wave phase speeds of 0.8–1.0 m s^{-1}. Note that the full range of phase speeds within the equatorial oceans is approximately 2.0–3.2 m s^{-1}, so these result for the Indian Ocean are broadly applicable to the majority of the ocean basins. It can thus be concluded that the choice of mean stratification for the model is reasonable.

The second test is to compare the SSH field from the model with satellite observations. To do this, we used composite surface winds from the ERA-Interim reanalysis for each of the eight phases of the MJO defined by Wheeler and Hendon (2004). We then assumed a constant interval of six days between phases to allow cubic interpolation from the phase composites to daily wind fields. These winds were then spatially interpolated onto the model grid from the 1.5° reanalysis data. The model is run for two MJO cycles to avoid spin-up issues. Figure 4.4 shows the comparison of the SSH from model days 54, 66, 78

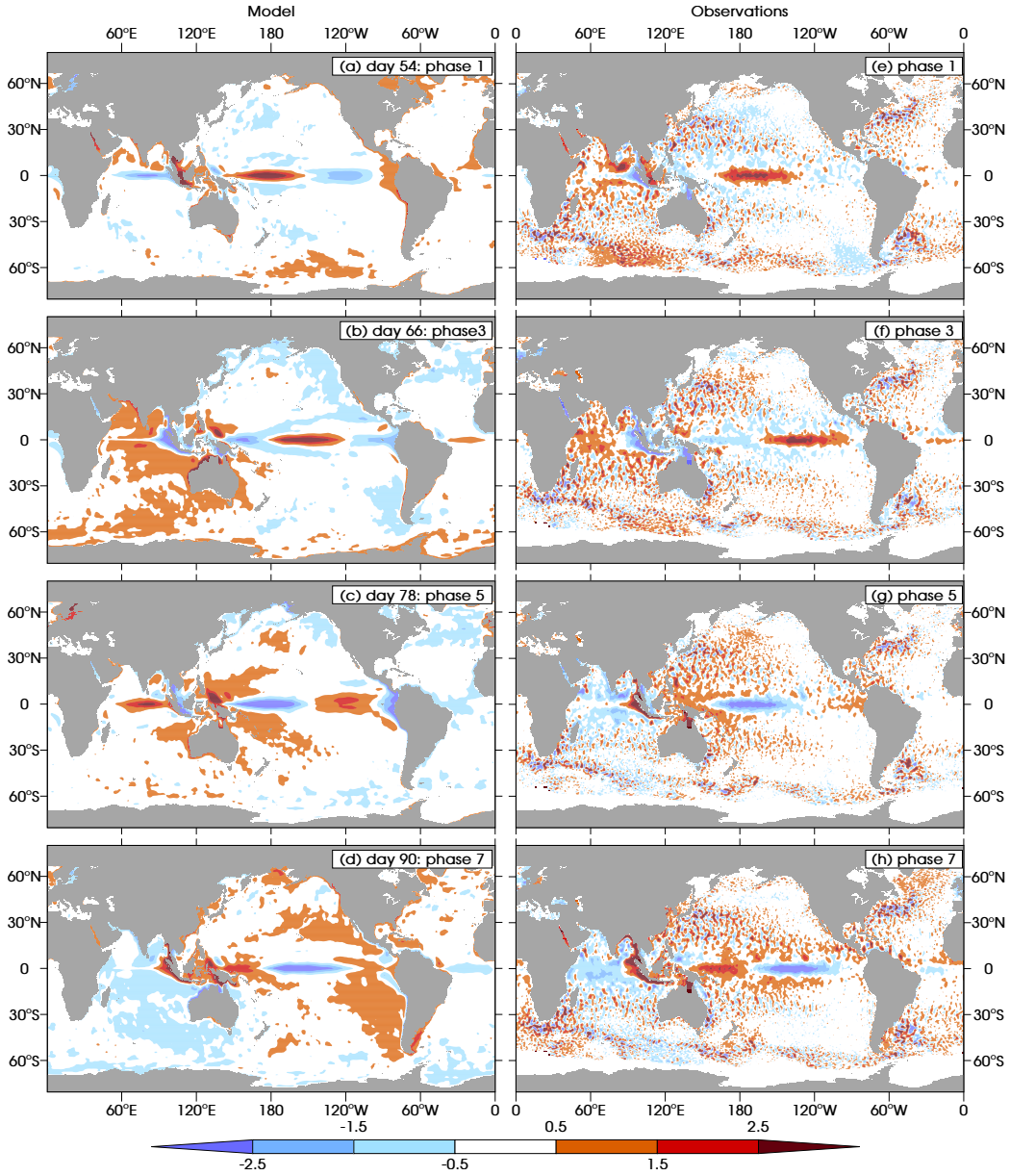

Figure 4.4: SSH anomalies (cm) (a–d) from the model run with cyclical MJO composite surface wind forcing, taken from days 54, 66, 78 and 90 corresponding to (e–h) Composite SSH anomalies (cm) from satellite altimetry observations for MJO phases 1, 3, 5 and 7.

and 90 with observed SSH composites for phases 1, 3, 5 and 7 of the MJO respectively. The agreement is strikingly good considering the relatively low resolution of the forcing wind data compared to the high resolution satellite altimetry. Various similar features are evident, such as the propagation of equatorial ocean Kelvin waves across the Pacific and the coastal Kelvin waves around the Bay of Bengal in the Indian Ocean. It therefore appears that not only is the model accurately simulating the linear dynamic ocean response to the MJO, but that the SSH composites for the MJO are comprised of this and little else;

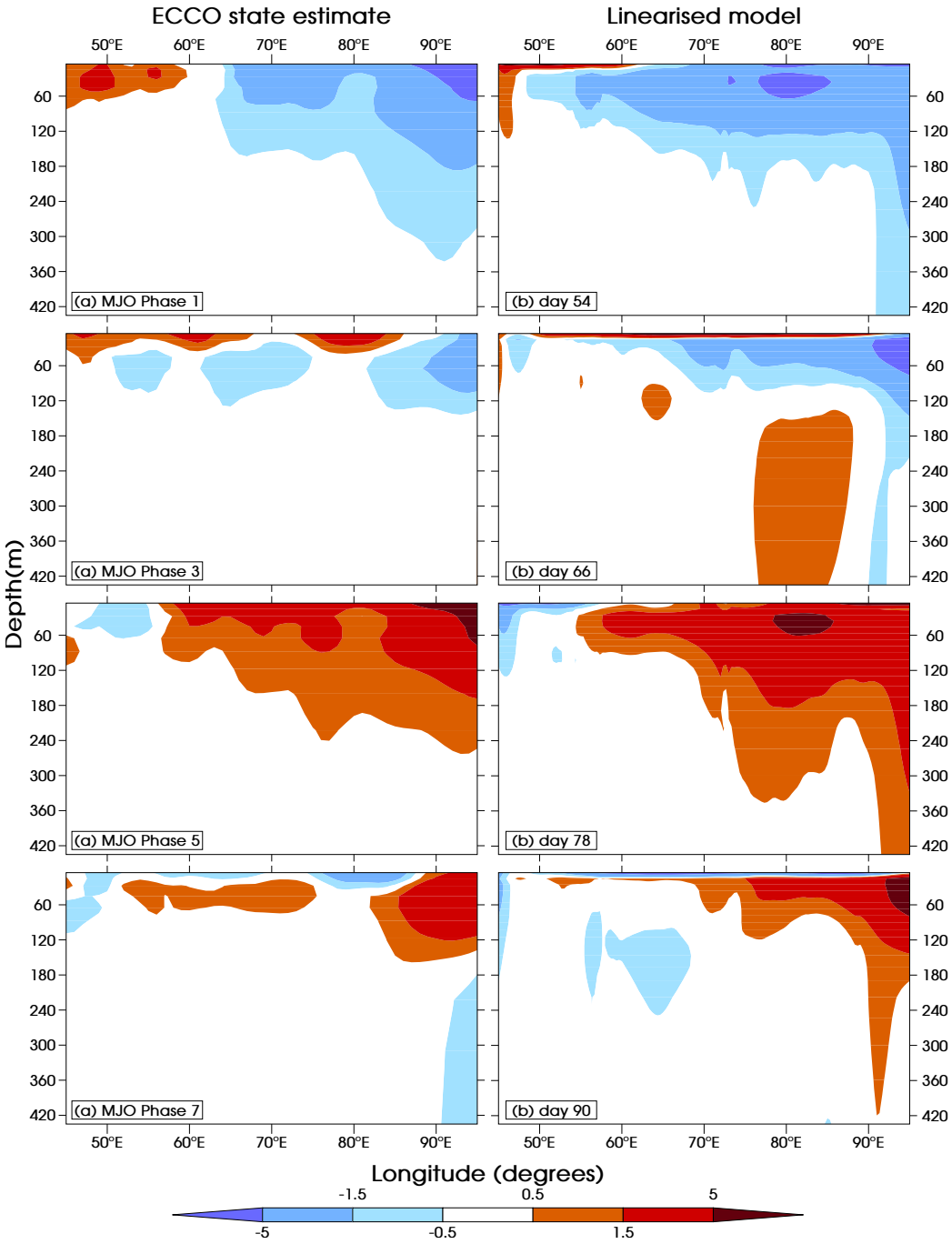

Figure 4.5: Depth-longitude sections of zonal velocity anomalies (cm s^{-1}) averaged over the Rossby wave guide of 2–6°N/S. (a–d) from the model run with cyclical MJO composite surface wind forcing, taken from days 54, 66, 78 and 90 corresponding to (e–h) Composite zonal velocity anomalies from the ECCO ocean state estimate for MJO phases 1, 3, 5 and 7.

nonlinearities are not important to first order. In addition, the similarity confirms the assumption that the lack of currents in the model is not of first-order importance.

The final test of the model is to analyse the vertical structure. To do this, we use

the same model run as for the SSH comparison above, but this time examine the subsurface zonal velocities along the equatorial waveguide in the Indian Ocean. These are then compared to the equivalent zonal velocities from the ECCO ocean reanalysis. Figure 4.5 shows depth-longitude sections averaged over the latitude band of 2°S–2°N, for the upper 500 m of the ocean. This shows a very good agreement between the model and the ocean state estimate, especially below the mixed layer. Within the mixed layer, there may be nonlinear processes that are not simulated by the model that are important, thus leading to discrepancies. Nevertheless, the vertical propagation of wave energy seems to be fairly well simulated by the model, although there is slightly more energy at depth near the eastern boundary in our model. Given the success of these tests, and the further agreements presented in Chapter 5, it is concluded that the model is fit for the purpose of simulating the equatorial waves in question.

Chapter 5

Dynamical ocean forcing of the Madden-Julian Oscillation at lead times of up to five months

5.1 Preface

This chapter consists of a paper which is press in the Journal of Climate, with the same title (Webber *et al.*, 2012b). The manuscript is unchanged from the paper apart from the model description, which has been trimmed to avoid repetition of parts of Chapter 4. In addition, there have been minor superficial changes to the figures, and all references to Webber *et al.* (2010) have been changed to "Chapter 2", and all references to Webber *et al.* (2012a) changed to "Chapter 3". BGMW was responsible for the majority of the work, under supersvision by AJM, KJH and DPS who provided scientific input and helped revise the text for publication. DPS was responsible for the design of the numerical ocean model used. The comments of three anonymous reviewers also helped to improve the manuscript.

5.2 Abstract

We show that a simple three-dimensional ocean model linearised about a resting basic state can accurately simulate the dynamical ocean response to wind forcing by the Madden-Julian Oscillation (MJO). This includes the propagation of equatorial waves in

the Indian Ocean, from the generation of oceanic equatorial Kelvin waves to the arrival of downwelling oceanic equatorial Rossby waves in the western Indian Ocean, where they have been shown to trigger MJO convective activity. Simulations with idealised wind forcing suggest that the latitudinal width of this forcing plays a crucial role in determining the potential for such feedbacks. Forcing the model with composite MJO winds accurately captures the global ocean response, demonstrating that the observed ocean dynamical response to the MJO can be interpreted as a linear response to surface wind forcing.

The model is then applied to study "primary" Madden-Julian events, which are not immediately preceded by any MJO activity nor by any apparent atmospheric triggers, but have been shown to coincide with the arrival of downwelling oceanic equatorial Rossby waves. Case study simulations show how this oceanic equatorial Rossby wave activity is partly forced by reflection of an oceanic equatorial Kelvin wave triggered by a westerly wind burst 140 days previously, and partly directly forced by easterly wind stress anomalies around 40 days prior to the event. This suggests predictability for primary Madden-Julian events on times scales of up to five months, following the re-emergence of oceanic anomalies forced by winds almost half a year earlier.

5.3 Introduction

The dynamics of the equatorial oceans are dominated by equatorial Kelvin and Rossby waves, on time scales from intraseasonal (Kessler *et al.*, 1995; Hendon *et al.*, 1998) to interannual (Battisti, 1988; McPhaden, 1999). These are planetary scale internal waves with wavelengths of thousands of km that affect sea surface height (SSH) and pycnocline depth. Variations in pycnocline depth are several orders of magnitude larger than the SSH anomalies and have the opposite sign; thus positive SSH anomalies correspond to a deeper mixed layer depth (MLD) and are associated with downwelling anomalies at their leading edge. Such waves are often referred to as downwelling waves, although they are also associated with upwelling anomalies at their trailing edge. This variability modifies the upper-ocean heat content and the mixing of cold subsurface waters, leading to changes in sea surface temperature (SST; McCreary, 1983; Battisti, 1988). These SST anomalies subsequently modulate atmospheric convection; such processes have been shown to be important for the El Niño-Southern Oscillation (ENSO; Battisti, 1988; Kessler and

McPhaden, 1995; McPhaden, 1999) and the Madden-Julian Oscillation (MJO; Chapter 2, Han *et al.*, 2001).

Equatorial Kelvin waves exhibit a single equatorial SSH maximum while equatorial Rossby waves have more complex meridional structures, the simplest and most commonly observed being the first meridional mode with symmetric off-equatorial SSH maxima (Chelton *et al.*, 2003). A westerly wind burst on the equator will generate Ekman convergence, thus forcing a positive SSH anomaly on the equator, along with downwelling anomalies and an eastward current. These anomalies propagate along the equator as a downwelling Kelvin wave (Giese and Harrison, 1990). Westerly wind bursts will typically also trigger upwelling Rossby waves due to off-equatorial Ekman divergence, although this is somewhat dependent on the meridional structure of the wind stress (Chelton *et al.*, 2003).

For a continuously stratified ocean there are an infinite number of vertical (baroclinic) modes for both equatorial waves, in addition to the barotropic mode (sometimes referred to as the zeroth baroclinic mode). However, typically only the barotropic and first few baroclinic modes are observed to be important (Giese and Harrison, 1990; Chelton and Schlax, 1996; Wunsch, 1997). The propagation speed of such waves depends upon both the baroclinic mode and the stratification of the fluid through which they propagate. Equatorial Kelvin waves are nondispersive with the first baroclinic mode ($n = 1$) phase speed c_e between approximately 2.4 and 3.0 m s^{-1}, depending on the local stratification (Chelton *et al.*, 1998). The first baroclinic mode equatorial Rossby wave phase speed, c, also depends on the meridional mode (Chelton *et al.*, 2003), and follows the dispersion relation

$$c = \frac{-\beta}{k^2 + (2m+1)\beta/c_e},$$

where $\beta \approx 2.3 \times 10^{-11}$ m^{-1} s^{-1} is the meridional gradient of planetary vorticity, k is the zonal wavenumber, and m is the meridional mode number. Thus, long first baroclinic, first meridional, mode Rossby waves propagate westward at approximately $\frac{c_e}{3}$ or around 0.8–1.0 m s^{-1} in the Indian Ocean.

Kelvin waves can also propagate along coastal waveguides, with the coastline to the right (left) of the wave in the northern (southern) hemisphere. Coastal Kelvin waves can be

generated by local wind stress forcing or by equatorial waves incident on a meridionally-oriented coastal boundary. However, the effect of sloping coastal bathymetry is to produce a coastally trapped wave which combines the properties of Kelvin waves and barotropic shelf waves, with modified phase speed and increased dispersion (Huthnance, 1975; Brink, 1982, 1991).

The Madden-Julian Oscillation (MJO) is the dominant atmospheric mode of intraseasonal variability in the tropics (Madden and Julian, 1971, 1972). It is associated with convective, rainfall and wind variability with a periodicity of around 30–60 days, although it is only quasi-periodic and thus has a broadband spectral signal extending as far as 100 days (Salby and Hendon, 1994). See Chapter 1, Zhang (2005) and Lau and Waliser (2005) for a full review of the MJO and its impacts.

The MJO is an important source of surface wind stress variability and thus generates substantial oceanic equatorial wave activity (Chapter 2, Hendon *et al.*, 1998; Han *et al.*, 2001). Observations have linked the MJO-generated oceanic equatorial Kelvin waves to the triggering of ENSO events (McPhaden, 1999). There is also growing evidence of the potential for oceanic equatorial Rossby waves in the Indian Ocean to force variability in the MJO (Chapters 2, 3) and for feedbacks between the two (Han *et al.*, 2001; Han, 2005; Fu, 2007).

The MJO is sporadic, with periods of cyclical activity ("successive" events) interspersed with intervals of relative quiescence. "Primary" Madden-Julian (MJ) events are those that are not preceded by any coherent MJO activity. Here, we follow Matthews (2008) by examining the subset of primary events that begin in the western Indian Ocean, which accounts for the largest portion of such events. Matthews (2008) found no triggers or precursors from the atmospheric dynamics or thermodynamic interaction with the ocean for such events. However, in Chapter 3 we showed, through a combination of case studies and composite analysis, that these events do coincide with the arrival of a downwelling oceanic equatorial Rossby wave in the western Indian Ocean, implying that such waves could act as a trigger. They suggested that the associated warm SST anomalies act to destabilise the atmospheric boundary layer, thus priming the atmosphere for the large scale convection associated with an MJ event. The western Indian Ocean appears to be

a favourable region for such forcing to occur, possibly due to the relatively shallow thermocline (Figure 2.7 in Chapter 2, Xie *et al.*, 2002), higher rates of entrainment cooling (McCreary *et al.*, 1993) and the relatively weak intraseasonal surface heat fluxes here.

This paper examines the dynamical response of the Indian Ocean to the MJO and its potential to couple to the MJO through simulations in a linearised ocean circulation model. A combination of model runs forced by both idealised and realistic surface wind stress forcing are used. The pathways and time scales of the wave propagation are examined using simple idealised wind patches and the effects of stratification, bathymetry and forcing scale are analysed. Model runs with composite forcing are compared with the observational results of Chapter 2 to validate the model performance and investigate further the global dynamical ocean response. The model is then run with observed winds from the period prior to a case study primary event on 24 September 2004. Comparison with observations from that case study allows the key atmospheric forcing events to be identified and their relative importance to be tested. Thus we identify the time scales that are important for this primary MJ event triggering mechanism.

5.4 Observational Data and Model Forcing

The surface wind stress data used in this study are calculated using daily global 10 m wind velocities $\mathbf{v}$ from the European Centre for Medium-range Weather Forecasts (ECMWF) Era-Interim data set (Dee *et al.*, 2011). For compositing relative to the MJO, the period of 1 January 1990 to 31 December 2008 is used. The wind stress τ is then approximated using the standard bulk formula $\tau = \rho C_D |\mathbf{v}| \mathbf{v}$, with the air density $\rho = 1.23$ kg m^{-3} and the drag coefficient $C_D = 1.5 \times 10^{-3}$. This is calculated separately for the zonal and meridional components of the wind field and then spatially interpolated using cubic splines onto the $1/3^\circ$ grid used in the ocean model.

The SSH anomalies used in this study are from the merged TOPEX/Poseidon-Earth Remote Sensing (T/P-ERS) satellite altimetry product (Fu *et al.*, 1994; Ducet *et al.*, 2000; Le Traon *et al.*, 2001). Weekly data on a 0.25° grid were obtained for the period from 14 October 1992 to 23 January 2008, and then interpolated to daily values using cubic splines. SST data from the Tropical Microwave Imaging (TMI) satellite (Kummerow *et al.*, 2000; Gentemann *et al.*, 2004) were extracted from 1 January 1998 to 17

December 2008. The data are available as daily fields of the 3-day running-mean SST at 0.25° resolution. Outgoing long-wave radiation (OLR) is used as a proxy for tropical deep convective precipitation. The OLR data for this study were obtained as 2.5° resolution gridded daily output from the optimally-interpolated Liebmann and Smith (1996) data set. For comparison with the subsurface variability in the model, we use density data from the ECCO-GODAE ocean state estimate (Estimating the Circulation and Climate of the Ocean-Global Ocean Data Assimilation Experiment; Wunsch and Heimbach, 2007), which we treat as "observations" in the same sense as an atmospheric reanalysis product.

To construct composites of observational fields for surface forcing or comparison with model output, we use the eight phases of the MJO as defined by the Wheeler-Hendon index (Wheeler and Hendon, 2004). Phase 1 corresponds to minimum convection over the Maritime Continent and the initiation of active convective anomalies in the western Indian Ocean. These anomalies move eastwards in each successive phase; by phase 4 the positive convective anomalies overlie the Maritime Continent while the suppressed convection has propagated into the western Pacific. A new region of suppressed convection originates in the western Indian Ocean at phase 5; phases 5–8 are thus equivalent to phases 1–4 with anomalies of the opposite sign.

The linear trend, mean and first three harmonics of the annual cycle were removed point-wise from each data set to produce detrended anomaly fields, which were then bandpass-filtered using a 20-200 day Lanczos filter. The use of such a broadband filter is motivated by its ability to exclude low-frequency climate signals as well as high-frequency noise while better retaining the MJO signal and the distinction between individual MJ events than a narrower filter window (Matthews, 2000). The filter uses 241 symmetric weights, meaning that 120 days of data are lost at each end of the data set. All data sets were further truncated so that an integer number of calendar years are retained, thus avoiding seasonal bias. To investigate the oceanic response to the MJO, composites are created separately for each MJO phase, using all days within that phase when the amplitude of the Wheeler-Hendon index exceeds an arbitrary threshold value of 1.5, along with counter-clockwise rotation in the Wheeler-Hendon phase space to ensure eastwards propagation. The threshold value was chosen to select the stronger MJO events (whose impact on the ocean should be stronger and more coherent), as opposed to the threshold

value of 1 chosen by Wheeler and Hendon (2004).

5.5 Model Description and Setup

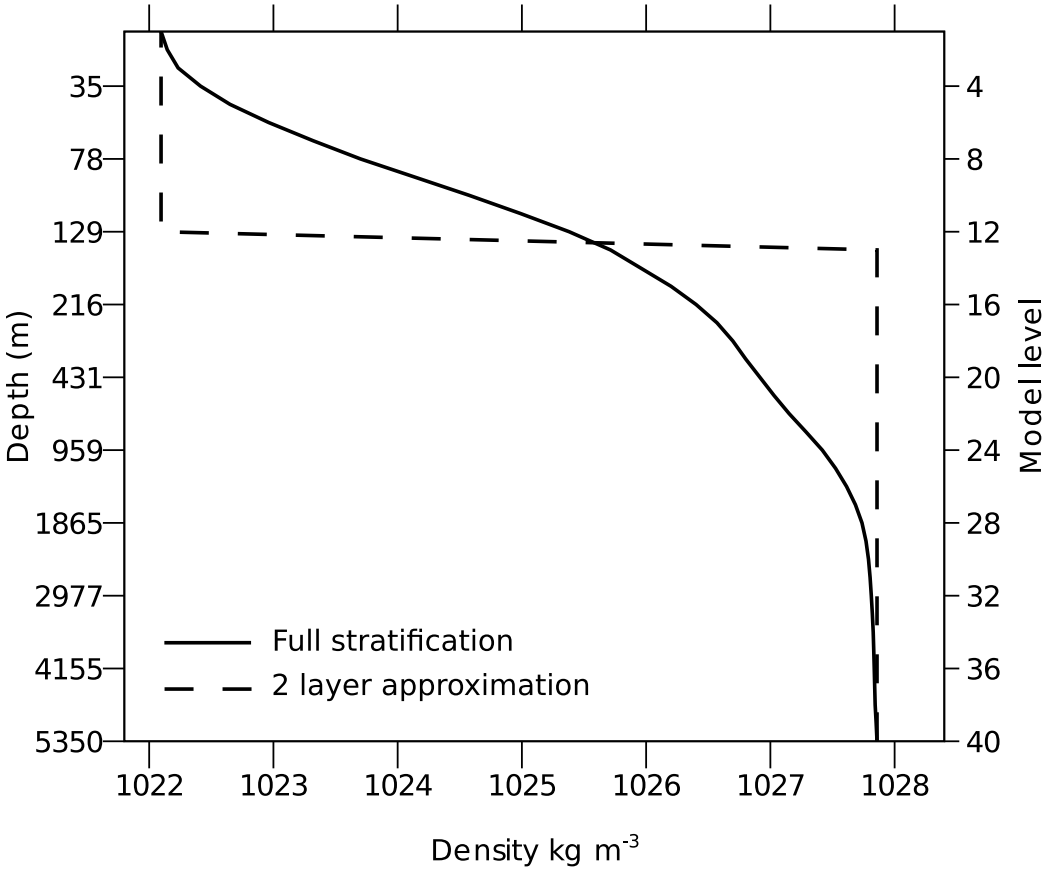

Figure 5.1: Potential density profiles used as the model initial conditions. Solid line: default 40 level density profile, calculated from Conkright *et al.* (2002); Dashed line: two-layer density configuration.

The ocean model used for this study is a linearised version of the general circulation model described by Webb (1996). For a full description of the model, see Chapter 4. The model is configured quasi-globally (the Arctic and the Nordic Seas north of 67° N are omitted), with a horizontal resolution of $1/3^\circ \times 1/3^\circ$ and 40 uneven levels in the vertical that vary smoothly from 10 m thickness at the sea surface to 300 m thickness at depth. The mean vertical potential density profile, $\bar{\rho}$, is taken from the Indian Ocean, calculated from the World Ocean Database 2001 (Conkright *et al.*, 2002) over 10°N–10°S, 60–90°E (Figure 5.1). The model can also be configured with only two density layers, where the upper 12 model layers are given the surface potential density (1022.1 kg m^{-3}) and the

remaining 28 layers the deepest layer potential density (1027.8 kg m^{-3}). The bathymetry of the model is shown in Figure 5.2, along with key geographical regions for this study and the pathway for the Indonesian Throughflow (ITF).

5.6 Idealised westerly wind burst forcing experiments

5.6.1 Control run

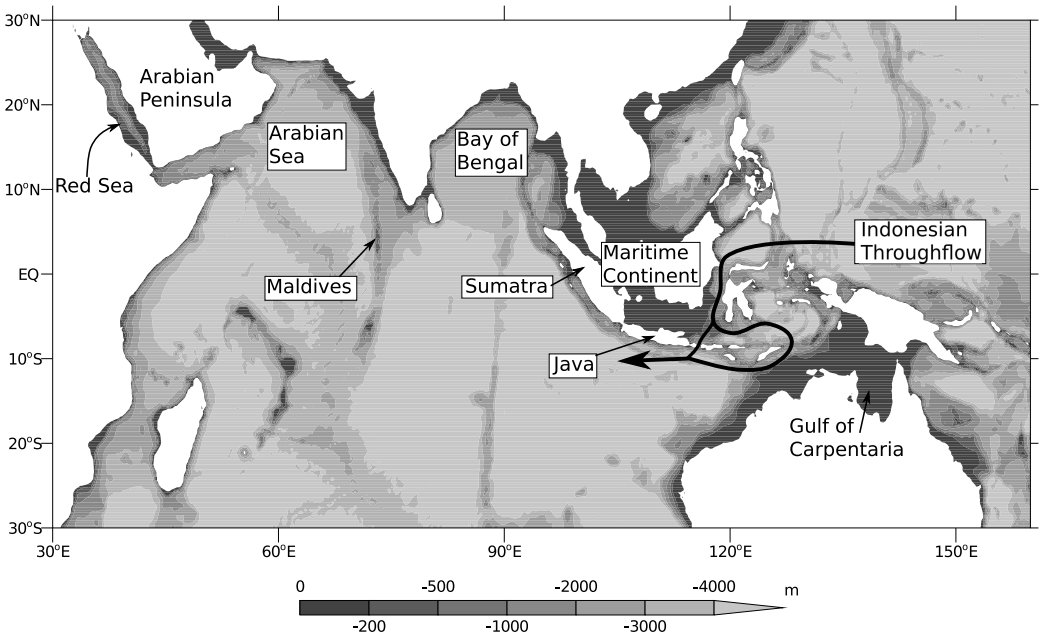

Figure 5.2: Model bathymetry at 1/3° resolution (depth shaded in m; see legend). Labels refer to regions mentioned in this study.

Several studies have shown the importance of westerly wind bursts (WWBs) in forcing equatorial oceanic Kelvin waves (Giese and Harrison, 1990; McPhaden *et al.*, 1992; Kessler *et al.*, 1995). The MJO is a major source of relatively long-lived WWBs at the same spatial scale as the resulting Kelvin waves, and is thus an effective forcing mechanism (Hendon *et al.*, 1998). Here we idealise this forcing mechanism by applying a Gaussian WWB centred on the equator ($\phi_0 = 0$) at λ_0 =75°E, with a decay scale of 10° in both longitude (W_λ) and latitude (W_ϕ). The wind forcing is applied constantly with a peak westerly magnitude of $\tau_0 = 0.1$ N m^{-2} (corresponding to a windspeed of 7.4 m s^{-1}) while $t \leq$5 days and is zero thereafter. The surface zonal wind stress τ_s^λ is thus given by

$$\tau_s^{\lambda}(\lambda,\phi,t) = \begin{cases} \tau_0 \exp\left\{-\left[\left(\frac{\lambda-\lambda_0}{W_\lambda}\right)^2 + \left(\frac{\phi-\phi_0}{W_\phi}\right)^2\right]\right\} & ;0 \le t \le 5d \\ 0 & ;t > 5d \end{cases}$$

The spatial and temporal scale of this forcing is broadly characteristic of the MJO, as is the peak magnitude (Hendon *et al.*, 1998). This experiment is qualitatively similar to that of McCreary *et al.* (1993), and Valsala (2008) who used a $2\frac{1}{2}$ layer model to examine the response of the Indian Ocean to seasonal to interannual wind anomalies.

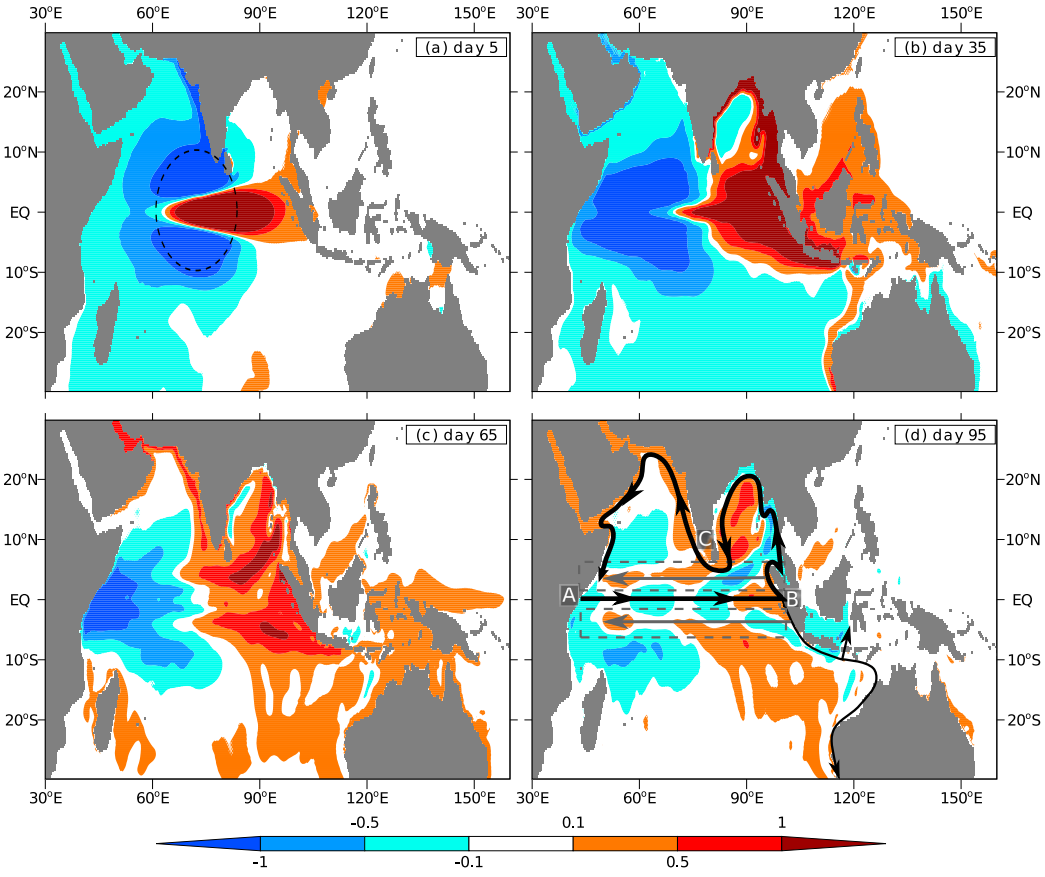

Figure 5.3: SSH anomalies (cm) from the control run of the idealised westerly wind burst experiment. (a) day 5, (b) day 35, (c) day 65, (d) day 95. The equatorial wind patch forcing is indicated schematically by the dashed ellipse in (a). In (d), the equatorial and northern coastal Kelvin-waveguide is shown by the thick black line, the southern coastal waveguides by thin black lines and the equatorial Rossby waveguide by the grey arrows and dashed boxes.

Figure 5.3(a) shows the model SSH anomalies for this control simulation after the initial five days of forcing. The positive SSH anomalies indicate a downwelling equatorial Kelvin wave being forced at 75°E, while the negative off-equatorial SSH anomalies indicate the upwelling Rossby wave response to the wind forcing. By day 35, the Kelvin wave

has propagated eastwards, impinging on the coast of Sumatra where coastal waves are triggered along with reflected downwelling Rossby waves (Figure 5.3(b)). The coastally trapped waves propagate both northwards and southwards, with some of the energy from the latter portion propagating into the Maritime Continent. This energy spreads in all directions, with coastal wave signals propagating around the island coastlines (for example, the positive SSH anomalies along the east coast of Java and Sumatra and then along the west coast of Borneo) and through the various channels. The surface wave signal is not apparently dependent on channel depth and is capable of propagating through channels with a maximum depth of less than 20 m, such as between Borneo and Sumatra. Note that the vertical resolution is around 10 m in the surface layers of the model, so such waves will be imperfectly resolved in such shallow depths.

The subsequent westward propagation of the reflected Rossby wave along the off-equatorial waveguide can be seen in the transition from day 35 to 65 (Figure 5.3(b) to 5.3(c)), and is similar to that observed (Chapter 2, Oliver and Thompson, 2010). At the same time, the upwelling Rossby waves (negative SSH anomalies) have reached the coast of Africa and have begun to reflect into an upwelling equatorial Kelvin wave. The coastally trapped waves propagating along the northern coastal waveguide have circumnavigated the Bay of Bengal and the Arabian Sea, with the westernmost positive SSH anomalies reaching the southern coast of the Arabian Peninsula, as seen in models (Valsala, 2008) and observations (Chapter 2, Oliver and Thompson, 2010). The downwelling coastal wave which propagated southwards along the west coast of Australia has generated westward-propagating Rossby waves in the southern Indian Ocean while the anomalies that propagated through the Maritime Continent have formed a downwelling equatorial Kelvin wave in the Pacific (positive SSH anomalies at 140–160°E on the equator).

Figure 5.3(d) shows the eventual SSH anomalies at 95 days along with the propagation paths of the various wave responses. The thick black arrow shows the equatorial Kelvin waveguide and subsequently the northern coastal waveguide, emphasised because this waveguide retains energy within the tropical Indian Ocean. The thin black lines show the southern coastal waveguide including the path through the Lombok Straits into the Maritime Continent. The grey arrows and dashed boxes show the off-equatorial Rossby waveguide. The arrival of the downwelling equatorial Rossby wave in the western Indian

Ocean can be seen in this figure (positive off-equatorial SSH anomalies at 45–60°E). Coastal Kelvin waves have propagated all the way around the northern coastal waveguide (shown by the thick black arrow) to arrive in the western Indian Ocean at the same time as the equatorial Rossby wave. Once they reach the equatorial region they may contribute to and reinforce the positive SSH anomalies there at around 100 days after the initial wind forcing; we return to this question later. The propagation and timing of both the equatorial Rossby and coastally trapped waves agrees well with observational composites of the free wave response to MJO forcing (Chapter 2).

5.6.2 Sensitivity to latitudinal width of westerly wind forcing

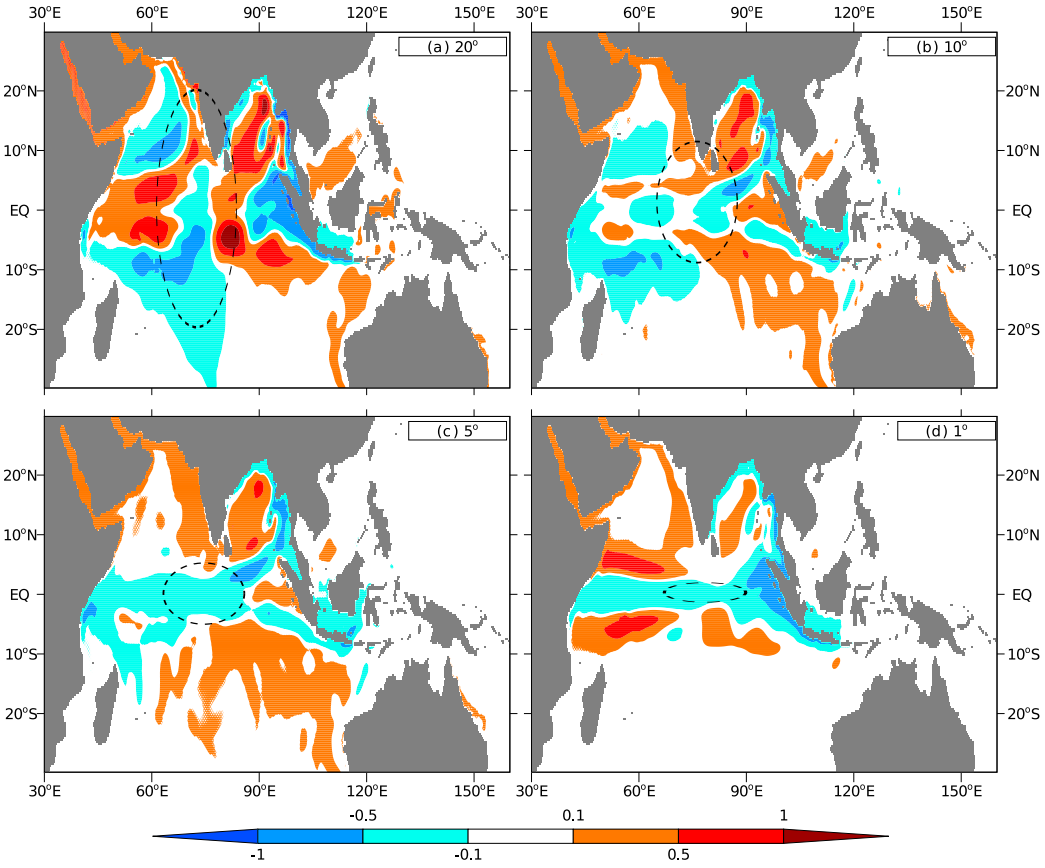

Figure 5.4: SSH anomalies (cm) at day 95 for idealised westerly wind burst integrations with differing latitudinal decay scales of the initial wind patch forcing, shown schematically by the dashed ellipses. (a) 20°, (b) control run; 10°, (c) 5°, (d) 1°.

The sensitivity of the ocean response to the latitudinal Gaussian decay scale (W_ϕ) of the wind patch is examined. Four experiments were carried out, with latitudinal decay scales of 20°, 10° (the control run), 5° and 1° (Figure 5.4). The peak amplitude τ_0 is

the same for all four simulations (0.1 N m^{-2}), hence the wider wind bursts will input more total energy to the ocean, as well as projecting differently onto the equatorial wave meridional modes. As would be expected, there are larger SSH signals away from the equator in the wider wind burst simulations, leading to stronger variability in the Bay of Bengal and the Arabian sea. However, in the equatorial waveguide the sign of the SSH anomalies changes between the simulations, with positive anomalies in the western Indian Ocean in the 20° experiment but predominantly negative SSH anomalies in the same region for the 1° and 5° simulations. The key result is therefore that the latitudinal decay scale of the westerly wind burst can alter not just the magnitude, but also the sign of the resulting equatorial anomalies 95 days later.

The relative strength of the various baroclinic modes (with their different vertical structures and zonal propagation speeds) is also different between the simulations. Within the equatorial waveguide, there are strong positive anomalies at 40–70°E and 80–90°E clearly separated zonally by negative anomalies at 70–80°E in the 20° experiment (Figure 5.4(a)), while narrower wind bursts lead to much less distinction and separation between the modes (zonally uniform negative near-equatorial anomalies in the 5° and 1° experiments). It therefore appears that varying the latitudinal decay scale of the wind forcing leads to a different combination of baroclinic and meridional modes in the model and subsequently a different equatorial SSH signal 95 days after the initial forcing. The implication is that a westerly wind burst at the equator needs to have a latitudinal decay scale greater than 5° latitude in order for the ocean forcing mechanism postulated in Chapter 2 to be important.

5.6.3 Sensitivity to stratification and bathymetry

We now construct simulations with the same wind forcing as the control run but with varying bathymetry and stratification to examine the interaction between Kelvin and shelf wave modes along the coastal waveguide. The bathymetry is either the default model bathymetry used in the control run (see Figure 5.1) or a "flat" bathymetry, set to zero where shallower than 200 m and 4000 m elsewhere. The stratification is either the same as the control, or a two-layer stratification comprising the surface potential density ($\rho_1 =$ 1022.1 kg m^{-3}) in the top 12 model levels ($\sim$200 m) and the bottom layer potential

density ($\rho_2 = 1027.8$ kg m^{-3}) in the lower 28 model levels (Figure 5.1). For the two-layer configuration, we expect the ocean dynamics to consist solely of the barotropic and first baroclinic mode waves, with coastal waves resembling pure Kelvin waves. The propagation speed of the first baroclinic mode Kelvin wave for this configuration is

$$c_e = \sqrt{\frac{(\rho_2 - \rho_1)H_e}{\rho_1 g}} = 2.75 \text{ m s}^{-1},$$

where H_e is the equivalent depth, i.e., the depth of the surface density layer. This phase speed is in good agreement with the calculated first baroclinic mode equatorial Kelvin wave phase speed for the Indian Ocean, which is typically between 2.6 and 2.8 m s^{-1} (Chelton *et al.*, 1998). The estimated Kelvin wave phase speed for the model with full 40-layer stratification and the realistic (control run) bathymetry (Figure 5.2) is around 2.5 m s^{-1}, so we expect the waves to propagate slightly faster in the two-layer configuration. To isolate the Kelvin wave response we construct Hovmöller diagrams along the equatorial Kelvin and coastal waveguides, as shown by the thick black arrow in Figure 5.3(d). Note that some of the reflected Rossby wave propagation can be seen in the equatorial waveguide but this Rossby wave signal is relatively weak.

The first experiment is the most idealised, with just the 2-layer stratification and flat bathymetry (Figure 5.5(a)). The downwelling first baroclinic mode Kelvin wave (positive SSH anomalies) propagates eastward along the equatorial waveguide to the coast of Sumatra (point B) then anticlockwise around the Bay of Bengal to the southern tip of India (point C) and onwards around the Arabian Sea to the Somali coast at the equator (point A). This propagation is very clear and coherent, with minimal energy loss. The arrival of the coastal Kelvin wave in the western Indian Ocean (point A) coincides almost perfectly with that of the reflected Rossby wave which can be seen to a certain extent in the equatorial waveguide (left hand side of Figure 5.5(a)). Interestingly, some of the energy initially associated with the upwelling equatorial Rossby waves escapes into the coastal waveguide near the tip of India (point C) where the coastal waveguide extends into the equatorial domain. There may also be direct forcing of coastal waves here, although the along-shore component of the westerly wind forcing will be small.

After the initial downwelling coastal Kelvin wave there are several wave signals of both signs that can be seen propagating along the coastal waveguide. Some of these can

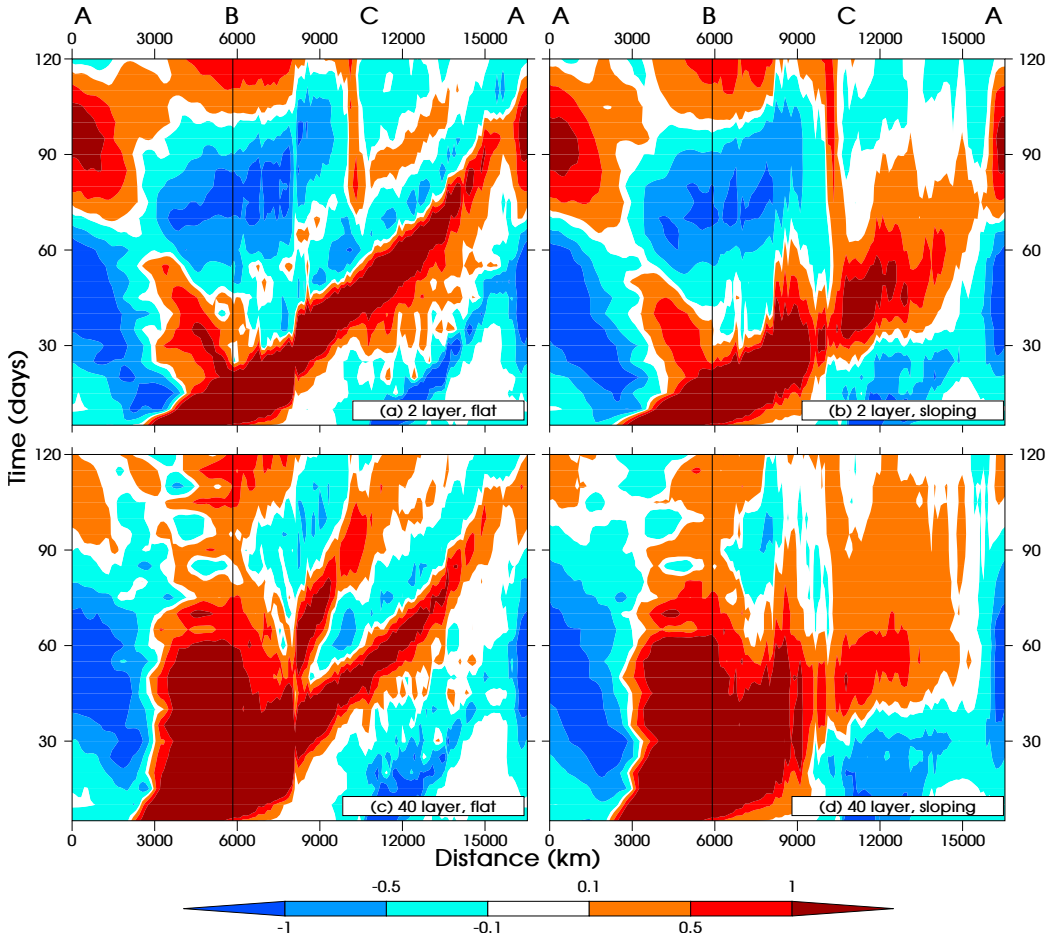

Figure 5.5: Hovmöller diagrams of SSH (cm) along the equatorial and coastal Kelvin-waveguides, as shown by the thick black line in Figure 5.3(d). (a) 2-layer model with flat bathymetry, (b) 2-layer model with sloping bathymetry, (c) full stratification but flat bathymetry, (d) full model with sloping bathymetry. The transition between the equatorial and coastal waveguides is at 5800 km, as shown by the black vertical lines. The letters A, B, C along the top axes correspond to the locations marked in Figure 5.3(d).

be traced back to reflection of equatorial Rossby waves at the western boundary (point A); for example, the negative SSH anomalies here at around day 40 reflect into an upwelling equatorial Kelvin wave which reaches the eastern boundary (point B) around day 75. This signal then propagates coherently around the coastal waveguide as an upwelling equatorial Kelvin wave (negative SSH anomalies) to arrive just past point C at day 120. Similar behaviour can be seen in the downwelling wave signal (positive SSH anomalies) that reaches the western boundary around day 100, subsequently reflecting into an equatorial Kelvin wave that arrives at point B at day 120.

The effect of bathymetry is investigated by replacing the flat bathymetry with realistic sloping bathymetry (c.f. Figure 5.2), while keeping the idealised 2-layer stratification (Figure 5.5(b)). This experiment shows less coherent propagation along the coastal waveguide, whereas the equatorial propagation pattern in the open ocean (left hand portion of the diagrams) is almost identical. The sloping bathymetry will lead to coastal trapped waves with dispersive properties (Huthnance, 1975; Brink, 1982) and thus will attenuate the signal as it propagates around the coastal waveguide. Thus it is unsurprising that the downwelling Kelvin wave signal is relatively spread out and that the signal is weaker by the time it reaches the western Indian Ocean.

The effect of using a realistic 40-layer stratification, but reinstating the idealised flat bathymetry, is shown in Figure 5.5(c). The propagation of energy along the equatorial waveguide is much more spread out than in the idealised 2-layer stratification experiments (Figures 5.5(a,b)), probably due to the partitioning of wave energy between the multiple baroclinic modes that are now allowed by the model. The coastal wave propagation is clearly split into two baroclinic modes with different propagation speeds as shown by their relative slopes on the Hovmöller diagrams. As expected, the wave propagation is slightly slower for this realistic stratification than for the two-layer configuration (Figure 5.5(a,b)), with the peak in positive SSH at the western boundary (point A) occurring 10–20 days later.

Finally, Figure 5.5(d) shows the corresponding Hovmöller diagram for the control simulation (as in Figure 5.3) with both realistic stratification and bathymetry. In this figure, the two factors of energy partitioning between baroclinic modes and increased energy dispersion along the coastal waveguide lead to quite a different picture from Figures 5.5(a–c). The two baroclinic modes evident in Figure 5.5(c) are no longer apparent. The propagation of the positive SSH anomalies along the equatorial waveguide is less coherent compared with Figure 5.5(b), with weaker positive SSH anomalies at the western boundary (point A) at days 100–120. In addition, the coastal wave signal spreads further in time and space than in the other simulations, and becomes insubstantial before arriving in the western Indian Ocean; the weak positive SSH signal on the equator at point A is primarily due to the Rossby wave propagation. Therefore, in the real ocean, it seems likely that the coastal waveguide will be less important than the equatorial Rossby waveguide for

forcing MJO variability in the western Indian Ocean.

The simulations described above summarise the dynamical ocean response to idealised WWBs associated with the MJO in the Indian Ocean. This consists of a combination of equatorial Kelvin and Rossby waves along with coastally trapped waves. Some of the equatorial wave energy escapes along the southern coastal waveguide and into the Maritime Continent, which subsequently leads to weak equatorial Kelvin wave activity in the Pacific. The remainder returns across the Indian Ocean in the form of both equatorial Rossby waves and coastally trapped waves propagating along the northern coastal waveguide. For realistic simulations, the interaction of wave modes along the sloping bathymetry of this coastal waveguide leads to dissipation of this coastal signal before it arrives in the western Indian Ocean. In contrast, equatorial Rossby waves do propagate coherently across the width of the Indian Ocean, and arrive in the western Indian Ocean around 100 days after the initial downwelling Kelvin wave was forced. There are also upwelling wave signals (negative SSH anomalies) that are approximately half a cycle out of phase with the downwelling waves. Multiple meridional and baroclinic wave signals are seen, the distribution of which partly depends upon the latitudinal decay scale of the initial wind forcing. The combination of these wave modes has the potential to critically alter the dynamic ocean state along the equatorial waveguide, and is thus crucial for determining the potential for triggering atmospheric convection and the MJO.

5.7 Realistic composite MJO wind forcing

The key processes in the dynamical ocean response to MJO-like wind forcing have been determined in the idealised experiments of Section 5.6. In this section, the dynamical ocean response to realistic MJO wind forcing is examined. We force the model with composite MJO winds globally (see Section 5.4). These composites consist of eight global fields of the zonal and meridional components of the surface wind (one for each of the eight Wheeler-Hendon MJO phases), which are then interpolated onto a daily time scale by assuming a constant 6 day time interval between phases. This gives a 48-day cycle for the MJO, which is consistent with previous definitions of the MJO life-cycle (Madden and Julian, 1972, 1994). However, this emphasises the cyclical component of the MJO which may not always be appropriate during periods of sporadic behaviour (Matthews, 2008),

and will tend to smear out some of the freely propagating oceanic wave signals generated (Chapter 2). Nevertheless, it is useful as a tool to investigate the key components of the dynamical ocean response to the cyclical MJO. The simulation is run for two full cycles of the MJO (i.e., 96 days), to allow processes occurring over the time scale of multiple MJO cycles to be seen.

5.7.1 Global SSH anomalies

Figure 5.6 shows the SSH anomalies from the second MJO cycle of the simulation (i.e., day 54 to 96) in the left column, with the equivalent composites of observed SSH anomalies in the right hand column. In general the agreement between the model and observations is strikingly good. There is more small-scale noise in the observations, which is to be expected as the model is forced by the relatively low resolution 1° ECMWF winds (compared with the 0.25° SSH data) and does not contain currents and their associated eddies. The propagation of waves around the Indian Ocean in the model shows all the same features as the observations, as does the propagation of SSH anomalies into the Maritime Continent. Several of the features evident in the idealised westerly wind burst experiment (Figure 5.3) are also evident in this composite simulation; the reflection of equatorial waves at the eastern boundary is similar, as is the propagation of waves around the coastal waveguide.

The modelled propagation of Kelvin waves across the equatorial Pacific appears consistent with observations, although the subsequent generation of coastal waves and reflected Rossby waves at the eastern boundary is stronger and more coherent in the model than in observations. There is also evidence in the model of equatorial Kelvin wave activity in the Atlantic, which is somewhat evident but less clear in the observations. A role for the MJO in forcing dynamical variability in the Atlantic has been postulated previously, but not proven (Chapter 2, Foltz and McPhaden, 2004; Han *et al.*, 2008). Our results indicate that at least a portion of this observed variability arises through wind forcing associated with the MJO.

The conclusion of this simulation is that the majority of the observed SSH variability composited relative to the MJO can be explained by the linear dynamical response to surface wind forcing. This implies that other, nonlinear processes are less important,

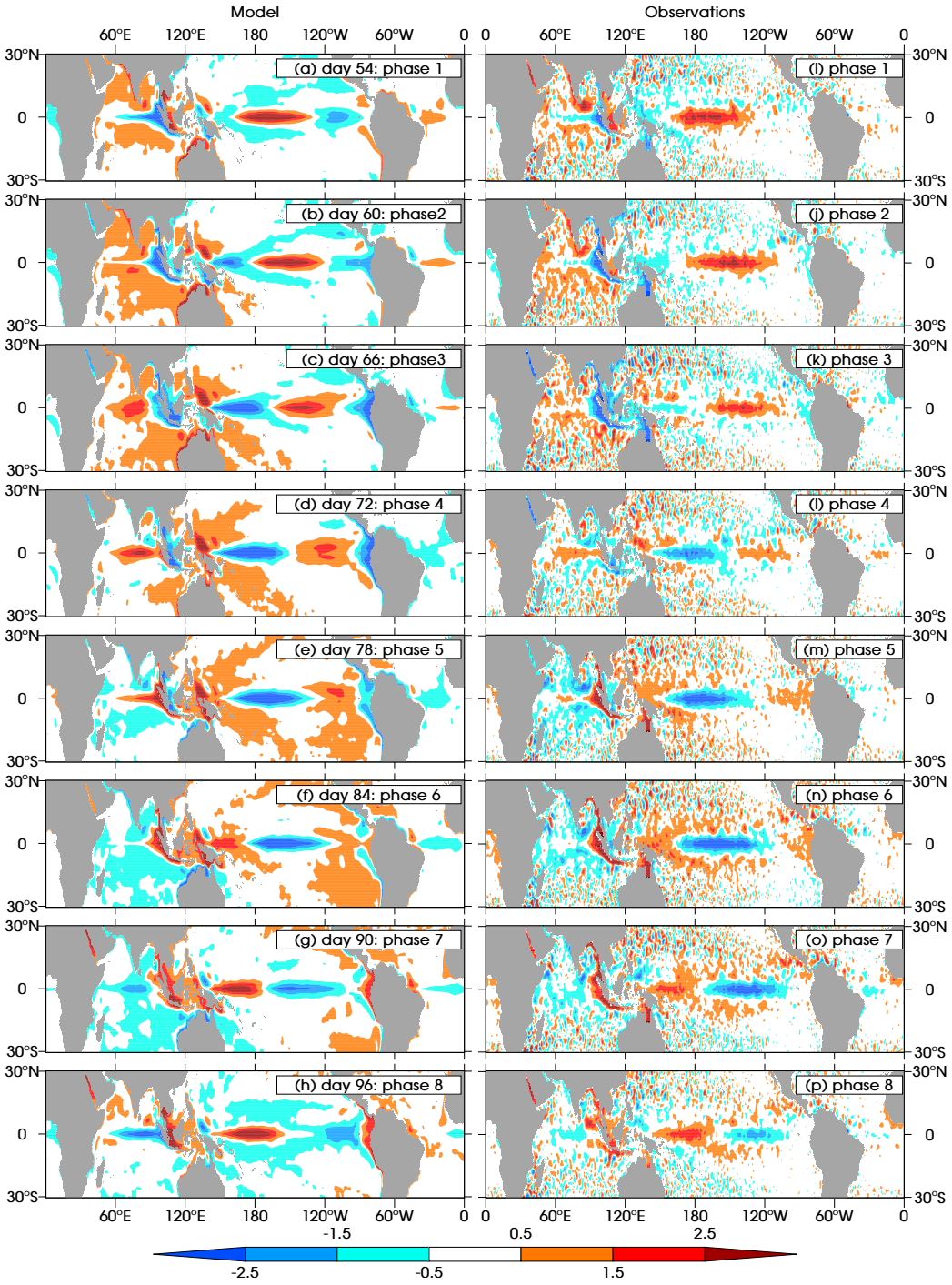

Figure 5.6: SSH anomalies (cm) (a–h) from the model run with cyclical composite surface wind forcing, taken from days 54–96, corresponding to a full MJO cycle. (i–p) Composite SSH anomalies (cm) from satellite altimetry observations for the equivalent MJO phases.

although they may account for the decay in the equatorial Kelvin wave signals as they propagate across the Pacific. There are also large coherent regions of SSH anomalies outside of the equatorial waveguide in the Pacific, in both hemispheres. Additionally, the model simulates the relatively large (>1.5 cm) variability of SSH in the Red Sea noted in Chapter 2. The positive SSH anomalies in phase 7 coincides with strong south-easterly wind anomalies over the preceding two MJO phases (not shown) which will lead to anomalous inflow of water into the Red Sea and thus raise the sea surface; the reverse process accounts for the negative SSH anomalies in phase 3. The variability in the Gulf of Carpentaria found by Oliver and Thompson (2011) and in the observational composites here is not reproduced in quite the same manner; the observed strong positive (negative) SSH anomalies in phases 6–7 (2–3) correspond to a dipole pattern of SSH anomalies in the model. It is not clear what causes this discrepancy, but it may be due to inaccurate representation of the shallow bathymetry of the area in the model, or due to other surface processes not included in this model.

5.8 Realistic primary Madden-Julian event wind forcing experiment

We now move to the question of how ocean dynamics might force primary Madden-Julian (MJ) events. In Chapter 3 we investigated this question using a combination of composite and case study analysis applied to observational data. Here, we will examine the case study of the primary event starting on 24 September 2004 in further detail, by attempting to simulate the oceanic equatorial Rossby wave activity that preceded the triggering of this event. Four experiments are run. The first uses the observed winds for the 150 days previous to the start of the primary MJ event to drive the ocean circulation, i.e., wind forcing from 27 April 2004. The later experiments use the winds for the 120 days, 50 days and 30 days previous to the start of the primary MJ event, respectively. This will allow insight into the key components of the atmospheric forcing necessary to generate this oceanic equatorial Rossby wave.

5.8.1 150 day experiment

Figure 5.7(a) shows the observed SSH and SST anomalies in the off-equatorial Rossby waveguide for the 100 days prior to the initiation of the event of 24 September 2004, until 10 days after the event. Note that day zero of the primary event (i.e., 24 September 2004) is defined to be the maximum principal component amplitude during "phase A" of the MJO, following the definition of Matthews (2008). Therefore, the actual initiation of the convection associated with this MJ event occurs around 10–15 days earlier, as shown by the OLR anomalies (dashed contours in Figure 5.7(b)).

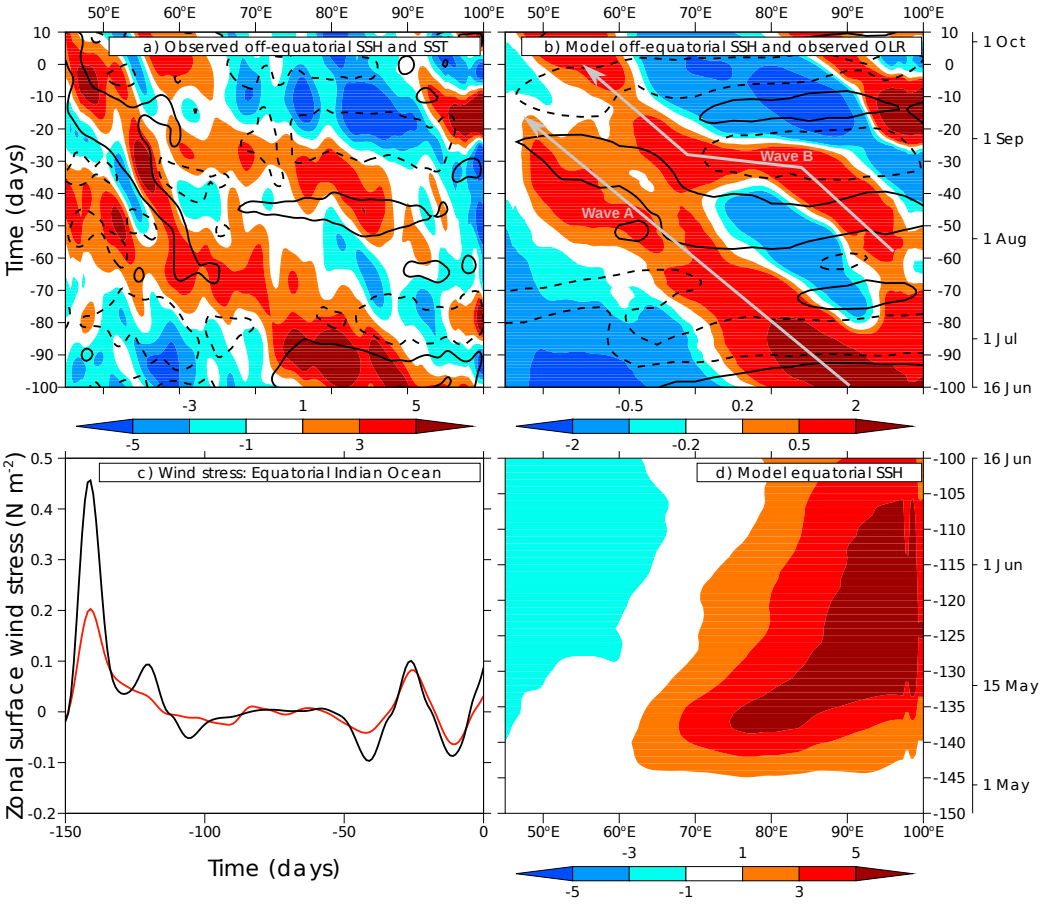

Figure 5.7: (a) Hovmöller diagram of observed off-equatorial SSH (cm; shaded, see legend) and SST anomalies (contoured at ±0.3°C, negative contour dashed) averaged over 2–5°N and 2–5°S for the 100 days preceding the primary event of 24 September 2004. (b) Hovmöller diagram of off-equatorial SSH from the model run forced by observed winds for the 150 days preceding the primary MJ event and observed equatorial (5°S–5°N) OLR anomalies (contoured at ±15 W m^{-2}, negative contour dashed) from day −100 to +10. (c) Surface zonal wind stress anomalies (Nm^{-2}) averaged over 10°N–10°S and: 40–100°E (red line); 70–80°E (black line). (d) Hovmöller diagram of equatorial (2°N–2°S) SSH from the same model run as (b) but for days −150 to −100.

The arrival of the downwelling Rossby wave in the western Indian Ocean can be

clearly seen in Figure 5.7(a), as can the resultant positive SST anomalies, as shown by the diagonally-oriented solid contours in the western Indian Ocean between days -60 and $+10$. The location and timing of the warm SST anomalies agree well with the initiation of the convective anomalies associated with the primary MJ event (dashed contours in (b)). There are likely to be other factors influencing the triggering of this event. For example, there are cold SST anomalies (dashed contours in Figure 5.7(a)) in the eastern Indian Ocean that are associated with suppressed convection in this region that may induce circulation that is favourable for the initiation of convection in the western Indian Ocean. In addition, there is some evidence for a weak convective signal that circumnavigates the globe following the convective activity in the Pacific at lag -50 (not shown) and may also be favourable for the triggering of the event. Nevertheless, given the strength of the dynamically-induced SST anomalies, it seems reasonable to conclude that the arrival of the downwelling Rossby wave has a role in triggering this primary MJ event, following the arguments of Chapters 2 and 3.

When the model is forced using observed winds over the 150 days prior to the primary event of 24 September 2004, it is able to simulate the observed wave propagation with reasonable accuracy (compare SSH anomalies in panels (a) and (b) in Figure 5.7). The magnitude of the SSH anomalies is somewhat smaller in the simulation than in the observations, but the pattern of anomalies agrees well, albeit with less small-scale noise than the observations. These differences may be due to erroneous noise in the observations, to genuine variability not captured in the temporally filtered 1° wind forcing, or possibly to variations in the propagation speed of the Rossby waves between the model and observations. There appear to be two distinct downwelling Rossby wave signals: one (wave A) which is triggered by reflection of the downwelling Kelvin wave arriving at the eastern boundary (Figure 5.7(d)), and a later one (wave B) that begins near the eastern boundary at day -60 and appears to be augmented by local wind forcing around day -40. The combination of these waves appears to generate the broad region of positive SSH anomalies in the western Indian Ocean around days -20 to -10. The latter wave (wave B) continues to propagate westwards after the MJ event is triggered, and is further amplified following the subsequent easterly winds (days $+10$ to $+30$; not shown). However, wave B may be somewhat less important than wave A for triggering the primary

event itself, judging by the location at which convection is triggered (west of 50°E at day −10).

5.8.2 Re-emergence of dynamical ocean anomalies

Analysis of the zonal wind averaged over 10°N–10°S in the Indian Ocean (Figure 5.7(c)) shows that there was a long interval of relatively weak equatorial winds during boreal summer (approximately day −120 to −50), with only a slight increase in variability in the 50 days preceding the primary event. However, around day −140 there was a large westerly wind burst, especially intense in the region of 70–80°E (black line in Figure 5.7(c)). This appears to be linked to the triggering of the downwelling equatorial Kelvin wave shown in Figure 5.7(d). The winds remain westerly for a period of 20 days after this wave is triggered, further intensifying the signal.

There is also an easterly wind burst around day −40 which may be partly responsible for the intensification and rapid westward propagation of wave B around day −40 in Figure 5.7(b). It is likely that the period of relative quiescence between days −120 and day −40 is partly due to the northward displacement of the monsoonal circulation and MJO during boreal summer (Wang and Rui, 1990). The westerly wind burst which triggers the initial equatorial Kelvin wave is thus probably associated with the last major MJO cycle of the boreal spring season (140 days prior to 24 September is 7 May).

A key result is therefore that a westerly wind burst in the central Indian Ocean associated with a strong MJ event can trigger equatorial wave activity in the Indian Ocean that can affect the MJO 140 days (approximately five months) later. This is associated with the "re-emergence" of SST anomalies generated by ocean dynamics forced by wind variability during the preceding boreal spring and subsequently leading to convective anomalies. 140 days is an extraordinary lead time for the MJO, for which predictability is normally limited to around three weeks (Love and Matthews, 2009; Kang and Kim, 2010; Vitart and Molteni, 2010; Rashid *et al.*, 2011). Thus, even the relatively short lead time associated with the easterly wind forcing at day −40 suggests the potential for unprecedented predictability.

5.8.3 Sensitivity to length of wind forcing history

Although we have clearly shown that 150 days of wind forcing simulates the observed wave propagation preceding the primary MJ event of 24 September 2004, it remains an open question whether it is possible to simulate similar dynamics with a shorter period of wind forcing. It is possible that a similar SSH structure could be generated without the westerly wind burst at -140 days. We now turn to this question by examining Hovmöller diagrams of Rossby wave propagation from such model simulations integrated over a shorter period of wind forcing (Figure 5.8). The observed SSH anomalies are reproduced in each panel to facilitate comparison. The run with 150 days of wind forcing (Figure 5.8(a)) shows that the model SSH anomalies agree broadly with the location of the observed anomalies, although the fit is not exact, as discussed above.

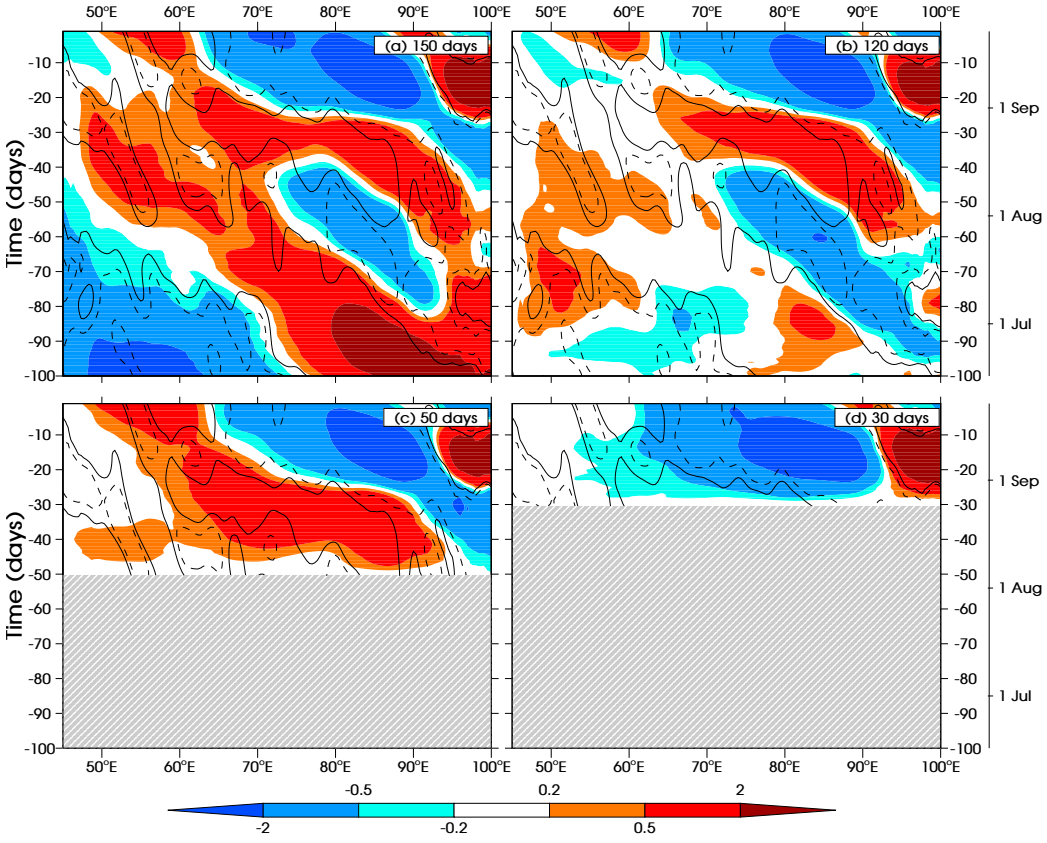

Figure 5.8: Hovmöller diagrams of model SSH (cm; shaded, see legend) and observed SSH anomalies (contoured at ± 1 cm, negative contour dashed) for the 100 days preceding the primary event on 24 September 2004. The model integrations were forced with observed wind stress, and started at (a) 150 days, (b) 120 days, (c) 50 days, (d) 30 days prior to the start of the primary MJ event on 24 September 2004 (day 0).

When the model is forced only with observed winds over the preceding 120 days

(Figure 5.8(b)), there is little if any evidence of the Rossby wave generated by reflection at the western boundary in panel (a). This is unsurprising given that this wave can be traced back to wind forcing that occurred before the 120 day cut-off. There are some positive SSH anomalies along the propagation path of wave A, which may be locally forced, but these do not propagate coherently as a Rossby wave. However, there is evidence of an upwelling Rossby wave which propagates from the eastern Indian Ocean before being largely over-ridden by the broad region of positive SSH anomalies between 60° and 90°E, associated with wave B and forced by the easterly wind anomalies around day −40. The positive SSH anomalies associated with this downwelling wave (wave B) do propagate relatively coherently, but do not create a broad region of positive SSH anomalies between days −20 and −10, in time for triggering the primary event.

Panels (c) and (d) show the results from shorter simulations. For the simulation with 50 days (Figure 5.8(c)), wave B is strongly evident; more so than for the 120 day simulation since the preceding upwelling Rossby wave is not simulated. The SSH anomalies do not agree well with the location and timing of the observed SST anomalies but could still have a role in enhancing the convective anomalies of the primary MJ event. However, from Figure 5.8(d), it is clear that 30 days of wind forcing is not sufficient to generate any positive SSH anomalies locally in the western Indian Ocean. We therefore conclude that the ocean dynamics are not merely a response to wind forcing in the few weeks before the primary event, but rather a response to wind forcing from more than a month before. Furthermore, the role of the westerly wind burst five months previously is confirmed as being important to the triggering of the primary event.

5.8.4 Rossby wave vertical structure

We now analyse the vertical structure of the model Rossby waves in order to investigate the magnitude of the thermocline displacement associated with the SSH perturbations. Figure 5.9 shows depth-longitude sections for the surface 450 m over 45–95°E in both our model and "observations" from the ECCO ocean state estimate (Wunsch and Heimbach, 2007). In both the model and observations, the downwelling wave can be traced in the form of negative density anomalies back to the eastern boundary at day −100. These anomalies are maximum around 100 m depth but extend coherently into the deep ocean

with a slight westward tilt with increasing depth. This tilt implies upward phase propagation and downward energy propagation and has been observed in equatorial Kelvin waves for the Pacific Ocean forced by the MJO (Matthews *et al.*, 2007, 2010). The coherent propagation across the width of the Indian Ocean reinforces the hypothesis that the wave activity can be traced back to reflection of the equatorial Kelvin wave incident on the eastern boundary prior to day -100.

One difference between the model and the observations is in the near-surface density anomalies, especially in days -60 to 0. The model shows a persistent surface layer of positive density anomalies overlying the negative density anomalies associated with the downwelling Rossby wave, while this layer is much more broken in the observations. This is likely to be associated with surface thermodynamic and precipitation processes not included in our simulations, which will act to modify the density of the surface layers. In addition, nonlinear processes and mixing by near-surface currents are not present in the model and may also play a role.

5.9 Discussion

5.9.1 Ocean Dynamics

Our results show that the observed wave propagation can be simulated by a simple ocean model linearised about a resting basic state. This realistic behaviour is evident even from model simulations forced by an idealised Gaussian westerly wind burst on the equator in the Indian Ocean. The subsequent wave propagation shows many of the features identified in previous studies of the dynamics of this ocean basin in response to wind forcing by the MJO (Chapter 2, Oliver and Thompson, 2010). Crucially, the arrival of downwelling oceanic equatorial Rossby waves in the western Indian Ocean around 90 days after the initial wind burst agrees with the findings of Chapter 2 and with hypotheses of coupling between the atmosphere and the ocean dynamics on such time scales (Han *et al.*, 2001; Han, 2005; Fu, 2007). The western Indian Ocean is an important region in which forcing by oceanic equatorial Rossby waves can influence atmospheric convection due to the relatively shallow thermocline, higher rates of entrainment cooling (McCreary *et al.*, 1993) and thus increased correlation between SSH and SST anomalies (Xie *et al.*, 2002). It is

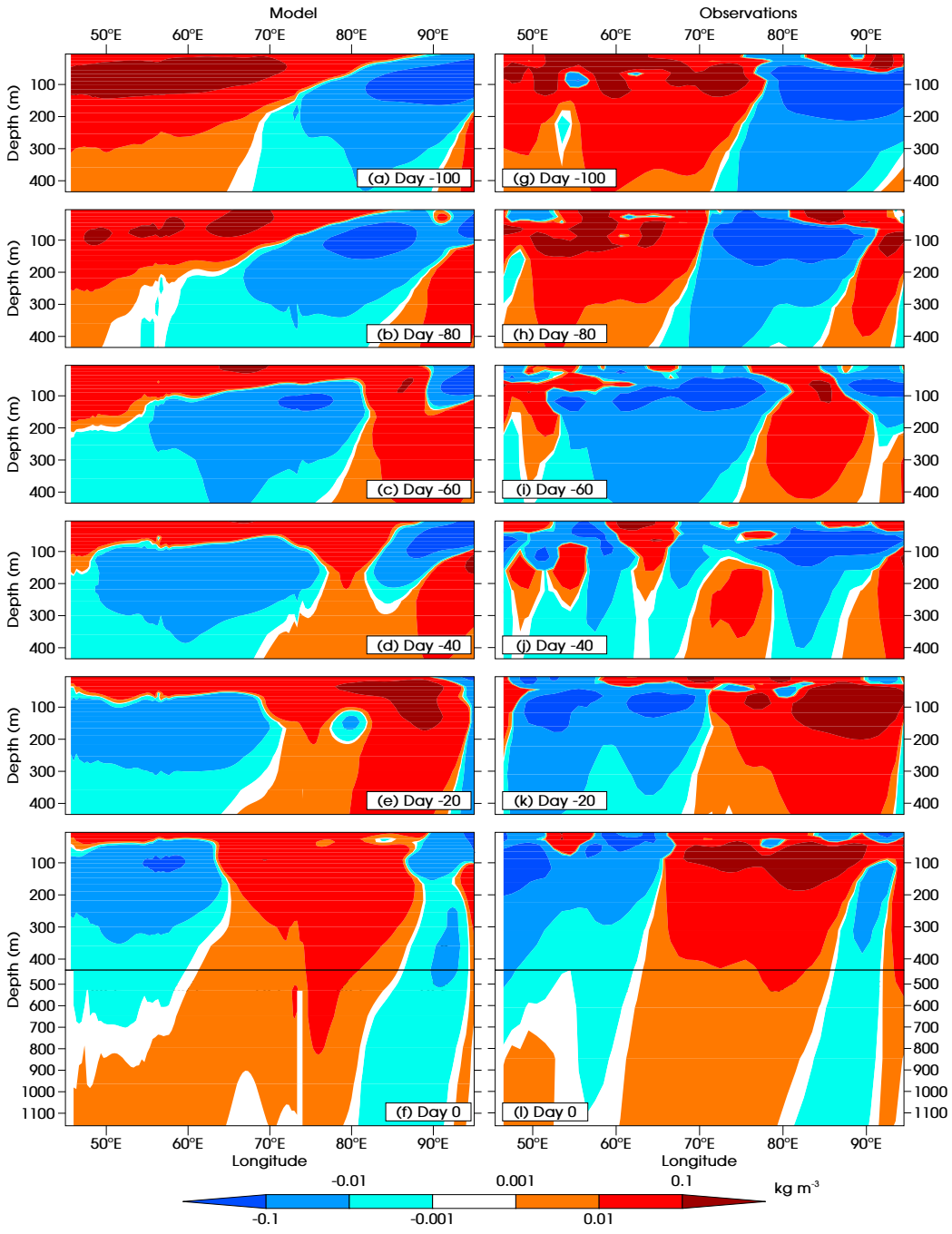

Figure 5.9: Vertical profiles of density anomalies (kg m^{-3}; shaded, see legend) for the 100 days preceding the primary event on 24 September 2004 in: (a–f) the model simulation forced by observed winds over the 150 days prior to the primary event; (g–l) "observations" from the ECCO-GODAE ocean state estimation. (a,g) day −100, (b,h) day −80, (c,i) day −60, (d,j) day −40, (e,k) day −20, (f,l) day 0.

worth noting that the model does not contain the complex equatorial current systems of the Indian Ocean, which would be expected to alter the phase speed of Rossby waves through Doppler shifting and by altering the meridional vorticity gradient through which they propagate (McPhaden and Ripa, 1990). Therefore the location of the waves in time and space may vary between model and observations.

The model reproduces the observed propagation of coastally trapped waves, both southwards along the coasts of Sumatra and Java into the Maritime Continent and northwards around the Bay of Bengal. This latter coastal waveguide continues around the tip of India, where wave energy may escape from the equatorial waveguide or be triggered by near-equatorial winds. Coastally trapped waves continue to propagate around the Arabian seas and arrive in the western Indian Ocean at around the same time as the equatorial Rossby waves. This coincidence in timing led us to hypothesise in Chapter 2 that the propagation of anomalies along the coastal waveguide could contribute to feedbacks onto the MJO. This hypothesis is consistent with the results of a two layer model with flat bathymetry, in which the coastal Kelvin wave arrives at the same time as the equatorial Rossby wave. However, simulations with more realistic stratification and bathymetry suggest that interactions between baroclinic modes and barotropic shelf wave modes lead to higher levels of energy dispersion such that the coastally trapped wave signal never reaches the western Indian Ocean. Therefore we can conclude that it is the oceanic equatorial Rossby wave dynamics that are important for understanding coupling between the MJO and the dynamics of the Indian Ocean.

Another constraint on the potential for feedbacks from the ocean dynamics onto the MJO appears to be the latitudinal decay scale of the westerly wind burst which generates the initial wave activity. In order for the eventual SSH anomalies to be coherent, it appears that the Gaussian westerly wind burst must have a latitudinal decay scale greater than 5° (10° is certainly sufficient). Narrower wind bursts change not just the magnitude but also the sign of the eventual equatorial anomalies, with substantially altered spatial patterns for the SSH anomalies. It is hypothesised that this difference between the simulations is due to different projections of the initial wind forcing onto meridional and baroclinic wave modes. This variation in the dynamic response suggests that atmospheric variability needs to be coherent over a relatively broad latitudinal range, centred on the equator, in

order to effectively force dynamical variability in the equatorial oceans. In addition, the boreal summer MJO, which exhibits less coherent variability around the equator (Wang and Rui, 1990) will probably be less effective in forcing such dynamics.

When the model is forced by realistic composite MJO winds globally, it is able to replicate the observed composite SSH anomalies. This is an important result as it reinforces the notion that the global SSH response to the MJO is a simple product of the linear dynamic response to surface momentum flux; nonlinear and thermodynamic effects are not required and neither is a realistic ocean circulation. We might therefore infer that the interannual variability of the ocean will have a relatively minor effect on the dynamical ocean response to the MJO which will be predominantly a linear addition to this low-frequency variability.

In addition, this model run highlights some intriguing characteristics of the global dynamic ocean response to the MJO. For example, there is evidence of equatorial Kelvin wave propagation in the Atlantic which subsequently can be seen to propagate in both directions along the coast of Africa. Such behaviour has been seen by Polo *et al.* (2008), but has not previously been attributable to the MJO; our results suggest that at least a portion of this can be attributed to a local linear response to wind variability associated with the MJO. The model also simulates substantial SSH variability in the Red Sea, in agreement with observations (Chapter 2) but fails to simulate the observed SSH variability in the Gulf of Carpentaria (Oliver and Thompson, 2011). Such forms of local variability are likely to have a substantial impact on biological productivity due to variations in the upwelling of nutrients. This would build upon existing research that has established a role for the MJO in generating chlorophyll variability through such mechanisms (Waliser *et al.*, 2005; Isoguchi and Kawamura, 2006).

5.9.2 Primary Events

A model simulation with observed winds over the 150 days preceding the primary MJ event of 24 September 2004 reproduces closely the observed SSH variability which has previously been implicated in triggering this primary event (Chapter 3). A westerly wind burst 140 days before the primary event is implicated in generating a downwelling Kelvin wave which subsequently reflects into the first of two Rossby wave signals seen (wave

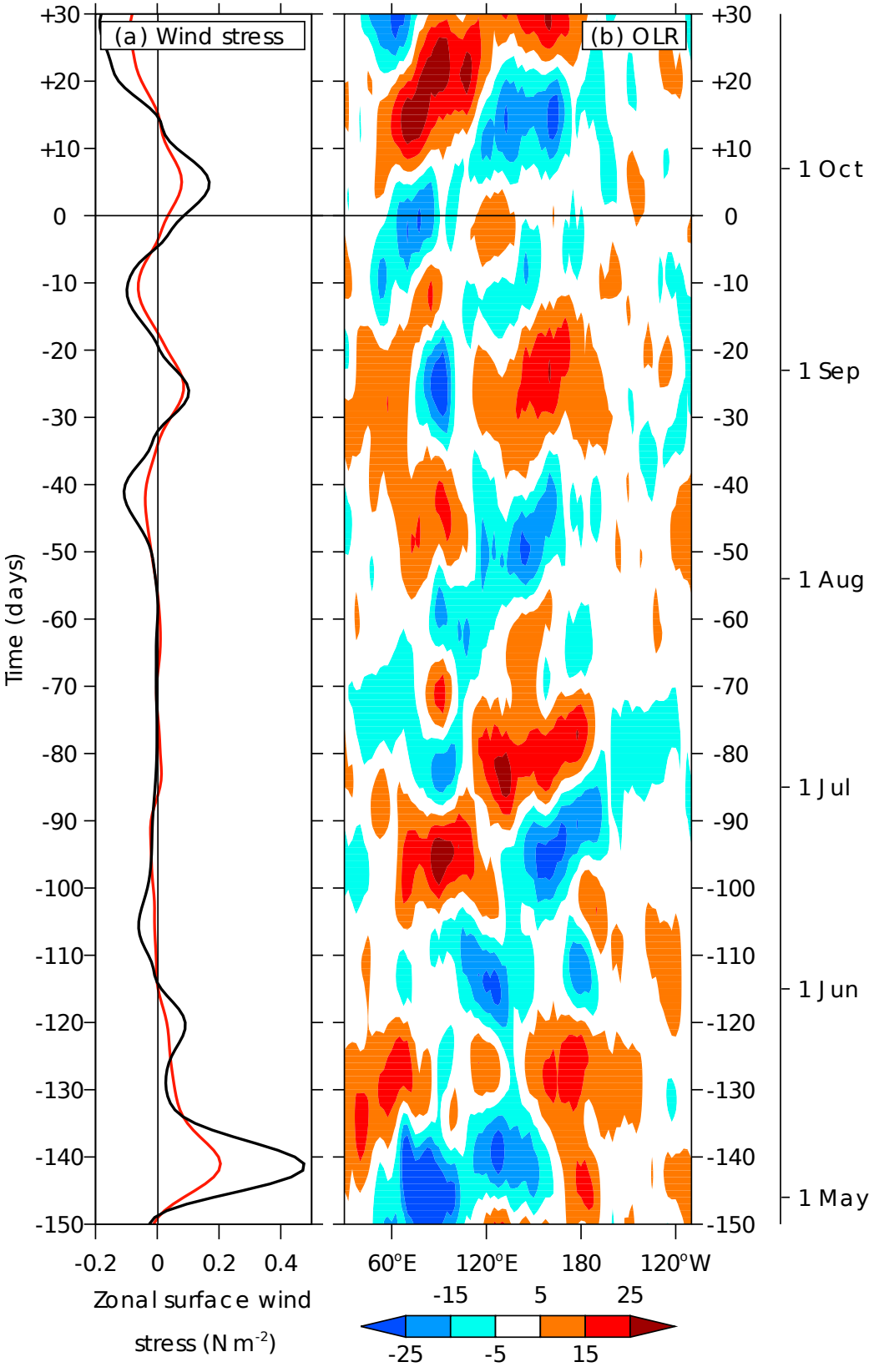

Figure 5.10: (a) as in figure 5.7(c) but rotated by 90°. (b) Hovmöller diagram of OLR anomalies (W m^{-2}; shaded, see legend) averaged over 15°N–15°S for the period from 150 days prior to until 30 days after the primary event on 24 September 2004.

A). This wave propagates westwards to arrive in the western Indian Ocean shortly before the initiation of convection, although there is a slight difference in the propagation speed of this wave between model and observations. Simulations with shorter periods of wind forcing are less successful at replicating the observed dynamics, although 50 days is sufficient to generate the latter portion of the wave activity observed (wave B). From the observations of SST and OLR, it appears that wave A is at least as important as wave B (indeed, probably more so) in generating the warm SST anomalies which prime the atmosphere for convection. The reduced convection in the eastern Indian Ocean that precedes the initiation of the primary event may also be influential through modifications to the atmospheric circulation; these reduced convective anomalies coincide with cold SST anomalies that may be partly driven by the preceding upwelling Rossby wave.

To put these forcing events into context, Figure 5.10 shows the intraseasonal OLR anomalies averaged over 15°N–15°S for the period from 150 days prior to 30 days after the primary event of 24 September 2004. The westerly wind burst around day -140 can be clearly linked to intense convective activity over the eastern Indian Ocean region (negative OLR values below -25 W m^{-2} between 65–100°E in early May). This is one of the last strong cycles of MJO activity of the boreal spring season, which is followed by relatively weak and incoherent anomalies during the summer season when convection shifts north of the equator (Wang and Rui, 1990). The MJO becomes organised again in a cyclical sense in late September and early October. This re-invigoration of the MJO begins with the primary event on 24 September, which coincides with the re-emergence of ocean anomalies forced by a westerly wind burst before the summer period. There may also be a role for atmospheric variability, including the component of the MJO that exists to the north of the equator over the summer months, but it seems likely that the ocean dynamics at least play a role in triggering the primary event in question.

The key conclusion of this chapter is therefore that the ocean dynamics act to integrate intraseasonal wind forcing over as much as five months and can subsequently trigger a primary MJ event. In the case study of 24 September 2004, the wave activity is triggered by the last major episode of MJO variability before the summer season. The equatorial waves propagate almost freely back and forth across the Indian Ocean, before being reinforced by a second Rossby wave, triggered by easterly wind anomalies around 40 days prior to

the primary event. Thus an MJ event is able to influence another one four cycles later. Although we have only presented results from one case study, composite analysis suggests that downwelling Rossby waves are consistently important for triggering primary MJ events (Chapter 3). Therefore, although the specifics will vary, it is likely that interaction between intraseasonal atmospheric variability and the ocean dynamics, with their differing time scales, is at least partly responsible for the sporadic nature of the MJO.

This potential for coupling between the intraseasonal atmospheric variability and dynamic ocean processes occurring at a longer time scale also brings the potential for forecasting MJO activity at long lead times. Given that current state-of-the art forecasts of the MJO only exhibit skill up to 20–25 days (Love and Matthews, 2009; Rashid *et al.*, 2011), a process which is predictable over 140 days is exceptional. The degree to which the ocean dynamics can be used to forecast the MJO remains to be tested, but it is likely to be strongest during periods of reduced MJO activity, when forecast skill is low (Jones *et al.*, 2004). These results emphasise the importance of monitoring the equatorial Indian Ocean using combinations of moored buoys and ARGO floats, in combination with satellite data, to potentially facilitate such predictions.

5.10 Acknowledgments

The altimeter products were produced by Ssalto/Duacs and distributed by Aviso with support from Cnes and are available at `www.aviso.oceanobs.com/`. The TMI SST data were obtained from the SSM/I website at `www.ssmi.com/tmi/`. The EMCWF surface wind data were obtained through the British Atmospheric Data Centre (BADC) and from the ECMWF website at `data-portal.ecmwf.int/data/d/interim_daily`. The interpolated OLR data were obtained from the NOAA/OAR/ESRL PSD web site at `www.cdc.noaa.gov/`. Data from the ECCO-GODAE project were obtained through the ftp site `www.ecco-group.org/`. The Wheeler-Hendon index was obtained from `http://www.bom.gov.au/`.

Chapter 6

Conclusions

6.1 Summary

Despite four decades of study, the MJO remains incompletely understood. It is the dominant source of variability in the tropical atmosphere-ocean system (Madden and Julian, 1994; Lau and Waliser, 2005; Zhang, 2005) and generates anomalous circulation and rainfall on a global scale (Matthews *et al.*, 2004; Donald *et al.*, 2006). As such, it is very important that we improve our understanding of it, along with our ability to predict it. However, there is a large gap in understanding, particularly of the potential interaction with ocean dynamics. It is known that MJO-induced equatorial ocean waves can trigger El Niño events (Kessler *et al.*, 1995; McPhaden, 1999; Zavala-Garay *et al.*, 2005), but there is little understanding of how these same ocean dynamics might influence the MJO itself.

To elucidate the role of the dynamic ocean response to the MJO, and to determine the degree to which this can be seen as a component of the MJO, we have conducted studies to answer a number of sub-questions within this larger remit. Not all of these were apparent on beginning the PhD, but instead became evident as the answers to the initial questions threw light on other questions in turn. The fundamental question behind Chapter 3 was conceived following the results of Chapter 2, and the motivation for the modelling studies in Chapter 5 was inspired by the results of the previous two chapters.

The first goal of this thesis was to quantify the dynamic ocean response to the MJO, in a concise and coherent manner. Prior to this there had been no attempts to define the generic response of the ocean dynamics to the MJO throughout its life cycle. The details,

mechanism and implications of this response were also in need of investigation. The second question was to understand how the ocean dynamics might then feed back onto the MJO, and to investigate any resonance that might occur between the two systems. This was partly motivated by previous work that had shown the existence of resonant modes within the Indian Ocean at time scales similar to that of the MJO (Han *et al.*, 1999, 2001; Han, 2005; Fu, 2007). The results of this work motivated the assessment of the potential for the ocean dynamics to trigger MJ events, especially primary MJ events that are not preceded by any other triggers. Finally, it was necessary to understand what constraints there might be on this interaction, feedback or forcing by the ocean, either due to the ocean dynamics, the atmospheric forcing or the basic state against which the variability is manifest.

6.2 Progress

Quantification of the dynamical ocean response to the MJO was achieved observationally in Chapter 2, with further refinements made by the theoretical model studies of Chapter 5. From these results, it can be concluded that there is a large, long lived and temporally coherent response. This includes equatorial wave activity in all ocean basins, dynamic variability in the Red Sea and the Gulf of Carpentaria, and extra-tropical responses. In addition, there is significant coastal wave activity in the Indian Ocean, in the Maritime Continent and (to a lesser extent) along the coasts of the Americas and Africa. These constitute far-reaching oceanographic impacts, with implications for the Indonesian Throughflow, equatorial and coastal current systems, upwelling in shelf seas and will in turn influence ocean biology and chemistry. The deep ocean response seen by Matthews *et al.* (2007, 2010) has also been verified by the results of Chapter 5. Many of these oceanographic responses deserve further study in their own right, such as analysis of the response in the Red Sea, investigation of the ITF variability in response to the MJO and the influence of the dynamic ocean component of the MJO for biology.

The potential for feedbacks from the dynamical ocean response to the MJO has been considered throughout each of the chapters. Chapter 2 considered this as a resonant coupling between the MJO (with a nominal time scale of $\sim$45 days) and the ocean dynamics (with a nominal time scale of $\sim$90 days, or exactly double the nominal time scale of the

MJO). This led to the concept that the ocean dynamics feed back onto the next-but-one MJ event, supported by composites of SSH compared with composites of SSH, surface heat fluxes and OLR. This conceptual framework sets the ocean dynamics as a key component of the MJO, that will enhance its low-frequency variability. The shoaling thermocline in the western Indian Ocean provides a constraint on the location of this feedback mechanism and may help explain why the majority of MJ events form here (Matthews, 2008). However, it is necessary to invoke chaotic interactions between the many feedback or initiation mechanisms for the MJO to explain why the dynamical ocean component is not more strongly resonant, or more consistently evident as a triggering mechanism. Assessing the degree to which these various mechanisms are important is a key question for future research.

We now turn to the potential for the ocean dynamics to trigger primary MJ events. Within this conceptual framework it is preferable to view the ocean dynamics as evolving freely after triggering by some unknown atmospheric forcing at some time previously. The source of the waves is not important here, only the impact that the waves have on the subsequent initiation (or otherwise) of MJO activity. This was assessed in Chapter 3 using the methodology of Matthews (2008) to distinguish between 'primary' and 'successive' MJ events. Analysis of primary events provides a clean framework in which to assess the impact of the ocean dynamics on the MJO, since it allows observed oceanic anomalies to be robustly attributed to cause rather than effect (assuming the processes are not merely coincidental). This is in contrast to composites of cyclical MJO activity when the effects from one event cannot be separated from the causes of the next. Applying this methodology to the ocean dynamics shows that equatorial ocean Rossby waves appear to be a consistent and important trigger for such primary events. There is some, but relatively little, evidence of equatorial ocean Rossby waves triggering successive events, which emphasises that the ocean dynamics are more influential for the MJO when other atmospheric triggering mechanisms are not active. The results of Chapter 3 are also consistent with the concept that the ocean dynamics enhance the low-frequency tail of the MJO, since the primary events have a lower frequency spectral signature by definition. This will also act as a mechanism to enhance the sporadic behaviour of the MJO. The implications of this chapter are all the more important due to the lack of other, atmospheric

triggers for primary MJ events; they were difficult to explain prior to the discovery of the ocean dynamics as a triggering mechanism (Matthews, 2008). The results of Chapter 5 show how these waves can originate from previous MJO activity many months previously, which suggests that they are indeed a component of the MJO, albeit perhaps in a different and more complex sense than that suggested by the results of Chapter 2. The modelling studies of Chapter 5 also highlight how the waves, and thus the MJO behaviour, is potentially predictable over time scales of around 140 days, which is exceptional in the context of the MJO. This also provides some hope for forecasting the MJO when it is not already active, which has previously been a particularly difficult challenge (Jones *et al.*, 2000).

The final question was to understand further the details of the dynamical ocean processes that are important to the interactions outlined above, and thus any constraints on the strength of this feedback from the ocean dynamics. This was achieved by the idealised modelling experiments described in Chapter 5. The first result of this was to support the notion that a westerly wind burst can lead to the propagation of Kelvin and Rossby waves coherently such that the reflected Rossby wave arrives back in the western Indian Ocean around 90 days after the initial Kelvin wave was forced, as postulated in Chapter 2. This supports the concept that reflection at the eastern boundary of the Indian Ocean is important to the feedback, as opposed to direct forcing of Rossby waves by easterly surface wind stress being the primary mechanism. The relative importance of this reflection as opposed to the propagation of coastal waves around the northern boundary of the Indian Ocean has also been established, since realistic coastal topography modifies the wave properties such that they become dispersive and decay to insubstantial amplitudes before reaching the western Indian Ocean. The latitudinal width of the wind forcing has also been investigated and found to have profound implications for the feedback; modifying this width changes not just the magnitude but the sign of the eventual SSH signal in the western Indian Ocean. This could point to the MJO as a particularly suitable forcing mechanism due to its comparatively broad spatial scale.

6.3 Limitations

The limitations of the methods applied throughout this thesis are mostly due to the relatively short period for which the data are available (the most important being the SSH

data as an indicator of the equatorial waves, for which 20 years of data are now available), compared with the time scale of the processes investigated. This leads to fairly small sample sizes and limits the confidence in the results somewhat, especially for primary events where the number of samples is less than 20. The compositing technique used throughout is well suited to this sort of study since it does not assume linearity between the response at different phases of the MJO. However, the different time intervals between phases of the MJO does lead to some conflation of processes occurring with different time scales. This has been overcome by using time-lagged composites to more clearly reflect the time evolution of composited processes.

The SSH data set used is generally accurate, with the biggest errors arising out of aliasing tidal signals; this is especially problematic in regions with large tidal amplitudes, so the results should be interpreted with caution near the coastlines (Fu *et al.*, 1994; Le Traon *et al.*, 1994; Schlax and Chelton, 1994). The SST data from the TRMM Microwave Imager (TMI) have been found to have smaller biases than the more commonly used infrared SST data (Stammer *et al.*, 2003) and have better variance (Harrison and Vecchi, 2001; Klingaman *et al.*, 2008), partly due to the better spatial coverage of this data since microwaves are not absorbed by clouds. Nevertheless, there are still concerning biases and uncertainties in the data set (Ricciardulli and Wentz, 2004). In addition, there are missing data points due to heavy rainfall, which were filled in through temporal interpolation, potentially leading to small errors.

The other data used were primarily from reanalysis products; these are generally reliable, with the caveat that where observations are sparse, the data are not much better than model output. This is concerning over the ocean regions, but the use of satellite data and surface ocean observations from buoys, ships and Argo floats have improved the situation somewhat (Dee *et al.*, 2011). Of particular concern in atmospheric reanalysis products are the hydrological cycle and the temporal consistency of the data. All of these have been substantially improved in the ERA-interim data used here relative to previous reanalysis products (Dee *et al.*, 2011). The choice of ERA-Interim data is also supported by the fact that the ECMWF model on which this is based has one of the best simulations of the MJO (Vitart and Molteni, 2010). The accuracy of the ECCO ocean state estimate is assessed by Wunsch and Heimbach (2007). In many ways this is similar to atmospheric

reanalyses and has similar problems, although temporal consistency is assured due to the different methodology used for assimilating data in ECCO. The advent of Argo floats is particularly useful for such oceanic reanalyses, especially for deep ocean variability; it is thus reassuring that the Argo floats were widely assimilated into ECCO prior to the main (September 2004) case study used in Chapters 3 and 5 (Wunsch and Heimbach, 2007).

The limitations of the linear model were discussed in Chapter 4. These are predominantly due to the idealised nature of the model and the lack of currents or atmosphere-ocean interaction in the model. These simplifications limit the generality of the conclusions that can be derived from using the model, but do not fundamentally undermine its usefulness. Indeed, as outlined in Chapter 4, there are many ways in which such an idealised model is very well suited for studying the questions posed in Chapter 5. In particular, such a model allows a clean analysis of the dynamic ocean response in the absence of coupled or non-linear interactions that would complicate the interpretation of the results.

6.4 Questions and future research

There remain various important questions concerning the potential for feedbacks from the dynamical ocean response to the MJO. Foremost amongst these is to determine the relative strength of this feedback mechanism compared with the others that are well known. However, this is not easy to investigate, since the nature of the MJO consists of complex interactions between many of the mechanisms, so separating out the influences from each would be very difficult, as would distinguishing between cause and effect within such interactions. Numerical modelling studies where some mechanism is suppressed or added can be fruitful, as in, e.g., Ray *et al.* (2009), but may still miss interactions between the mechanism studied and other key processes. Alternatively, idealised models could be devised to simulate some of the important processes and the resulting simulation compared with observed MJO behaviour. The most applicable methodology for assessing the strength of the ocean dynamical feedback suggested here would be to impose SST anomalies similar to those observed into a coupled model, followed by a comparison between statistics of MJO initiation with or without this forcing. However, thermodynamic coupling would not be simulated in such an approach. A more conceptual approach to

simulate the overall implications for this mechanism compared with others would be interesting if such a model could be devised, but it is not clear how feasible it would be to make such a model sufficiently realistic.

The evidence presented here is strongly suggestive of a role for the ocean dynamics in influencing MJO behaviour, but confidence in this is limited by the small sample size, as discussed above. Further analysis once more data become available (after a decade or so) would be a useful test for this hypothesis. In addition, specific observational campaigns could provide detailed information on the structure of the equatorial ocean Rossby waves and might allow some insight into the key processes that link these dynamic processes to SST anomalies.

It is likely that the seasonal cycle and interannual variability could have a major effect upon the proposed feedback mechanism. In Chapter 2 it was shown that there is an apparent difference in the Rossby wave propagation speed between the summer and winter months. This would have a fundamental impact on the influence of the waves upon the MJO, especially with regard to resonance between the MJO and the ocean dynamics. However, further work is necessary to quantify the impact that the seasonal cycle in the equatorial current systems of the Indian Ocean would have on the wave propagation. It would be enlightening to investigate whether the wave propagation speeds are indeed fundamentally different between the seasons, for example. Analysis of ocean GCMs or the ECCO ocean state estimate could also allow direct comparison between the seasonally-varying current velocities and the intraseasonal wave propagation, as could more idealised GCM studies. For instance, using the model in Chapter 5 it would be possible to assess the degree to which such discrepancies between seasons could be ascribed purely to changes in atmospheric forcing, rather than to changes in the equatorial currents.

Another impact of interannual variability and the seasonal cycle would be to alter the mixed layer depth and thus change the magnitude of the SST signal generated by the downwelling Rossby waves. It appears that the waves are more effective at generating a positive SST signal upon arrival in the western Indian Ocean, where the thermocline is shallow and there is a known stronger correlation between SSH and SST (Xie *et al.*, 2002). Therefore it seems reasonable to suppose that seasonal, or indeed interannual, variability

in the thermocline depth here would make the feedback either stronger or weaker, depending on the sign of the depth anomaly. Further work could investigate whether the resonance between the atmospheric variability and the ocean dynamics is stronger during periods when the thermocline is shallow. If this were the case, the dynamical ocean component of the MJO could have a profound influence on the interannual and interdecadal variability of the MJO and could be crucial in understanding such variability. However, it would be difficult to assess such processes associated with primary MJ events due to their relatively small sample size; subdividing this sample would push the boundaries of statistical robustness.

Another question that may deserve further research is whether the waves have any influence on 'terminal' MJ events, where an active MJ event does not generate another. Considering the many triggering mechanisms that are known to exist when the MJO is active, it is intriguing to question whether the ocean dynamics might have a role in shutting down the MJO. This could be readily investigated using a similar methodology to that used in Chapter 3.

Testing the predictability gained by an improved understanding of such processes would be a useful next step. Given that numerical simulations of the MJO have a limit of around three weeks on predictability, it is on time scales of 2–4 weeks that the mechanism presented here might make substantial improvements to such forecasts. For example, if a downwelling Rossby wave were present in the central Indian Ocean in the initial conditions of a monthly forecast, there might be increased likelihood of an MJ event being triggered some weeks later. This could be tested by modifying the initial ocean conditions in an ensemble of hindcasts prior to a primary MJ event, and testing for increases in the hindcast skill.

6.5 Conclusion

The primary conclusion of this thesis is that the ocean dynamics form an integral component of the MJO. It is now evident that one should not view the MJO in isolation from the propagation of equatorial ocean waves that it generates. The dynamical ocean component is large and has important and wide-reaching implications for oceanography. Feedbacks from the ocean dynamics can lead to a resonance whereby the 90 day oscillations in the

Indian Ocean resonate with the 45-day oscillations of the MJO. Forcing by the ocean dynamics can trigger primary MJ events that previously had no apparent triggers, highlighting the potential for the ocean dynamics to enhance the sporadic nature of the MJO. In addition, the predictability of these waves suggests that it may be possible to improve forecasts of the MJO during periods when it has previously been most difficult to predict. In future it could be possible to enhance real-time prediction of the MJO using sustained observational monitoring of the Indian Ocean through Argo and mooring data.

References

Allen, J.S., and R.D. Romea, 1980: On coastal trapped waves at low latitudes in a stratified ocean. *J. Fluid Mech.* **98,** 555–585.

Anderson, D.L.T., K. Bryan, A.E. Gill, and R.C. Pacanowski, 1979: The transient response of the North Atlantic: some model studies. *J. Geophys. Res.* **84,** 4795–4815.

Arakawa, A., and V.R. Lamb, 1977. *Methods of Computational Physics*. New York: Academic Press.

Batstone, C.P., A.J. Matthews, and D.P. Stevens, 2005: Coupled ocean-atmosphere interactions between the Madden-Julian oscillation and synoptic-scale variability over the warm pool. *J. Climate* **18,** 2004–2020.

Battisti, D.S., 1988: Dynamics and thermodynamics of a warming event in a coupled tropical atmosphere ocean model. *J. Atmos. Sci.* **45,** 2889–2919.

Bergman, J., H.H. Hendon, and K.M. Weickmann, 2001: Intraseasonal air-sea interactions at the onset of El Niño. *J. Climate* **14,** 1702–1720.

Bernie, D.J., S.J. Woolnough, J.M. Slingo, and E. Guilyardi, 2005: Modeling diurnal and intraseasonal variability of the ocean mixed layer. *J. Climate* **18,** 1190–1202.

Bjerknes, J., 1969: Atmospheric teleconnections from equatorial Pacific. *Mon. Weath. Rev.* **97,** 163–172.

Boulanger, J.P., and L.L. Fu, 1996: Evidence of boundary reflection of Kelvin and first-mode Rossby waves from TOPEX/POSEIDON sea level data. *J. Geophys. Res.* **101,** 16361–16371.

Brink, K.H., 1982: A comparison of long coastal trapped wave theory with observations off Peru. *J. Phys. Oceanogr.* **12,** 897–913.

Brink, K.H., 1991: Coastal-trapped waves and wind-driven currents over the continental-shelf. *Annu. Rev. Fluid Mech.* **23,** 389–412.

Bryan, K., 1969: A numerical method for the circulation of the world ocean. *J. Comput. Phys.* **4,** 347–376.

Cane, M.A., and D.W. Moore, 1981: A note on low-frequency equatorial basin modes. *J. Phys. Oceanogr.* **11,** 1578–1584.

Chang, C.P., and H. Lim, 1988: Kelvin wave-CISK - a possible mechanism for the 30-50 day oscillations. *J. Atmos. Sci.* **45,** 1709–1720.

Chelton, D.B., R.A. DeSzoeke, M.G. Schlax, K. El Naggar, and N. Siwertz, 1998: Geographical variability of the first baroclinic Rossby radius of deformation. *J. Phys. Oceanogr.* **28,** 433–460.

Chelton, D.B., and M.G. Schlax, 1996: Global observations of oceanic Rossby waves. *Science* **272,** 234–238.

Chelton, D.B., M.G. Schlax, J.M. Lyman, and G.C. Johnson, 2003: Equatorially trapped Rossby waves in the presence of meridionally sheared baroclinic flow in the Pacific Ocean. *Prog. Oceanog.* **56,** 323–380.

Clarke, A.J., 1983: The reflection of equatorial waves from oceanic boundaries. *J. Phys. Oceanogr.* **13,** 1193–1207.

Clarke, A.J., 1991: On the reflection and transmission of low-frequency energy at the irregular western Pacific-Ocean boundary. *J. Geophys. Res.* **96,** 3289–3305.

Clarke, A.J., 1992: Low-frequency reflection from a nonmeridional eastern ocean boundary and the use of coastal sea-level to monitor eastern Pacific equatorial Kelvin waves. *J. Phys. Oceanogr.* **22,** 163–183.

Clarke, A.J., and X. Liu, 1993: Observations and dynamics of semiannual and annual sea levels near the eastern equatorial Indian-Ocean boundary. *J. Phys. Oceanogr.* **23,** 386–399.

Clarke, A.J., and C. Shi, 1991: Critical frequencies at ocean boundaries. *J. Geophys. Res.* **96,** 10731–10738.

Conkright, M.E., R.A. Locarnini, H.E. Garcia, T.D. O'Brien, T.P. Boyer, C. Stephen, and J.I. Antonov, 2002: World Ocean Atlas 2001: Objective Analyses, Data Statistics, and Figures, CD-ROM Documentation. *National Oceanographic Data Center, Internal Rep. 17*. 17 pp.

Cox, M.D., 1984: A primitive equation, 3-dimensional model of the ocean. Technical Report: *GFDL*.

Dee, D.P., S.M. Uppala, A.J. Simmons, P. Berrisford, P. Poli, S. Kobayashi, U. Andrae, M.A. Balmaseda, G. Balsamo, P. Bauer, P. Bechtold, A.C.M. Beljaars, L. van de Berg, J. Bidlot, N. Bormann, C. Delsol, R. Dragani, M. Fuentes, A.J. Geer, L. Haimberger, S.B. Healy, H. Hersbach, E.V. Holm, L. Isaksen, P. Kallberg, M. Koehler, M. Matricardi, A.P. McNally, B.M. Monge-Sanz, J.-. Morcrette, B.-. Park, C. Peubey, P. de Rosnay, C. Tavolato, J.-. Thepaut, and F. Vitart, 2011: The ERA-Interim reanalysis: configuration and performance of the data assimilation system. *Quart. J. Roy. Meteorol. Soc.* **137,** 553–597.

Donald, A., H. Meinke, B. Power, A.D.N. Maia, M.C. Wheeler, N. White, R.C. Stone, and J. Ribbe, 2006: Near-global impact of the Madden-Julian oscillation on rainfall. *Geophys. Res. Lett.* **33,** L09704. DOI: 10.1029/2005GL025155.

Ducet, N., P.Y. Le Traon, and G. Reverdin, 2000: Global high-resolution mapping of ocean circulation from TOPEX/Poseidon and ERS-1 and-2. *J. Geophys. Res.* **105,** 19477–19498.

Durand, F., D. Shankar, F. Birol, and S.S.C. Shenoi, 2009: Spatiotemporal structure of the East India Coastal Current from satellite altimetery. *J. Geophys. Res.* **114,** C02013. DOI: 10.1029/2008JC004807.

Edwards, L.A., R.E. Houseago-Stokes, and P. Cipollini, 2006: Altimeter observations of the MJO/ENSO connection through Kelvin waves. *Int. J. Remote Sens.* **27,** 1193–1203.

Ferranti, L., T.N. Palmer, F. Molteni, and E. Klinker, 1990: Tropical extratropical interaction associated with the 30-60 day oscillation and its impact on medium and extended range prediction. *J. Atmos. Sci.* **47,** 2177–2199.

Flatau, M., P. Flatau, P. Phoebus, and P.P. Niiler, 1997: The feedback between equatorial convection and local radiative and evaporative processes: the implications for intraseasonal oscillations. *J. Atmos. Sci.* **54,** 2373–2386.

Foltz, G.R., and M.J. McPhaden, 2004: The 30-70 day oscillations in the tropical Atlantic. *Geophys. Res. Lett.* **31,** L15205. DOI: 10.1029/2004GL020023.

Fu, L.L., 2007: Intraseasonal variability of the equatorial Indian Ocean observed from sea surface height, wind, and temperature data. *J. Phys. Oceanogr.* **37,** 188–202.

Fu, L.L., E.J. Christensen, C.A. Yamarone, M. Lefebvre, Y. Menard, M. Dorrer, and P. Escudier, 1994: TOPEX/Poseidon mission overview. *J. Geophys. Res.* **99,** 24369–24381.

Fu, X.H., and B. Wang, 2004: Differences of boreal summer intraseasonal oscillations simulated in an atmosphere-ocean coupled model and an atmosphere-only model. *J. Climate* **17,** 1263–1271.

Gentemann, C.L., F.J. Wentz, C.A. Mears, and D.K. Smith, 2004: In situ validation of Tropical Rainfall Measuring Mission microwave sea surface temperatures. *J. Geophys. Res.* **109,** C04021. DOI: 10.1029/2003JC002092.

Giese, B.J., and D.E. Harrison, 1990: Aspects of the Kelvin wave response to episodic wind forcing. *J. Geophys. Res.* **95,** 7289–7312.

Gill, A.E., 1980: Some simple solutions for heat-induced tropical circulation. *Quart. J. Roy. Meteorol. Soc.* **106,** 447–462.

Gill, A.E., 1982. *Atmosphere-ocean dynamics*. Academic Press.

Greenslade, D.J.M., D.B. Chelton, and M.G. Schlax, 1997: The midlatitude resolution capability of sea level fields constructed from single and multiple satellite altimeter datasets. *J. Atmos. Ocean. Tech.* **14,** 849–870.

Han, W., 2005: Origins and dynamics of the 90-day and 30-60-day variations in the equatorial Indian Ocean. *J. Phys. Oceanogr.* **35,** 708–728.

Han, W., D.M. Lawrence, and P.J. Webster, 2001: Dynamical response of equatorial Indian Ocean to intraseasonal winds: zonal flow. *Geophys. Res. Lett.* **28,** 4215–4218.

Han, W.Q., J.P. McCreary, D.L.T. Anderson, and A.J. Mariano, 1999: Dynamics of the eastern surface jets in the equatorial Indian Ocean. *J. Phys. Oceanogr.* **29,** 2191–2209.

Han, W., P.J. Webster, J.L. Lin, T. Liu, R. Fu, D. Yuan, and A. Hu, 2008: Dynamics of intraseasonal sea level and thermocline variability in the equatorial Atlantic during 2002–03. *J. Phys. Oceanogr.* **38,** 945–967.

Harrison, D., and G. Vecchi, 2001: January 1999 Indian Ocean cooling event. *Geophys. Res. Lett.* **28,** 3717–3720.

Heimbach, P., C. Hill, and R. Giering, 2005: An efficient exact adjoint of the parallel MIT General Circulation Model, generated via automatic differentiation. *Future Gener. Comput. Syst.* **21,** 1356–1371.

Hendon, H.H., 2000: Impact of air-sea coupling on the Madden-julian oscillation in a general circulation model. *J. Atmos. Sci.* **57,** 3939–3952.

Hendon, H.H., B. Liebman, and J.D. Glick, 1998: Oceanic Kelvin waves and the Madden Julian oscillation. *J. Atmos. Sci.* **55,** 88–101.

Hendon, H.H., and B. Liebmann, 1990: A composite study of onset of the Australian summer monsoon. *J. Atmos. Sci.* **47,** 2227–2240.

Hendon, H.H., and M.L. Salby, 1994: The life-cycle of the Madden-Julian oscillation. *J. Atmos. Sci.* **51,** 2225–2237.

Hendon, H.H., C. Zhang, and J.D. Glick, 1999: Interannual variation of the Madden-Julian oscillation during austral summer. *J. Climate* **12,** 2538–2550.

Hsu, H.H., B.J. Hoskins, and F.F. Jin, 1990: The 1985/86 Intraseasonal Oscillation and the role of the extratropics. *J. Atmos. Sci.* **47,** 823–839.

Hsu, H.H., and M.Y. Lee, 2005: Topographic effects on the eastward propagation and initiation of the Madden-Julian oscillation. *J. Climate* **18,** 795–809.

Huthnance, J.M., 1975: Trapped waves over a continental-shelf. *J. Fluid Mech.* **69,** 689–704.

Huthnance, J.M., 1985: Flow across reefs or between islands, and effects on shelf-sea motions. *Continental Shelf Research* **4,** 709–731.

Inness, P.M., and J.M. Slingo, 2003: Simulation of the Madden-Julian oscillation in a coupled general circulation model. Part I: Comparison with observations and an atmosphere-only GCM. *J. Climate* **16,** 345–364.

Isoguchi, O., and H. Kawamura, 2006: MJO-related summer cooling and phytoplankton blooms in the South China Sea in recent years. *Geophys. Res. Lett.* **33,** L16615. DOI: 10.1029/2006GL027046.

Izumo, T., S. Masson, J. Vialard, C.d.B. Montegut, S.K. Behera, G. Madec, K. Takahashi, and T. Yamagata, 2010: Low and high frequency Madden-Julian oscillations in austral summer: interannual variations. *Clim. Dyn.* **35,** 669–683.

Jones, C., L.M.V. Carvalho, R.W. Higgins, D.E. Waliser, and J.K.E. Schemm, 2004: A statistical forecast model of tropical intraseasonal convective anomalies. *J. Climate* **17,** 2078–2095.

Jones, C., D.E. Waliser, and C. Gautier, 1998: The influence of the Madden-Julian oscillation on ocean surface heat fluxes and sea surface temperature. *J. Climate* **11,** 1057–1072.

Jones, C., D.E. Waliser, J.K.E. Schemm, and W.K.M. Lau, 2000: Prediction skill of the Madden and Julian Oscillation in dynamical extended range forecasts. *Clim. Dyn.* **16,** 273–289.

Kang, I., and H. Kim, 2010: Assessment of MJO Predictability for Boreal Winter with Various Statistical and Dynamical Models. *J. Climate* **23,** 2368–2378.

Katz, E.J., 1997: Waves along the equator in the Atlantic. *J. Phys. Oceanogr.* **27,** 2536–2544.

Kessler, W.S., and M.J. McPhaden, 1995: Oceanic equatorial waves and the 1991-93 El-Nino. *J. Climate* **8,** 1757–1774.

Kessler, W.S., M.J. McPhaden, and K.M. Weickmann, 1995: Forcing of intraseasonal Kelvin waves in the equatorial Pacific. *J. Geophys. Res.* **100,** 10,613–10,631.

Killworth, P.D., D. Stainforth, D.J. Webb, and S.M. Paterson, 1991: The development of a free-surface Bryan-Cox-Semtner ocean model. *J. Phys. Oceanogr.* **21,** 1333–1348.

Klingaman, N.P., H. Weller, J.M. Slingo, and P.M. Inness, 2008: The intraseasonal variability of the Indian summer monsoon using TMI sea surface temperatures and ECMWF reanalysis. *J. Climate* **21,** 2519–2539.

Klingaman, N.P., S.J. Woolnough, H. Weller, and J.M. Slingo, 2011: The Impact of Finer-Resolution Air-Sea Coupling on the Intraseasonal Oscillation of the Indian Monsoon. *J. Climate* **24,** 2451–2468.

Knutson, T.R., and K.M. Weickmann, 1987: 30-60 day atmospheric oscillations - composite life-cycles of convection and circulation anomalies. *Mon. Weath. Rev.* **115,** 1407–1436.

Kummerow, C., J. Simpson, O. Thiele, W. Barnes, A.T.C. Chang, E. Stocker, R.F. Adler, A. Hou, R. Kakar, F. Wentz, P. Ashcroft, T. Kozu, Y. Hong, K. Okamoto, T. Iguchi, H. Kuroiwa, E. Im, Z. Haddad, G. Huffman, B. Ferrier, W.S. Olson, E. Zipser, E.A. Smith, T.T. Wilheit, G. North, T. Krishnamurti, and K. Nakamura, 2000: The status of the Tropical Rainfall Measuring Mission (TRMM) after two years in orbit. *J. Appl. Met.* **39,** 1965–1982.

Lau, K.M., and L. Peng, 1987: Origin of low-frequency (intraseasonal) oscillations in the tropical atmosphere. 1. basic theory. *J. Atmos. Sci.* **44,** 950–972.

Lau, W.K.M., and D.E. Waliser, (eds). 2005. *Intraseasonal variability in the atmosphere–ocean climate system*. Springer-Praxis: Heidelberg, Germany.

Lavender, S.L., and A.J. Matthews, 2009: Response of the west African monsoon to the Madden-Julian oscillation. *J. Climate* **In Press,** In Press.

Le Traon, P.Y., G. Dibarboure, and N. Ducet, 2001: Use of a high-resolution model to analyze the mapping capabilities of multiple-altimeter missions. *J. Atmos. Ocean. Tech.* **18,** 1277–1288.

Le Traon, P.Y., J. Stum, J. Dorandeu, P. Gaspar, and P. Vincent, 1994: Global statistical-analysis of Topex and Poseidon data. *J. Geophys. Res.* **99,** 24619–24631.

Liebmann, B., G.N. Kiladis, C.S. Vera, A.C. Saulo, and L.M.V. Carvalho, 2004: Subseasonal variations of rainfall in South America in the vicinity of the low-level jet east of the Andes and comparison to those in the South Atlantic convergence zone. *J. Climate* **17,** 3829–3842.

Liebmann, B., and C.A. Smith, 1996: Description of a complete (interpolated) outgoing longwave radiation dataset. *Bull. Am. Meteorol. Soc.* **77,** 1275–1277.

Lighthill, M.J., 1969: Dynamic response of Indian Ocean to onset of the southwest monsoon. *Phil. Trans. R. Soc. London* **265,** 45–92.

Love, B.S., and A.J. Matthews, 2009: Real-time localised forecasting of the Madden-Julian Oscillation using neural network models. *Quart. J. Roy. Meteorol. Soc.* **135,** 1471–1483.

Madden, R., 1986: Seasonal Variations of the 40-50 Day Oscillation in the Tropics.. *J. Atmos. Sci.* **43,** 3138–3158.

Madden, R.A., and P.R. Julian, 1971: Detection of a 40-50 day oscillation in zonal wind in the tropical Pacific. *J. Atmos. Sci.* **28,** 702–708.

Madden, R.A., and P.R. Julian, 1972: Description of global-scale circulation cells in the tropics with a 40-50 day period. *J. Atmos. Sci.* **29,** 1109–1123.

Madden, R.A., and P.R. Julian, 1994: Observations of the 40-50 day oscillation, a review. *Mon. Weath. Rev.* **122,** 814–836.

Majda, A.J., and J.A. Biello, 2004: A multiscale model for tropical intraseasonal oscillations. *Proc. Natl. Acad. Sci. U. S. A.* **101,** 4736–4741.

Marshall, J., C. Hill, L. Perelman, and A. Adcroft, 1997a: Hydrostatic, quasi-hydrostatic, and nonhydrostatic ocean modeling. *J. Geophys. Res.* **102,** 5733–5752.

Marshall, J., A. Adcroft, C. Hill, L. Perelman, and C. Heisey, 1997b: A finite-volume, incompressible Navier Stokes model for studies of the ocean on parallel computers. *J. Geophys. Res.* **102,** 5753–5766.

Matsuno, T., 1966: Quasi-geostrophic motions in the equatorial area. *J. Meteor. Soc. Japan* **44,** 25–43.

Matthews, A.J., 2000: Propagation mechanisms for the Madden-Julian oscillation. *Quart. J. Roy. Meteorol. Soc.* **126,** 2637–2651.

Matthews, A.J., 2008: Primary and successive events in the Madden-Julian oscillation. *Quart. J. Roy. Meteorol. Soc.* **134,** 439–453.

Matthews, A.J., B.J. Hoskins, and M. Masutani, 2004: The global response to tropical heating in the Madden-Julian oscillation during the northern winter. *Quart. J. Roy. Meteorol. Soc.* **130,** 1991–2011.

Matthews, A.J., and G.N. Kiladis, 1999: The tropical-extratropical interaction between high-frequency transients and the Madden-Julian oscillation. *Mon. Weath. Rev.* **127,** 661–677.

Matthews, A.J., and M.P. Meredith, 2004: Variability of Antarctic circumpolar transport and the Southern Annular Mode associated with the Madden-Julian Oscillation. *Geophys. Res. Lett.* **31,** L24312. DOI: 10.1029/2004GL021666.

Matthews, A.J., P. Singhruck, and K.J. Heywood, 2007: Deep ocean impact of a Madden-Julian oscillation observed by Argo floats. *Science* **318,** 1765–1768.

Matthews, A.J., P. Singhruck, and K.J. Heywood, 2010: Ocean temperature and salinity components of the Madden-Julian oscillation observed by Argo floats. *Clim. Dyn.* **35,** 1149–1168.

Matthews, A.J., 2004a: Intraseasonal variability over tropical Africa during northern summer. *J. Climate* **17,** 2427–2440.

Matthews, A.J., 2004b: Atmospheric response to observed intraseasonal tropical sea surface temperature anomalies. *Geophys. Res. Lett.* **31,** L14107. DOI: 10.1029/2004GL020474.

McCreary, J.P., 1983: A model of tropical ocean-atmosphere interaction. *Mon. Weath. Rev.* **111,** 370–387.

McCreary, J.P., P.K. Kundu, and R.l. Molinari, 1993: A numerical investigation of dynamics, thermodynamics and mixed-layer processes in the Indian-Ocean. *Prog. Oceanog.* **31,** 181–244.

McPhaden, M.J., 1999: Genesis and evolution of the 1997–98 El Niño. *Science* **283,** 950–954.

McPhaden, M.J., F. Bahr, Y. Dupenhoat, E. Firing, S.P. Hayes, P.P. Niiler, P.L. Richardson, and J.M. Toole, 1992: The response of the western equatorial Pacific-Ocean to westerly wind bursts during November 1989 to January 1990. *J. Geophys. Res.* **97,** 14289–14303.

McPhaden, M.J., and P. Ripa, 1990: Wave–mean flow interactions in the equatorial ocean. *Annu. Rev. Fluid Mech.* **22,** 167–205.

Moore, A.M., 1968. *Planetary-gravity waves in an equatorial ocean*. Thesis (PhD), Harvard University, Cambridge, Mass..

Moore, D.W., and S.G.H. Philander, 1977: Modeling of the tropical oceanic circulation. Pp 319–361 in *The Sea.* Goldberg, E.D., I.N. McCave, J.J. O'Brien, and J.H. Steele, (eds). Wiley-Interscience.

Nakazawa, T., 1988: Tropical super clusters within intraseasonal variations over the western Pacific. *J. Meteor. Soc. Japan* **66,** 823–839.

Neelin, J.D., D.S. Battisti, A.C. Hirst, F.F. Jin, Y. Wakata, T. Yamagata, and S.E. Zebiak, 1998: ENSO theory. *J. Geophys. Res.* **103,** 14261–14290.

Oliver, E.C.J., and K.R. Thompson, 2010: Madden-Julian Oscillation and sea level: Local and remote forcing. *J. Geophys. Res.* **115,** C01003. DOI: 10.1029/2009JC005337.

Oliver, E.C.J., and K.R. Thompson, 2011: Sea level and circulation variability of the Gulf of Carpentaria: Influence of the Madden-Julian Oscillation and the adjacent deep ocean. *J. Geophys. Res.* **116,** . DOI: 10.1029/2010JC006596.

Pai, D.S., J. Bhate, O.P. Sreejith, and H.R. Hatwar, 2011: Impact of MJO on the intraseasonal variation of summer monsoon rainfall over India. *Clim. Dyn.* **36,** 41–55.

Philander, S.G.H., 1979: Equatorial waves in the presence of the equatorial undercurrent. *J. Phys. Oceanogr.* **9,** 254–262.

Philander, S.G.H., 1981: The response of equatorial oceans to a relaxation of the trade winds. *J. Phys. Oceanogr.* **11,** 176–189.

Pohl, B., and A.J. Matthews, 2007: Observed changes in the lifetime and amplitude of the Madden-Julian oscillation associated with interannual ENSO sea surface temperature anomalies. *J. Climate* **20,** 2659–2674.

Polo, I., A. Lazar, B. Rodriguez-Fonseca, and S. Arnault, 2008: Oceanic Kelvin waves and tropical Atlantic intraseasonal variability: 1. Kelvin wave characterization. *J. Geophys. Res.* **113,** C07009. DOI: 10.1029/2007JC004495.

Rao, S.A., and T. Yamagata, 2004: Abrupt termination of Indian Ocean dipole events in response to intraseasonal disturbances. *Geophys. Res. Lett.* **31,** L19306. DOI: 10.1029/2004GL020842.

Rashid, H.A., H.H. Hendon, M.C. Wheeler, and O. Alves, 2011: Prediction of the Madden-Julian oscillation with the POAMA dynamical prediction system. *Clim. Dyn.* **36,** 649–661.

Ray, P., C. Zhang, J. Dudhia, and S.S. Chen, 2009: A Numerical Case Study on the Initiation of the Madden-Julian Oscillation. *J. Atmos. Sci.* **66,** 310–331.

Reynolds, R.W., T.M. Smith, C. Liu, D.B. Chelton, K.S. Casey, and M.G. Schlax, 2007: Daily high-resolution-blended analyses for sea surface temperature. *J. Climate* **20,** 5473–5496.

Ricciardulli, L., and F. Wentz, 2004: Uncertainties in sea surface temperature retrievals from space: Comparison of microwave and infrared observations from TRMM. *J. Geophys. Res.* **109,** . DOI: 10.1029/2003JC002247.

Roundy, P.E., and G.N. Kiladis, 2006: Observed relationships between oceanic Kelvin waves and atmospheric forcing. *J. Climate* **19,** 5253–5272.

Roundy, P.E., I.I.I. Schreck, and M.A. Janiga, 2009: Contributions of convectively coupled equatorial Rossby waves and Kelvin waves to the real-time multivariate MJO indices. *Mon. Weath. Rev.* **137,** 469–478.

Saji, N., B. Goswami, P. Vinayachandran, and T. Yamagata, 1999: A dipole mode in the tropical Indian Ocean. *Nature* **401,** 360–363.

Salby, M.L., and R.R. Garcia, 1987: Transient-response to localized episodic heating in the tropics .1. Excitation and short-time near-field behavior. *J. Atmos. Sci.* **44,** 458–498.

Salby, M.L., and H.H. Hendon, 1994: Intraseasonal behavior of clouds, temperature, and motion in the tropics. *J. Atmos. Sci.* **51,** 2207–2224.

Schlax, M.G., and D.B. Chelton, 1994: Aliased tidal errors in Topex/Poseidon sea-surface height data. *J. Geophys. Res.* **99,** 24761–24775.

Semtner, A.J., 1974: A general circulation model for the world ocean. Technical Report: *UCLA Department of Meteorology*.

Shinoda, T., and W. Han, 2005: Influence of the Indian Ocean Dipole on atmospheric subseasonal variability. *J. Climate* **18,** 3891–3909.

Shinoda, T., H.H. Hendon, and J. Glick, 1998: Intraseasonal variability of surface fluxes and sea surface temperature in the tropical western Pacific and Indian Oceans. *J. Climate* **11,** 1685–1702.

Slingo, J., P. Inness, R. Neale, S. Woolnough, and G. Yang, 2003: Scale interactions on diurnal to seasonal timescales and their relevance to model systematic errors. *Ann. Geophys.* **46,** 139–155.

Slingo, J.M., D.P. Rowell, K.R. Sperber, and E. Nortley, 1999: On the predictability of the interannual behaviour of the Madden-Julian Oscillation and its relationship with El Nino. *Quart. J. Roy. Meteorol. Soc.* **125,** 583–609.

Spall, M., and J. Pedlosky, 2005: Reflection and transmission of equatorial Rossby waves. *J. Phys. Oceanogr.* **35,** 363–373.

Stammer, D., F. Wentz, and C. Gentemann, 2003: Validation of microwave sea surface temperature measurements for climate purposes. *J. Climate* **16,** 73–87.

Stevens, D.P., 1988. *Towards modelling the Norwegian-Greenland Sea*. Thesis (PhD), University of East Anglia, Norwich, UK.

Suarez, M.J., and P.S. Schopf, 1988: A delayed action oscillator for ENSO. *J. Atmos. Sci.* **45,** 3283–3287.

Sui, C.H., and K.M. Lau, 1989: Origin of low-frequency (intraseasonal) oscillations in the tropical atmosphere. Part II: structure and propagation of mobile wave-CISK modes and their modification by lower boundary forcings. *J. Atmos. Sci.* **46,** 37–56.

Tomczak, M., and J.S. Godfrey, 1994. *Regional oceanography: an introduction*. Pergamon.

Valsala, V., 2008: First and second baroclinic mode responses of the tropical Indian Ocean to interannual equatorial wind anomalies. *J. Oceanog.* **64,** 479–494.

Vialard, J., S.S.C. Shenoi, J.P. McCreary, D. Shankar, F. Durand, V. Fernando, and S.R. Shetye, 2009: Intraseasonal response of the northern Indian Ocean coastal waveguide to the Madden-Julian Oscillation. *Geophys. Res. Lett.* **36,** L14606. DOI: 10.1029/2009GL038450.

Vitart, F., and F. Molteni, 2010: Simulation of the Madden-Julian Oscillation and its teleconnections in the ECMWF forecast system. *Quart. J. Roy. Meteorol. Soc.* **136,** 842–855.

Waliser, D.E., K.M. Lau, and J.H. Kim, 1999: The influence of coupled sea surface temperatures on the Madden-Julian oscillation: A model perturbation experiment. *J. Atmos. Sci.* **56,** 333–358.

Waliser, D.E., R. Murtugudde, and L.E. Lucas, 2003: Indo-Pacific Ocean response to atmospheric intraseasonal variability: 1. Austral summer and the Madden-Julian oscillation. *J. Geophys. Res.* **108,** 3160. DOI: 10.1029/2002JC001620.

Waliser, D.E., R. Murtugudde, P. Strutton, and J.L. Li, 2005: Subseasonal organization of ocean chlorophyll: Prospects for prediction based on the Madden-Julian Oscillation. *Geophys. Res. Lett.* **32,** . DOI: 10.1029/2005GL024300.

Wang, B., and H. Rui, 1990: Synoptic climatology of transient tropical intraseasonal convection anomalies - 1975-1985. *Meteorol. Atmos. Phys.* **44,** 43–61.

Wang, B., and X.S. Xie, 1998: Coupled modes of the warm pool climate system. Part 1: The role of air-sea interaction in maintaining Madden-Julian oscillation. *J. Climate* **11,** 2116–2135.

Webb, D.J., 1996: An ocean model code for array processor computers. *Computers & Geosciences* **22,** 569–578.

Webber, B.G.M., A.J. Matthews, and K.J. Heywood, 2010: A dynamical ocean feedback mechanism for the Madden-Julian Oscillation. *Quart. J. Roy. Meteorol. Soc.* **136,** 740–754.

Webber, B.G.M., A.J. Matthews, K.J. Heywood, and D.P. Stevens, 2012a: Ocean Rossby waves as a triggering mechanism for primary Madden-Julian events. *Quart. J. Roy. Meteorol. Soc.* **138,** 514–527.

Webber, B.G.M., D.P. Stevens, A.J. Matthews, and K.J. Heywood, 2012b: Dynamical ocean forcing of the Madden-Julian Oscillation at lead times of up to five months. *J. Climate* **25,** 2824–2842.

Webster, P.J., and R. Lukas, 1992: TOGA COARE - The Coupled Ocean Atmosphere Response Experiment. *Bull. Am. Meteorol. Soc.* **73,** 1377–1416.

Wheeler, M.C., and H.H. Hendon, 2004: An all-season real-time multivariate MJO index: Development of an index for monitoring and prediction. *Mon. Weath. Rev.* **132,** 1917–1932.

Wheeler, M.C., H.H. Hendon, S. Cleland, H. Meinke, and A. Donald, 2009: Impacts of the Madden-Julian Oscillation on Australian Rainfall and Circulation. *J. Climate* **22,** 1482–1498.

Wilks, D.S., 1995. *Statistical Methods in the Atmospheric Sciences*. Academic Press: London, UK.

Woolnough, S.J., J.M. Slingo, and B.J. Hoskins, 2000: The relationship between convection and sea surface temperature on intraseasonal timescales. *J. Climate* **13,** 2086–2104.

Woolnough, S.J., J.M. Slingo, and B.J. Hoskins, 2001: The organization of tropical convection by intraseasonal sea surface temperature anomalies. *Quart. J. Roy. Meteorol. Soc.* **127,** 887–907.

Wu, Z.H., 2003: A shallow CISK, deep equilibrium mechanism for the interaction between large-scale convection and large-scale circulations in the tropics. *J. Atmos. Sci.* **60,** 377–392.

Wunsch, C., 1997: The vertical partition of oceanic horizontal kinetic energy. *J. Phys. Oceanogr.* **27,** 1770–1794.

Wunsch, C., and P. Heimbach, 2007: Practical global oceanic state estimation. *Physica D* **230,** 197–208.

Xie, S.P., H. Annamalai, F.A. Schott, and J.P. McCreary, 2002: Structure and mechanisms of South Indian Ocean climate variability. *J. Climate* **15,** 864–878.

Xie, P.P., and P.A. Arkin, 1997: Global precipitation: A 17-year monthly analysis based on gauge observations, satellite estimates, and numerical model outputs. *Bull. Am. Meteorol. Soc.* **78,** 2539–2558.

Zavala-Garay, J., C. Zhang, A.M. Moore, and R. Kleeman, 2005: The linear response of ENSO to the Madden-Julian oscillation. *J. Climate* **18,** 2441–2459.

Zebiak, S.E., and M.A. Cane, 1987: A model El-Nino Southern Oscillation. *Mon. Weath. Rev.* **115,** 2262–2278.

Zhang, C.D., 2001: Intraseasonal perturbations in sea surface temperatures of the equatorial eastern Pacific and their association with the Madden-Julian oscillation. *J. Climate* **14,** 1309–1322.

Zhang, C.D., 2005: Madden-Julian oscillation. *Rev. Geophys.* **43,** RG2003. DOI: 10.1029/2004RG000158.

Acronyms

BADC	British Atmospheric Data Centre
CFL	Courant-Friedrichs-Lewy
DJF	December–February
ECCO	Estimating the Circulation and Climate of the Ocean
ECMWF	European Centre for Medium-Range Weather Forecasts
ENSO	El-Niño Southern Oscillation
EOF	Empirical Orthogonal Function
IOD	Indian Ocean Dipole
ISV	Intraseasonal Variability
ITCZ	Intertropical Convergence Zone
ITF	Indonesian Throughflow
GCM	General Circulation Model
GODAE	Global Ocean Data Assimilation Experiment
MIT	Massachusetts Institute of Technology
MJ	Madden-Julian
MJO	Madden-Julian Oscillation
MLD	Mixed Layer Depth
MOM	Modular Ocean Model
OLR	Outgoing Longwave Radiation
PC	Principal Component
PV	Potential Vorticity
SCC	Super Cloud Clusters
SSH	Sea Surface Height
SST	Sea Surface Temperature
TMI	TRMM Microwave Imaging
TRMM	Tropical Rainfall Measuring Mission
WH	Wheeler Hendon
WOCE	World Ocean Circulation Experiment
WWB	westerly wind burst